Synthesis, Characterization, Thermal and Rheological Studies in Nanofluids

A thesis submitted to the
Board of Studies in Chemical Sciences
In partial fulfillment of requirements
For the Degree of

DOCTOR OF PHILOSOPHY

of

Homi Bhabha National Institute

By

Shima. P. D
Enrolment No: CHEM02200704007
Indira Gandhi Centre for Atomic Research
Kalpakkam-603 102, Tamil Nadu, India

Research Supervisor

Dr. John Philip
Head, SMART Section, NDE Division
Metallurgy and Materials Group
Indira Gandhi Centre for Atomic Research
Kalpakkam-603 102, Tamil Nadu, India

August, 2011

Synthesis, Characterization, Thermal and Rheological Studies in Nanofluids

By

Shima. P. D

Enrolment No: CHEM02200704007
SMART Section, NDE Division,
Indira Gandhi Centre for Atomic research
Kalpakkam-603 102, Tamilnadu, India

A thesis submitted to the
Board of Studies in Chemical Sciences
In partial fulfillment of requirements
For the Degree of

DOCTOR OF PHILOSOPHY

of

Homi Bhabha National Institute
Deemed University, Mumbai, India

August, 2011

Homi Bhabha National Institute

Recommendations of the Viva Voce Board

As members of the Viva Voce Board, we certify that we have read the dissertation prepared by **Shima. P. D** entitled **"Synthesis, Characterization, Thermal and Rheological Studies in Nanofluids"** and recommend that it may be accepted as fulfilling the dissertation requirement for the Degree of Doctor of Philosophy.

Date:

Chairman - **Dr. M. Saibaba**

Date:

Convener - **Dr. John Philip**

Date:

Member 1 - **Dr. T. Jayakumar**

Date:

Member 2 - **Dr. K. V. G. Kutty**

Date:

Member 3 - **Dr. V. Jayaraman**

Final approval and acceptance of this dissertation is contingent upon the candidate's submission of the final copies of the dissertation to HBNI.

I hereby certify that I have read this dissertation prepared under my direction and recommend that it may be accepted as fulfilling the dissertation requirement.

Date:

Guide - **Dr. John Philip**

STATEMENT BY AUTHOR

This dissertation has been submitted in partial fulfillment of requirements for an advanced degree at Homi Bhabha National Institute (HBNI) and is deposited in the Library to be made available to borrowers under rules of the HBNI.

Brief quotations from this dissertation are allowable without special permission, provided that accurate acknowledgement of source is made. Requests for permission for extended quotation from or reproduction of this manuscript in whole or in part may be granted by the Competent Authority of HBNI when in his or her judgment the proposed use of the material is in the interests of scholarship. In all other instances, however, permission must be obtained from the author.

(**Shima. P. D**)

Kalpakkam
August, 2011

DECLARATION

I, hereby declare that the investigation presented in the thesis entitled ***"Synthesis, Characterization, Thermal and Rheological Studies in Nanofluids"*** submitted to **Homi Bhabha National Institute (HBNI),** Mumbai, India, for the award of **Doctor of Philosophy** in **Chemical Sciences** is the record of work carried out by me during the period from March 2007 to August 2011 under the guidance of **Dr. John Philip,** Head, SMARATS, NDED, Materials and Metallurgy Group, Indira Gandhi Centre for Atomic Research, Kalpakkam. The work is original and has not been submitted earlier as a whole or in part for a degree / diploma at this or any other Institution / University.

(**Shima. P. D**)

Kalpakkam
August, 2011

Dedicated To My

Parents,

Teachers

&

Friends

ACKNOWLEDGEMENTS

I thank **Dr. Baldev Raj** and **Shri. S. C. Chetal** the former and present Director of IGCAR for permitting me to pursue research at this premier centre. I express my sincere gratitude to **Dr Baldev Raj** for his inspirational talks**.** I am grateful to **Dr. T. Jayakumar**, Director, Metallurgy and Materials Group for his motivating words, kind advices and helpful suggestions. His advices on several occasions have been a source strength and inspiration for me.

I express my deep sense of gratitude to my advisor **Dr. John Philip** for his valuable guidance, innovative ideas, insightful comments and suggestions, constant support and encouragement. His mentorship provided me with the perfect balance of research independence and support. I am grateful for all his contributions and creative ideas that made my Ph.D. experience challenging and stimulating.

My sincere thanks to the doctoral committee members **Dr. M. Sai Baba, Dr. T. Jayakumar**, **Dr. K. V. G. Kutty**, **Dr. V. Jayaraman** and **Dr. J. Philip** for their constant encouragement and valuable suggestions throughout my research career. I am thankful to **Dr. M. Sai Baba** for his motivation, kind advices and for making my stay enjoyable in the enclave.

I thank each member of SMARTS, NDED and GRIP for their kind help and support during my research period. Special thanks to my friends for their valuable help, support and care. I thank my family for their support of all my life choices and their love, which has been a constant source of strength for everything I do.

August, 2011 (**Shima. P. D**)

Contents

Page No.

Chapter I

Introduction

Chapter II

Synthesis and Characterization Techniques

Chapter – III

Size Controlled Synthesis of Nanoparticles and Nanofluids

Chapter – IV 69

Effect of Nanoparticle Aggregation on Thermal and Rheological Properties of Nanofluids

Chapter – V 94

Tuning of Thermal Conductivity of Nanofluids Using an External Stimulus

Chapter – VI 120

Study of Temperature Dependent Thermal Conductivity and Viscosity of Aqueous and Non-Aqueous Magnetite Nanofluids

Chapter – VII 141

Effect of Particle Size on Thermal Conductivity and Viscosity of Magnetite Nanofluids

Chapter – VIII 153

Conclusions and Perspectives

SYNOPSIS

With constantly increasing thermal loads due to smaller features of microelectronic devices and higher power outputs, there is an urgent need to develop advanced cooling techniques and innovative heat transfer fluids with better heat transfer performance than those presently available. The low thermal conductivity (k) of conventional heat transfer fluid is a serious limitation in improving the performance and compactness of engineering equipments. By considering the fact that metallic solids possess higher k than conventional heat transfer fluids, it is speculated that the thermal conductivities of fluids containing suspended solid metallic could exhibit significantly higher than that of conventional fluids. To test the above concept, colloidal dispersions of nanometer-sized particles in traditional heat transfer fluids, popularly known as nanofluids, have been attempted by many researchers. Nanofluids got intense scientific attention after the first report of unusual k enhancement for copper (Cu) nanofluids, at very low particle loading. Subsequent to that, numerous theoretical and experimental studies have been carried out on k of nanofluids.

Despite numerous experimental studies on thermal conductivity of nanofluids, it is not clear whether the k enhancement in nanofluids are anomalous or within the predictions of effective medium theory of Maxwell. Non-reproducibility and the lack of consensus on the mechanism of k enhancement in nanofluid are because of poor stability of the nanofluids and aggregating structures formed in the base fluids. For better understanding of nanofluid k, it is necessary to use model nanofluids with long term stability. Moreover, colloidal chemistry, sedimentation, and agglomeration are some of the important issues to be looked at carefully during k measurements. Towards this goals, systematic k studies in nanofluids with particle size < 10 nm are pursued to provide better insight into k enhancement in nanofluids. The main

objectives of the thesis are: (1) To synthesize nanofluids with particle size less than 10 nm with long term stability and to study their thermal properties (2) To probe the effect of Brownian motion induced convection and nanoparticle aggregation on k of nanofluids (3) To study the effect of nanoparticle aggregation on k, viscosity (η) and size distribution of stable and unstable nanofluids (4) To obtain better insights into the effect of particle size on k enhancement and (5) To study the tunable k and η of magnetically polarizable nanofluids.

To realize the above objectives, stable colloidal suspensions of magnetite (Fe_3O_4), copper oxide (CuO) and silver (Ag) nanoparticles of average diameter of < 10 nm are prepared. This thesis consists of eight chapters. Chapter 1 gives a brief introduction to nanofluids and their applications. Chapter 2 describes the nanoparticle synthesis methods, the experimental techniques used for nanoparticles characterization, details of k measurement technique and rheology measurement. Chapter 3 presents the methods used to produce nanoparticles of different size and their characterization by various techniques. Chapter 4 describes the thermal and rheological results in stable Fe_3O_4 and unstable CuO nanofluids. Chapter 5 describes the thermal and rheological properties of kerosene and hexadecane based Fe_3O_4 nanofluids in presence of linear aggregates. Chapter 6 describes temperature-dependent k of aqueous and non-aqueous nanofluids stabilized with a monolayer of surfactant. Chapter 7 describes the size dependant k studies in nanofluids with long term stability. Chapter 8 summarizes the results obtained, conclusions drawn and the scope for future work. The important findings of this thesis are briefly described below. Stable nanofluids exhibit moderate k enhancement within the predictions of effective medium theory(EMT), where unstable nanofluids exhibit k enhancement beyond EMT predictions. An invariant k, viscosity and particle size distribution are observed with time after sonication in stable nanofluids, whereas they are time dependent in unstable nanofluids. Aggregation in nanofluids is essentially governed by surface chemistry of the nanoparticles and hence surface functionalization is very important for improved stability and performance of nanofluids. Anomalous k enhancement is observed in a magnetically polarizable nanofluid in presence of external magnetic field due to effective conduction of heat through the chain like aggregates of nanoparticles, when the field orientation is parallel to the heat flow. In the absence of magnetic field, magnetically polarizable nanofluids exhibit series modes of conduction where the k/k_f is found to be within the lower Maxwell limits. No significant change in k/k_f is observed for magnetite nanofluids when the magnetic field direction is perpendicular to the direction of heat flow, irrespective of the strength of applied magnetic field and particle loading. A series to parallel mode of conduction through nanoparticle and the base fluid is also realized by varying the magnetic field orientation in a magnetically polarizable nanofluid. The k of aqueous nanofluids increase with temperature while it shows a decrease in non-aqueous nanofluids. However, the k/k_f remains constant with an increase in temperature, irrespective of the nature of base fluid. In stable nanofluids, the average particle size remains constant with temperature, indicating negligible aggregation with rise in temperature. Absolute η decreases with an increase in temperature in both the base fluids and nanofluids and the η ratio remains almost constant with an increase in temperature. Steric stabilization and superparamagnetic nature of nanoparticles render magnetite nanofluids reversibly tunable k and η enhancements, which can be exploited for a number of technological applications in nanoelectromechanical system (NEMS) and microelectromechanical system (MEMS) based devices. The k studies under controlled aggregation, size and temperature unambiguously confirm that Brownian motion induced microconvection is not the key mechanism responsible for k enhancement of nanofluids.

LIST OF FIGURES

LIST OF TABLES

LIST OF ABBREVIATIONS

Symbol	Abbreviation
A	Absorbance
E_a	Activation energy
Q	Adjustment parameter dependent on the geometry
t_p	Aggregation time constant
θ	Angle
K	Anisotropy constant
d	Average crystallite/particle size
k_B	Boltzmann constant
$B_{\text{crystallite}}$	Broadening due to crystallite size
τ_B	Brownian relaxation time
M_{Bulk}	Bulk magnetization
c	Concentration
C, X, Y, Z, C_k and C_η	Constants
v_N	Convection velocity
r*	Critical radius of nuclei
D_S	Critical size of particle
I	Current
Γ	Decay constant
τ	Delay time
ρ	Density of material
ρ_f	Density of fluid
ρ_P	Density of particle
D	Diffusion coefficient
h	Disordered shell of thickness
r_{ij}	Distance between particles
τ_{eff}	Effective relaxation time

$g^{(1)}(\tau)$	Electric field autocorrelation function
e	Elementary charge
γ	Euler's constant
x	Gap size
g	Gravitational acceleration
σ	Hard core diameter of the particle
C_N	Heat capacity per unit volume
q	Heat produced per unit length per unit time
d_{hy}	Hydrodynamic size
V_{hy}	Hydrodynamic volume of the particle
$G^{(2)}(\tau)$	Intensity autocorrelation function
I_0	Intensity of reference beam
I_S	Intensity of sample beam
d_{hkl}	Inter planar distance
$U_d(ij)$	Interparticle dipole-dipole interaction
$[\eta]$	Intrinsic viscosity
Z_+ and Z_-	Ionic charge
r_+ and r_-	Ionic radii
R_b	Kapitza resistance
ζ	Langevin function
L	Magnetic coupling constant
H	Magnetic field strength
B	Magnetic flux density
m	Magnetic moment
m_i and m_j	Magnetic moment of 'i' th and 'j' th particles
χ_L	Magnetic susceptibility
M	Magnetization
q_S	Magnitude of the scattering vector
ϕ_m	Maximum particle packing fraction

l_N	Mean free path
Δ	Mean separation of the centers of the molecules
ε_a	Molar absorption coefficient
V_m	Molecular volume of the precipitated species
τ_N	Neel relaxation time
N	Number density of particles
n	Order of diffraction
l	Path length
ε_0	Permittivity in vacuum
Pr	Prandlt number of the base fluid
r_a	Radial distance
r	Radius of the particle
μ	Refractive index of the medium
μ_r	Relative permeability
δ	Resolution
Re	Reynolds number of the particle
M_S	Saturation magnetization
V	Sedimentation velocity of particles
z	Separation between the chains
ε	Solvent polarity
W	Stability ratio
γ_e	Surface free energy per unit surface area
ω	System-specific exponent
T	Temperature
k	Thermal conductivity
k_f	Thermal conductivity of base fluid
k_p	Thermal conductivity of nanoparticles
α	Thermal diffusivity
t	Time

T_a	Transmittance
a	Unit length
R	Universal gas constant
μ_0	Vacuum permeability
υ	Velocity of sound in the liquid
η	Viscosity
$\eta_{\infty T}$	Viscosity at infinite temperature
η_0	Viscosity of base fluid
ϕ	Volume fraction
V_p	Volume of particles
λ	Wave length
ω_P	Weight fraction of particles

LIST OF PUBLICATIONS IN REFREED INTERNATIONAL JOURNALS

1. “Synthesis of aqueous and non-aqueous iron oxide nanofluids and study of temperature dependence on thermal conductivity and viscosity”, **P. D. Shima**, John Philip and Baldev Raj, **J. Phys. Chem. C** 2010, 114, 18825–18833

2. “Influence of aggregation on thermal conductivity in stable and unstable nanofluids”, **P. D. Shima**, John Philip and Baldev Raj, **Appl. Phys. Lett.** 2010, 97, 153113

3. “Role of microconvection induced by Brownian motion of nanoparticles in the enhanced thermal conductivity of stable nanofluids”, **P. D. Shima**, John Philip and Baldev Raj, **Appl. Phys. Lett.** 2009, 94, 223101

4. “Magnetically controllable nanofluid with tunable thermal conductivity and viscosity”, **P. D. Shima**, John Philip and Baldev Raj, **Appl. Phys. Lett.** 2009, 95, 133112

5. “Evidence for enhanced thermal conduction through percolating structures in nanofluids”, John Philip, **P. D. Shima** and Baldev Raj, **Nanotechnology** 2008, 19, 305706

6. “Nanofluid with tunable thermal properties”, John Philip, **P. D. Shima** and Baldev Raj, **Appl. Phys. Lett.** 2008, 92, 043108

7. “Enhancement of thermal conductivity in magnetite based nanofluid due to chainlike structures”, John Philip, **P. D. Shima** and Baldev Raj, **Appl. Phys. Lett.** 2007, 91, 203108

8. “Factors affecting thermal conductivity of nanofluids: effect of aggregation, particle size and temperature”, Baldev Raj, **P. D. Shima** and John Philip, **Nanotrends** 2011, 10, 14-21

9. “ Tuning of thermal conductivity of nanofluids using external stimuli”, **P. D. Shima** and John Philip, **J. Phys. Chem. C** (In Press)

INTERNATIONAL CONFERENCES

1. “Nanofluid with tunable thermal conductivity and viscosity”, **P. D. Shima**, J. Philip and Baldev Raj, International conference on Nanoscience and Nanotechnology (ICONSAT) held at Indian Institute of Technology, Mumabi, India during February 17-20, 2010. pp. 342

2. “Magnetically controllable nanofluid with tunable thermal conductivity and viscosity”, **P. D. Shima**, J. Philip and Baldev Raj, SERC School cum Symposium held at Indian Institute of Technology, Madras, India during January 4-9, 2010

3. “Role of microconvection induced by Brownian motion of nanoparticles in the enhanced thermal conductivity of stable nanofluids”, **P. D. Shima**, J. Philip and Baldev Raj, Nanotech India 2009 held at Gokulam Park - Cochin, Kerala, India during August 14-16, 2009

4. “Thermal conduction through percolating structures in nanofluids”, **P. D. Shima** and John Philip, International Conference on Frontiers in Nanoscience and Technology

(COCHIN NANO 2009) held at Cochin university, Kerala, India during January 3-6, 2009. pp. 38-39

5. "Dramatic enhancement of thermal conductivity in magnetite based nanofluid due to formation of chain like structures", **P. D. Shima**, J. Philip and Baldev Raj, International conference on Nanoscience and Nanotechnology (ICONSAT) held at Chennai Trade Center, (organized by IGCAR, Kalpakkam), India during February 27-29, 2008. pp. B100

NATIONAL WORKSHOPS

1. One day workshop on "Nano Science & Technology for Health Care" organized by IGCAR, Kalpakkam as part of ICONSAT on February 26, 2008

2. One day work shop on "Advances in Nano science & technology" conducted by Cochin University as part of COCHIN NANO on January 1'st, 2009

3. Two-Day Workshop on "Advanced Electron Microscopy" conducted by IIM Kalpakkam Chapter during October 12-13, 2009

AWARDS / RECOGNITIONS OF THESIS WORK

- "Magnetic nanofluids: Chain reaction", **Nature Nanotechnology Research Highlights**, Published online: 8 February 2008 | doi:10.1038/nnano.2008.38 (based on publication Appl. Phys. Lett. 2008, 92, 043108)

- "Nanofluid could cool tiny electronic devices", Editor's choice news story in the Technology Update section of **Nanotech Web, Institute of Physics, UK**, April 4, 2008 (based on publication Appl. Phys. Lett. 2007, 91, 203108)

- "Producing efficient heat sinks", Sci. Tech. News story, **Hindu Daily**, May 8, 2008 (based on publication Appl. Phys. Lett. 2007, 91, 203108)

- "Smart nanofluid for future cooling application", **Institute of metals and minerals Review**, No.6 June 28, 2008, pp28-31 (based on publication Nanotechnology 2008, 19, 305706)

- **Virtual Journal of Nanoscale Science & Technology**, November 26, 2007, Vol. 16, issue 22 (Appl. Phys. Lett. 2007, 91, 203108)

- **Virtual Journal of Nanoscale Science & Technology** February 11, 2008, Vol. 17, issue 6. (Appl. Phys. Lett. 2008, 92, 043108)

- **First prize for best oral presentation** for the talk titled "Thermal conduction through percolating structures in nanofluids" at the Second International Conference on Frontiers in Nanoscience and Technology (COCHIN NANO 2009) organized by Cochin University of Science and Technology, Cochin, India during January 3-6, 2009.

- **Citations** from the above works : > 200

Chapter – I

Introduction

Contents

Chapter I Introduction

1.1 Introduction

1.1.1 Nanotechnology

The seeds of nanotechnology is planted by the physicist and Nobel laureate Richard Feynman in his 1959 lecture 'There's Plenty of Room at the Bottom'.[1] Nanotechnology deals with control and manipulation of matter at the level of about 1 to 100 nm in order to create new materials, devices and systems with fundamentally new properties and functions. The goal of nanotechnology is to produce smaller, faster, cheaper, smarter information and storage devices, energy sources, medical devices etc. The success of nanotechnology crucially depends on the ability to make and manipulate objects on nano scale.

The history of nanotechnology may go back to many centuries. It is known that gold nanoparticles were used in coloring glasses in medieval times and during the days of ancient Romans. Alchemists used colloidal suspensions of nano gold and silver in water for medicinal purposes. A hair–dye formula was developed during Greek and Roman days which uses tiny lead sulphide nanocrystals to form deep inside strands of hair.[2] The Lycurgus Cup produced by the Romans in fourth century AD is one of the outstanding achievements of ancient glass industry which made use of colloidal nano gold and silver to achieve the color-shifting effect.[3] Recently researchers discovered multi walled carbon nanotubes (MWCNTs) in a seventeenth century Damascus steel sword, possibly the oldest manmade MWCNTs on record.[4] Michael Faraday, the greatest experimental physicists of all times, made the first experiments with gold nanoparticles and understood that the unexpected color was due to the extremely small size of the gold particles. His paper in philosophical transactions entitled 'Experimental relations of gold (and other metals) to light', based on his Bakerian lecture to the Royal Society in London on 5th February 1857 was perhaps the first report on quantum size effect.[5] Another nanotech breakthrough in transportation that is still important today, is the discovery by tire makers in 1928 that carbon black (down to ~ 25 nm size), when added to rubber, doubled tire mileage. So though nanoscience is very new, the technology is very old. What has changed recently is our ability to image, engineer and manipulate systems in the nano scale due to the advent of sophisticated experimental tools.

The current fever of nanotechnology is partly driven by the ever shrinking of devices in the semiconductor industry and the availability of characterization and manipulation techniques at the nanometer level. The continued decrease in device dimensions has followed the well known Moore's law,[6] which shows that the dimensions of a device halves approximately on every eighteen months. The most significant initial discovery leading to a rapid increase in understanding the properties of matter at the nanometer level is the discovery of the Scanning Tunneling Microscope (STM).[7] The invention and development of STM in early 1980s and other scanning probe microscopy such as Atomic Force Microscopy (AFM),[8] has opened up new possibilities for characterization, measurement and manipulation of nanostructures and nanomaterials. Combining with other well developed characterization and measurement techniques such as Transmission Electron Microscopy (TEM), it is possible to study and manipulate nanostructures and nanomaterials to a great detail down to atomic level.

Discovery of new materials and scientific principles stimulated nanotechnology as an area of great importance. The discovery of C_{60}, Buckminsterfullerene,[9] surprised the scientific world with the beautiful symmetric arrangement of sixty carbon atoms. The fact that such order could result from interatomic forces began to stimulate a realization that nature itself, could be a source for formation of well organized nanostructures. Discovery of carbon nanotubes stimulated greater interest due to its surprising properties[10] like unusual tensile strength, electrical conductivity, thermal conductivity etc.[11] Recently, graphene has attracted great interest in many fields of science owing to its outstanding fundamental properties and potential applications.[12] Graphene is a wonder material with many unique properties such as giant intrinsic mobility, zero effective mass, very high thermal conductivity, stiffness, impermeability to gases etc.[13] Directed self-assembly of nanoparticles open up new avenues of technology through controlled fabrication of nanoscopic materials with unique optical, magnetic, and electronic properties.[14]

Today, convergence of various events led to the recognition of nanotechnology as an area of special emphasis. Unifying science based on features of nature at the nanoscale provides a new foundation for knowledge, innovation and integration of technology. The subject has opened new scientific frontiers and has begun to redirect scientific pursuit from somewhat narrow fields of scientific disciplines to include broader objectives related to technologies and useful materials. Nanotechnology has its impacts in fields of electronics, information, chemistry, biology, medicine, energy, environment, transportation etc.

Nanotechnology has become a part of daily life with many nanotechnology products available in market now. Special nanoparticles made of carbon are used to stiffen the racquet head and shaft. The new composite hockey stick developed is more durable than other sticks because of the carbon nanotube epoxy matrix. There are new kinds of automobile paints, developed from nanotechnology, that have improved scratch-resistant qualities compared to the conventional car paints. Car waxes made with nano-sized polishing agents provide a better shine due to its ability to fill-in tiny blemishes in automotive paint finishes. There are several antibacterial cleansers that use nanoemulsion technology to kill pathogens. Special dressings for burns provide antimicrobial barrier protection by using silver nanoparticles. Several clothing companies have marketed new brands of non-stain nanotechnology fabrics that can resists spills, repels a range of liquids and keep the body cool and comfortable. Many sunscreen product uses zinc oxide nanoparticles that protects the skin but does not leave white marks on the skin.

1.1.2 Nanomaterials

Nanomaterials have structural features in between those of atoms and bulk materials and have at least one dimension in the nanometer range. They act as a bridge between single elements and single crystalline bulk structures. Quantum mechanics has successfully described the electronic structures of single elements. The well established bonding such as ionic, covalent and metallic are the basis of solid state structures. The theory for transition in energy levels from discrete for fundamental elements to continuous bands for bulk is the basis of many electronic properties. Thus a thorough understanding of the structure of nanocrystals can provide deep insight in the structural evolution from single atoms to crystalline solids.

Nanomaterials exhibit very interesting size dependent electrical, optical, magnetic and chemical properties compared to their bulk counterparts. This is mainly due: (i) large fraction of surface atoms; (ii) high surface energy; (iii) spatial confinement and (iv) reduced imperfections.[15] Due to their small dimensions, nanomaterials have extremely large surface area to volume ratio, which makes a large fraction of atoms of the materials to be present on the surface resulting in surface dependent material properties. When the size of nanomaterials are comparable to Debye length, the entire material will be affected by the surface properties which in turn enhance and modify the properties.[16] The energy band structure and charge carrier density in the materials can be modified quite differently from their bulk count part, which in turn modifies the electronic and optical properties of materials. Reduced imperfections are an important factor in determining the mechanical properties of nanomaterials. The small size make them free of internal structural imperfections such as dislocations, micro twins, impurity precipitates etc. The specimens of very small dimensions ought to have a much larger range of elastic strain than the bulk metal, either because they are free of dislocations, or the few dislocations present cannot multiply sufficiently to give an observable amount of slip.[17] Moreover, the external surfaces of nanomaterials have less or free of defects compared to bulk materials. Some of the novel properties of nanomaterials over their bulk counterparts are given below:

- Nanomaterials have significantly lower melting point or phase transition temperature due to large fraction of surface atoms. The reduced coordination number of surface atoms greatly increases the surface energy and atom diffusion occurs at relatively lower temperatures. The melting temperature of gold (Au) particles drops to ~ 300 ^{0}C for particles of diameter around 5 nm, which is much lower than the bulk melting temperature of 1063 ^{0}C.
- The mechanical properties of solids strongly depend on the density of dislocations, interface to volume ratio and grain size. An enhancement in damping capacity of a nanostructured solid may be associated with grain boundary sliding or with energy dissipation mechanism localized at interface. A decrease in grain size significantly affects the yield strength and hardness. The grain boundary structure, boundary angle, boundary sliding and movement of dislocations are important factors that determine the mechanical properties of nanostructured materials.

- Optical properties of nanomaterials are significantly different from their bulk counterparts. For example, the optical absorption peak of a semiconductor nanoparticle shifts to a shorter wavelength due to an increased band gap. The color of metallic nanoparticles changes with their sizes due to surface plasmon resonance. The finite size of particle confines the spatial distribution of electrons leading to quantized energy levels. This quantum confinement of electrons is responsible for the interesting optical properties of nanomaterials.
- Nanomaterials have interesting electronic properties compared to bulk crystals. The spherical shape of nanocrystals produces surface stress, resulting in lattice relaxation and changes in lattice constant. It is known that the electron energy band structure and band gap are sensitive to lattice constant. The lattice relaxation introduced by nanocrystal size can affects its electronic properties.
- Certain nanomaterials like graphene and carbon nanotubes have extraordinarily thermal properties compared to their macroscopic counterparts. As the dimension of the nanomaterials is comparable to the wavelength and mean free path of phonons, the phonon transport within the materials will be changed significantly by the phonon confinement and quantization of photon transport, resulting in modified thermal properties. The special structure of nanomaterials can also affect the thermal properties. For example, because of the tubular structures of carbon nanotubes, they have extremely high thermal conductivity along axial directions.[18] The interfaces are also very important for determining the thermal properties of nanomaterials.[19] These interconnected factors determine the special thermal properties of the nanomaterials.

- The magnetic properties of nanomaterials differ from those of bulk mainly due to two reasons. The large surface to volume ratio results in a different local environment for the surface atoms in their magnetic coupling interaction with neighboring atoms, leading to the different magnetic characteristics. Unlike bulk ferromagnetic materials, which usually forms multiple magnetic domains, small ferromagnetic particles could consist of a single magnetic domain. A single particle of a single magnetic domain results in superparamagnetism where the magnetization of the particles are randomly distributed and are aligned only under an applied magnetic field, and the alignment disappears once the external field is removed.
- Chemical properties (reactivity) of nanomaterials are different from bulk materials due to its high surface energy and surface area. A large percentage of surface atoms greatly increase the surface activities. The unique surface structure, electronic states and largely exposed surface area stimulate and promote chemical reactions. Thus nanomaterials find great applications in catalysis and sensor devices.

The unusual properties of nanomaterials have been employed in a variety of applications. For instance, the size dependent band gap of semiconductors such as CdSe is being exploited in solar cell designs.[20] These colloidal quantum dots are now widely employed as targeted fluorescent labels in biomedical applications, light emitting diodes and lasers. Metal nanoparticles serve as model system to probe the effects of quantum confinement of electronic, magnetic and other related properties.[21] They have also been widely exploited for use in photography, catalysis, biological labeling, photonics, optoelectronics, information storage and surface enhanced Raman scattering.[22, 23] Hollow nanocrystals offer possibilities in material design for applications in catalysis, nanoelectronics, nano-optics, drug delivery systems and as building blocks for lightweight structural materials.[24] The mixing of polymers and nanoparticles open up pathways for engineering flexible composites that exhibit improved electrical, optical or mechanical properties.[25] Recently, graphene and carbon nanotubes have attracted great interest in many fields of science owing to their outstanding physical properties and potential for applications. Graphene has exciting applications in electronics, electric batteries, field emitters, spintronics, gas sensors, quantum computing etc.[13] Carbon nanotubes have found many applications in the generation of conductive and high-strength composites, energy storage, energy conversion devices, sensors, field emission displays, radiation sources, hydrogen storage media, nanometer sized semiconductor devices, probes and interconnects.[11]

Over the last few decades, the synthesis of nanomaterials has been intensively pursued because of their fundamental scientific interest and technological applications. For many future applications, size controlled synthesis of uniform sized nanocrystals is very important. There are two different approaches to synthesize nanocrystals: “top-down” and “bottom-up” approaches, which utilize physical methods and solution-phase colloidal chemistry respectively. The advantage of the physical methods is the production of large quantity of nanocrystals. However, the synthesis of uniform-sized nanocrystals and their size control is very difficult to achieve by this approach. Colloidal chemical synthetic methods can be used to synthesize uniform nanocrystals with controlled particle size, but the amount of particles produced is generally limited to grams. Furthermore, various-shaped nanocrystals, including nanorods and nanowires, can be synthesized by varying the reaction conditions. Grinding and mechanical milling are the commonly used “top-down” approach for nanoparticle synthesis. Most common “bottom-up” approaches include vapour phase methods like physical and chemical vapour deposition; liquid phase methods like colloidal, sol-gel, micro emulsion, hydrothermal and polyol methods; gas phase synthesis methods like flame pyrolysis, electro-explosion, laser ablation and plasma synthesis techniques. Other novel production methods includes radiation (γ, UV-visible, microwave and ultra sound) assisted synthesis, electrodeposition, supercritical fluid mediated synthesis and biological techniques.

Among different nanoparticles, magnetic nanoparticles and ferrofluids are intensively studied owing to their applications in diverse fields such as magnetic refrigeration, catalysis, cell labeling, cell separation, contrast agents for magnetic resonance imaging (MRI), selective removal of cancer cells and drug delivery.[26] Size dependent magnetic properties of nanoparticles is exploited for information storage to achieve recording densities of an order of magnitude larger than that are currently available.[27] Magnetic separations at very low magnetic field gradients using 12 nm sized magnetite nanoparticles are employed for water purification and simultaneous separation of complex mixtures.[28] Incorporating magnetic nanoparticles into a polymer matrix can have significant impact on wide range of material properties, including mechanical strength, conductivity, permeability, catalytic activity, optical and magnetic properties.[29] Ferrofluids are being used in seals, bearings, dampers, stepping motors, loudspeakers and sensors.[30]

1.1.3 Nanofluids

Recently, colloidal dispersions of nanometer-sized particles in traditional heat transfer fluids, popularly known as nanofluids, have been attempted as a new class of nanoengineered coolants.[31, 32] With constantly increasing thermal loads, due to smaller features of microelectronic devices and higher power outputs, there is an urgent need to develop advanced cooling techniques and innovative heat transfer fluids with better heat transfer performance than those presently available. The reliability and speed of electronic and optoelectronic devices strongly depend on temperature and hence materials with very high thermal conductivities (k) are required to remove the heat generated from the devices. The low k of conventional heat transfer fluid is a serious limitation in improving the performance and compactness of engineering equipments.

By considering the fact that metallic solids possess higher k than fluids, it was speculated that fluids containing suspended solid metallic or nonmetallic particles could exhibit significantly higher thermal conductivities than that of conventional heat transfer fluids. Earlier studies on k of suspensions with millimeter and micrometer-sized particles encountered problems of rapid settling of particles, clogging of flow channels and increased pressure drop in the fluid. Nanoparticles, owing to their small size, can remain suspended in base fluids and thereby reduce erosion and clogging. Therefore, there have been continuing interests on nanofluids in cooling applications.

1.2 Overview of Thermal Conductivity Studies in Nanofluids

Nanofluids got intense scientific attention after the first report of unusual k enhancement for copper (Cu) nanofluids, at very low particle loading.[33] Subsequent to that, numerous theoretical and experimental studies have been carried out on thermal conductivity of nanofluids.

Experimental study on nanofluid conductivity is performed with nanoparticles of oxide, nitride and carbide ceramics, metals, semiconductors, metal alloys, single and multi-walled carbon nanotubes (SWCNTs, MWCNTs) etc. In addition, new materials and structures with fascinating properties like graphene and graphene oxide nanosheets have been used for the preparation of nanofluids.[34-36] Despite numerous experimental studies on k of nanofluids, it is not clear whether the k enhancement in nanofluids are anomalous or it can be described by the effective medium theory (EMT) of Maxwell.[37]

Previous reports show that k of nanofluids depends on many factors like volume fraction (ϕ), nanoparticle size, shape, presence of additives, pH, temperature, nature of base fluid and nanoparticle material etc. The earlier reports show enhancement in k ratio (k/k_f, where k is the nanofluid thermal conductivity and k_f is the base fluid thermal conductivity) beyond EMT predictions,[38-59] whereas recent reports show k/k_f enhancement within the predictions EMT.[43, 60-70] Recent systematic studies, led by Buongiorno of MIT and thirty research groups around the globe, on a series of stable nanofluids produced by the same manufacturer using the same production protocol show modest enhancement in k in polyalphaolefin lubricant (PAO) based alumina nanofluids at low and high particle concentrations. By analyzing large number of experimental data, Eapen et. al. have shown that almost all the reported k data are enveloped by the upper and lower Maxwell (H-S) mean-field bounds and the lack of consensus in nanofluid k reports arises because of differences in aggregation structures that arise from colloidal chemistry, thermodynamic conditions and external fields.[71] Likewise, there are conflicting reports on the effect of particle size and temperature on k of nanofluids. Few reports show an enhancement in k/k_f with decrease in particle size [49, 51-53, 72-80] while others show a decrease in k/k_f with decrease in particle size.[62, 69, 81-85] An increase in nanofluid k with temperature is reported in many cases,[73, 86] [38, 49, 53, 54, 72-74, 76, 87-105] whereas a few studies show invariant k with temperature.[62, 82, 106-108] [61, 69, 109-111] [35] [34, 63, 112-114] There are also reports of reduction in k/k_f with increase in temperature.[115, 116]

Majority of the studies showed an enhancement in k with an increase in particle aspect ratio.[42, 60, 70, 114, 117-123] There are conflicting reports on the effect of nanoparticle material on k of nanofluids. Many reports show that the k enhancement of nanofluid is higher when the suspended nanoparticles have higher k,[73, 124-127] whereas other studies show k of nanoparticles is not dependent on the k of nanofluids.[32, 39, 41, 54, 126, 128, 129] A decrease in k ratio with the increase in k of base fluid is reported in most of the studies.[32, 35, 60, 113, 124, 127, 130-133] Few studies have shown that the presence of additives can improve the dispersion stability of nanofluids which results an enhancement in the k value.[33, 121, 125, 134] Previous reports show that the stability and k enhancement of nanofluids is dependent on pH.[96, 124, 125, 131, 134-136] Few studies show that the effective k of nanofluids is linked to ultra-sonication power and its duration that influences the particle dispersibility and average cluster size.[39, 103, 124, 128, 129, 137-139]

Many mechanisms are put forward to account for the k enhancement of nanofluids, which are liquid layering around the nanoparticle surface, ballistic phonon transport, Brownian motion induced microconvection and the aggregation of nanoparticles.[140] Unfortunately, none of the heat transport models could explain the wide spectrum of k data reported in various nanofluids. After detailed investigations, Brownian motion induced convection and effective conduction through percolating nanoparticle paths are considered as the two most probable mechanisms responsible for the enhanced heat conduction in nanofluids.[141, 142] More recent systematic studies reveal that the conduction path through agglomerates is one of the most significant factors responsible for the dramatic enhancement of k.[61, 71]

1.3 Overview of Rheological Studies in Nanofluids

Improved dispersion stability with least enhancement in viscosity (η) is inevitable for the practical applications of nanofluids. Rheological properties of nanofluids are strongly related to the nanofluid's microstructure. Depending on the particle concentration and the extent of particle-particle interactions, nanoparticles can be well dispersed or agglomerated in suspension. Agglomeration and clustering of nanoparticles can lead to an undesirable η increase in nanofluids. Therefore, a proper understanding of η and k enhancement of nanofluid is a prerequisite for effective utilization of nanofluids for various applications.

Measurements show Newtonian nature of nanofluid η (i.e. η does not vary with shear rate) in many cases.[95, 117, 143-148] However there are reports on non-Newtonian (i.e. η varies with shear rate) nature of nanofluid η as well.[102, 105, 117, 148-154] Many reports show that an increase in η is an indication of aggregation in nanofluids.[69, 147, 150-152, 155-160] Recent systematic studies on η measurements in nanofluids show that the shear η increase is much more dramatic than predicted by the Einstein model.[69, 80, 98, 115, 117, 143, 145, 147, 153, 160-163] In another studies, viscosity of aggregating nanofluids show a shear thinning behavior, which is marked by very high low-shear η value followed by a progressive decrease in η at high shear rates.[150, 157]

Temperature dependent rheological studies show a decrease in nanofluid η with increase in temperature both for metal and metal oxide nanofluids.[90, 92, 115, 117, 145, 161, 164] However, there are few reports which demonstrate an invariant nature of relative nanofluid η with temperature.[63, 113, 144, 146]

1.4 Motivation

For better understanding of the k of nanofluids, it is necessary to use model nanofluids with long term stability. Moreover, colloidal chemistry, sedimentation, and agglomeration are some of the important issues to be looked at carefully during k measurements. For fundamental and practical applications in thermal engineering, a proper understanding of the role of η on k enhancement in nanofluids is a prerequisite. Even if there are many studies on the effect of aggregation on k of nanofluids, a systematic k study together with rheology, dynamic light scattering (DLS) and microscopy is still lacking. Further, to confirm the effect of aggregation on the thermal conductivity, a control on the aggregation mechanism and simultaneous measurement of both the aggregation kinetics and the k are essential. Towards this goals, systematic k studies in nanofluids with particle size < 10 nm (together with η, DLS and microscopy studies) are pursued to provide better insight into k enhancement in nanofluids.

1.5 Objectives

The objectives of the present study are the following:

- To synthesize nanofluids with particle size < 10 nm with long term stability and to study their thermal properties.
- To probe the effect of Brownian motion induced convection and nanoparticle aggregation on k of nanofluids.
- To study the thermal conductivity enhancement in nanofluids during the formation of linear aggregates (chains).

- To probe the effect of nanoparticle aggregation on k, η and size distribution of stable and unstable nanofluids.
- To study the effect of surface modification on thermal and rheological properties of nanofluids.
- To obtain better insights into the effect of particle size on k enhancement, especially in very small particle size range (3–10 nm), which were not investigated so far.
- To compare the temperature dependent k, η and particle size distribution of aqueous and nonaqueous nanofluids stabilized with a monolayer of surfactants.
- To study the tunable k and η of magnetically polarizable nanofluids.

To realize the above objectives, stable colloidal suspensions of magnetite (Fe_3O_4), copper oxide (CuO) and silver (Ag) nanoparticles of average size < 10 nm are prepared for these studies.

1.6 Overview of the Thesis

This thesis reports systematic studies on the synthesis and characterization of nanofluids and their thermal and rheological properties. It consists of seven chapters and the details of each chapter are summarized below.

Chapter 1 gives a brief introduction to nanotechnology, nanomaterials, nanofluids and their applications. A detailed discussion on magnetic nanoparticles and ferrofluids is presented. Literature survey on thermal and rheological studies of nanofluids, objectives and the motivation for the present work is also given. **Chapter 2** describes the nanoparticle synthesis methods, the experimental techniques used for nanoparticles characterization, details of k measurement technique and rheology measurements. **Chapter 3** presents the size controlled synthesis of Fe_3O_4, CuO and silver Ag nanoparticles and the characterization results of above nanoparticles. **Chapter 4** describes the k as a function of ϕ in stable Fe_3O_4 and unstable CuO nanofluids. Moreover, the role of aggregation on k and η of nanofluids is studied by following the time dependant k, average particle size, microstructure and η of stable and aggregating nanofluids. **Chapter 5** describes the thermal and rheological properties of kerosene and hexadecane based Fe_3O_4 nanofluids in presence of linear aggregates. A new approach to tune the thermal properties of magnetic nanofluids from low to very high values by varying the magnetic field strength and its orientation is also described. This chapter also focuses on the experimental demonstration of tunable k and η of magnetically polarizable nanofluids. **Chapter 6** describes temperature-dependent k, η and particle size distribution in aqueous and nonaqueous nanofluids stabilized with a monolayer of surfactant. **Chapter 7** describes size dependant k and η studies in magnetically polarizable nanofluids with long term stability both in presence and absence of external magnetic field. **Chapter 8** summarizes the results obtained, conclusions drawn and perspectives.

Chapter – II

Synthesis and Characterization Techniques

Contents

Chapter II | Synthesis and Characterization Techniques

2.1 Introduction

Magnetite (Fe_3O_4) is a ferrimagnetic mineral with inverse spinel structure. It consists of oxide ions in the cubic close-packed arrangements in which 1/3 rd of tetrahedral interstices and 2/3 rd of octahedral interstices coordinate with oxygen. All Fe^{2+} ions occupy the octahedral interstices and half of the Fe^{3+} ions occupy the tetrahedral interstices and remaining half of the Fe^{3+} in octahedral interstices. Electron spins of Fe^{3+} ions in octahedral interstices are aligned antiparallel to those in tetrahedral interstices, and hence no net magnetization is observed from these ions. The Fe^{2+} ions align their spins parallel to Fe^{3+} ions in adjacent octahedral sites leading to a net magnetization. Hence, Fe_3O_4 exhibits ferrimagnetism and the reported value of Curie temperature of bulk Fe_3O_4 is 858 K.[165]

The Fe_3O_4 nanoparticles of very small size exhibit superparamagnetism with zero remanence and coercivity.[166] As particle size decreases, the number of magnetic domains per particle decreases down to the limit where it is energetically unfavorable for a domain wall to exist. At first Frenkel and Dorfman proposed that ferromagnetic materials can have single magnetic domain below a critical size (D_S).[167] In superparamagnetism, each particle behaves like a single magnetized domain, where the system is in a state of uniform magnetization and behaves like a small permanent magnet. In such cases, even when the temperature is below the Curie or Neel temperature, the thermal energy is sufficient to change the direction of magnetization of the entire crystallite. The resulting fluctuations in the direction of magnetization cause the magnetic field to average to zero. Thus the material behaves in a manner similar to paramagnetism, except that instead of each individual atoms being independently influenced by an external magnetic field, the magnetic moment of the entire crystallite tends to align with the magnetic field. Theoretically estimated values of D_S are about 14 nm for iron (Fe), 70 nm for cobalt (Co), 166 nm for maghemite (γ -Fe_2O_3), 128 nm for Fe_3O_4 and 40 nm for cobalt ferrite ($CoFe_2O_4$).[168]

Uniform-sized ferrite nanoparticles have attracted considerable attention because of their broad applications, which include magnetic storage media, ferrofluids, Magnetic Resonance Imaging (MRI), magnetically guided drug delivery, medical diagnosis, and magnetic field assisted cancer therapy etc.[27, 169-171] Among ferrites, magnetite nanoparticles are of great importance due to their high saturation magnetization value, ease for tagging bio-molecules and biocompatibility.[172]

In recent years, copper oxide (CuO) nanoparticles have attracted increasing interests due to both fundamental and practical reasons. It belongs to monoclinic crystal system where the copper atom is coordinated by four oxygen atoms in an approximately square planar configuration. CuO is a semiconducting compound with a narrow band gap and is used for photoconductive and photothermal applications.[173] Copper oxide nanoparticles are industrially important material that has been used in applications such as gas sensors,[174] magnetic storage media,[175] solar energy transformation,[176] photovoltaic cells[177] and catalysis.[178, 179] Recently, CuO nanoparticles have been used as an antimicrobial agent.[180]

Silver (Ag) nanoparticles are attractive due to their remarkable size and shape dependent optical properties, highest efficiency of plasmon excitation, and highest electrical and thermal conductivity in the bulk among all the metals.[181, 182] These special properties have led to promising applications of silver nanoparticles in catalysis for the selective oxidation of styrene,[183] environmentally friendly antimicrobial coatings,[184] real-time optical sensors,[185] printed electronics,[186] photonics[187] etc. Due to the potential applications, the size controlled synthesis of Ag nanoparticles is an area of intense research for the last two decades. Silver has face centered cubic crystal structure.

2.2 Synthesis of Nanoparticles

Much progress has been made over the last one decade on the synthesis of monodisperse spherical nanocrystals because of their novel properties and potential applications. The synthesis of nanomaterials spans inorganic, organic, and biological systems and manipulation with control of structure, size, and shape. Earlier efforts had been limited to produce nanoparticles in uniform sizes.[188] Now, with the emerging new synthesis techniques, it is possible to synthesize them not only in uniform sizes but also in desired morphologies such as rods, tubes, cubes, prisms etc.[21, 189] Advances in synthesis techniques have allowed creation of other novel structures such as core shell particles,[190] hollow particles,[191] heterostructured nanoparticles[192] etc. An important research direction in current nanoparticle synthesis is the expansion from single component nanoparticles to hybrid nanostructures that possess two or more functional properties.[193]

Large scale and size controlled synthesis of magnetite nanoparticles is essential for realizing its potential applications. There exist a wide range of synthesis methods for magnetite nanoparticles such as mechanical milling,[194] mechano-chemical reactions,[195] hydrothermal,[196] solvothermal,[197] reverse micellar method,[198] sol-gel,[199], co-precipitation,[200-203] thermal decomposition,[204] vaporization condensation,[205] electrodeposition,[206] bacterial synthesis[207] etc. Each synthesis technique has its own merits and demerits and is useful for preparing magnetic nanoparticles with specific properties. For example, large scale synthesis of magnetite nanoparticle is possible by mechanical milling.[194] However, it is difficult to have a control on nanoparticle size and distribution in the above technique. Though fairly monodispersed nanoparticles can be synthesized by solvothermal route,[197] it requires high temperature reaction, tedious washing procedure and use of toxic organic solvents. Therefore, particles prepared by this technique are not preferable for biomedical applications. Coprecipitation allows the synthesis of magnetite nanocrystals by a simple, inexpensive, and environmentally friendly procedure.[201-203] Since the reaction in this technique occurs at low temperature, it can produce biocompatible materials with less impurity in aqueous phase. Moreover, it is possible to tune the size of nanoparticles during coprecipitation by changing the reaction conditions like temperature, precursor addition rate, nature of alkali, stirring speed, digestion time and pH of the reactants.[208]

Due to widespread application of CuO nanoparticles, there has been a renewed interest in understanding the fundamental physical properties of CuO, as well as for improving its performance in various applications. These interests have stimulated the development of several techniques for preparing CuO nanoparticles, such as sol-gel,[209] precipitation,[210] sonochemical reactions,[211] microwave irradiation,[212] alcohothermal reactions,[213] and mechanical milling methods.[214] Copper oxides nanoparticles can be conveniently obtained by thermal decomposition of copper salt precursors in the solid state.[215] But this method has difficulty in controlling the particle sizes and shapes. Microemulsion technique, which involves injection of the dissolved reactants into a hot surfactant solution, had the difficulties in producing monodispersed CuO nanocrystals.[216] Sonochemical method to synthesize CuO nanoparticle is elaborate and can produce nanocrystals of low yield.[217] Alcoho-thermal method is also not appropriate for the preparation of CuO nanoparticles in large amounts.[218] Moreover, the organic solvents of large amount are required for the preparation process. Precipitation allows large scale synthesis of CuO nanoparticles. Beside it is a simple, safe, cost effective and environment friendly method.[219] Moreover, the size and morphology of CuO nanoparticles can be varied by changing the reaction conditions like temperature and addition of precipitating agent.[220]

A variety of methods to prepare Ag nanoparticles have been available.[221-226] With regard to reducing agents used in the synthesis, three principal concepts are quite distinct in the “wet” chemical reduction of silver ions and the preparation of silver nanostructures.[227] The first one involves the reduction of silver ions with γ-ray,[228] ultraviolet or visible light,[229] microwave[230] or ultrasound irradiation.[231] The second approach refers to the formation of silver colloids with relatively strong reducing agents such as sodium borohydride,[232] hydrazine[233] and tetrabutyl ammonium borohydride.[234] The third approach is thermal decomposition which involves the reduction of silver by prolonged refluxing in the presence of weak reducing agents, such as glucose, organometallic compounds, sodium citrate, dimethylformamide, potassium bitartrate, ascorbic acid, and alcohols or polyols.[227] Among the three different approaches discussed above, the second one is more reliable. The synthesis of Ag nanoparticles with the aid of reducing agents is often been performed in the presence of a capping agent or in microemulsions at room temperature. With fatty acids or amines as ligands, and by using strong reducing agents, silver nanoparticles with narrow size distribution can be obtained in gram scale in a single phase.[235], Strong reducing agents produce silver nanoparticles with smaller sizes and narrower size distributions because of the rapid nucleation of high density nuclei.

2.2.1 Magnetite

The synthesis of magnetite nanoparticles is carried out by precipitating iron salts in alkaline medium. Ferrous sulphate heptahydrate ($FeSO_4.7H_2O$), ferric chloride hexahydrate ($FeCl_3.6H_2O$), 25% aqueous ammonia, oleic acid, 35% hydrochloric acid (HCl), hexane and acetone procured from E-Merck are used for the synthesis. All the chemicals used are GR grade and used without any further purification. Elga water with a resistivity of 8-15 MΩ·cm is used in all experiments. The iron salts used are freshly prepared 0.2 M $FeSO_4.7H_2O$ and 0.4 M $FeCl_3.6H_2O$. The salt solutions are prepared in acidic medium in order to avoid formation of iron hydroxides before initiation of the reaction. The above solutions with 1:1 ratio are mixed at constant stirring. This mixture is heated in a water bath until the required temperature of 60 °C is reached. On vigorous stirring, the above solution pH is increased rapidly to 10.5 by adding 25% aqueous ammonia. The solution turned to black at this stage indicating the formation of Fe_3O_4 nanoparticles. Rapid addition of ammonia allows the formation of excess number of nuclei and vigorous stirring prevents the coagulation of particles. The precipitated particles are left for finite digestion time until the nucleated particles attain a thermodynamically equilibrium state. Overall chemical reaction can be written as

$$2Fe^{3+} + Fe^{2+} + 8OH^{-} \rightarrow Fe_3O_4 + 4H_2O \tag{2.1}$$

To prepare stable water based magnetite nanofluid called ferrofluid, particles are coated with tetramethyl ammonium hydroxide surfactant ($C_4H_{13}NO$). Since, electrostatic stabilization is pH and salt sensitive, presence of salt ions in solvent may destabilize the particles. The magnetite nanoparticles prepared by this method are washed with triply distilled water for several times until the pH become 7, to remove the ionic impurities trapped or adhered to the particles. The solution is tested for Cl^- ions with silver nitrate solution. After repeated washings, the particles are coated with tetramethyl ammonium hydroxide (TMAOH) at higher pH at constant stirring.

To prepare stable oil based ferrofluid, particles are coated with oleic acid ($C_{18}H_{34}O_2$). After the preparation of magnetite nanoparticles, the solution is digested for 30 minutes and 20 ml of oleic acid is added to the dispersion. Then, the dispersion pH is adjusted to 9.5 with dilute hydrochloric acid and the temperature is increased to 70 ^{0}C. At the same pH, temperature and stirring speed, the solution is kept for 30 minutes to finish the coating process. An alkaline medium and higher temperature favor the oleic acid adsorption on magnetite. In the presence of ammonia, oleic acid forms water soluble ammonium oleate salt. The higher temperature helps to increase the solubility and decreases the viscosity of the surfactant. In alkaline medium, the surface of nanoparticles will have surface bound OH^- ions and hence they are charge stabilized. At this stage, ionized ammonium oleate surfactant forms ammonium cation and oleate anion. The oleate anions replace the magnetite surface bound OH^- ions by ion-exchange adsorption phenomena. After ammonium oleate adsorption, particles become hydrophilic in nature and cannot be dispersed in non-polar solvents. The neutralization of dispersion has been achieved by eliminating excess ammonia by heating. After this step, the temperature is increased to 79 ± 1 ^{0}C in order to eliminate the excess ammonia and the protonation of adsorbed and un-adsorbed ammonium oleate. After ammonia is excluded, particles are separated from the dispersion. The top water layer with excess salts is discarded. The surfactant coated particles have been washed with water at 60 ^{0}C, until the pH became 7 to remove the ionic impurities trapped or adhered to the coagulum. Later, the water washed particles are dispersed in hexane. The hexane dispersion is treated with acetone to induce aggregation of particles. The aggregated particles are then separated from dispersion by centrifugation at 2500 rpm for 30 minutes. The hexane-acetone mixture washing procedure is repeated to remove excess surfactant in the dispersion. The surfactant coated magnetite nanoparticles are dried at room temperature in an inert atmosphere.

2.2.2 Copper Oxide

For the synthesis of copper oxide nanoparticles, cupric acetate dihydrate [Cu $(CH_3COO)_2.2H_2O$], glacial acetic acid (CH_3COOH), sodium hydroxide (NaOH), acetone and ethanol are procured from E-Merck. All the chemicals are of GR-grade and used without any further purification.

The synthesis of copper oxide nanoparticles is carried out by precipitating copper salt in alkaline medium.[138] The copper salt used is freshly prepared 0.2 M Cu $(CH_3COO)_2.2H_2O$. The salt solution is mixed with 1ml glacial acetic acid and the resultant solution is heated at a constant stirring speed of 1000 rpm until required temperature of 60 °C is reached. Higher temperature is favored because of higher reaction rates, which produces large amounts of nuclei to form in a short time, and the aggregation of crystals is inhibited. Glacial acetic acid is used to prevent the hydrolysis of the copper acetate solution. On vigorous stirring, the above solution pH is increased rapidly to 10.5 by adding NaOH pellets where a black precipitate of CuO is formed instantly. At the same pH, temperature and stirring speed, the solution is kept at a digestion time of 30 minutes. Overall chemical reaction can be written as

$$Cu(CH_3COO)_2 + 2NaOH \rightarrow CuO + 2Na(CH_3COO) + H_2O \qquad (2.2)$$

After cooling to room temperature, particles are separated from the dispersion. The top water layer with excess salts is discarded. The particles are washed with water, ethanol and acetone. They are separated from dispersion by centrifugation at 2500 rpm for 30 min and dried at room temperature in an inert atmosphere.

2.2.3 Silver

For the synthesis of silver nanoparticles, silver nitrate ($AgNO_3$), sodium borohydride ($NaBH_4$), oleylamine, hexane and ethanol are procured from E-Merck. All the chemicals are of GR-grade and used without any further purification. The synthesis of silver nanoparticles is carried out by reducing silver salt using $NaBH_4$. The silver salt used is freshly prepared 0.1 M $AgNO_3$ solution in water. The salt solution is stirred using a mechanical stirrer at a rotating speed of 1000 rpm. To the above solution, oleylamine is added under continued stirring. As oleylamine is insoluble in water, the resultant reaction mixture becomes turbid. To the above mixture, hexane is added under continuous stirring. The oleylamine goes to the organic layer and two distinct clear layers are formed, which comprise of an aqueous silver salt solution at the bottom and a hexane-oleylamine mixture on the top. On vigorous stirring, the aqueous $NaBH_4$ solution is added to the above mixture where a black precipitate of silver nanoparticles is produced instantaneously. The resultant reaction mixture is stirred for 30 minutes to complete the transfer of silver nanoparticles from polar (water) to nonpolar layer (hexane). Overall chemical reaction can be written as

$$AgNO_3 + NaBH_4 \rightarrow Ag + 1/2H_2 + 1/2B_2H_6 + NaNO_3 \qquad (2.3)$$

After continued stirring, the silver nanoparticles are completely transferred to the organic top layer. Here, oleylamine act as a capping agent for Ag nanoparticles. Moreover, it helps to transfer the silver nanoparticles from polar to nonpolar medium as there is a chance for metal nanoparticles to undergo oxidation into metal oxide in a polar medium. The clear water layer at the bottom shows no absorption peak in UV spectrum, indicating the absence of Ag nanoparticles. The silver nanoparticles in the hexane layer is separated by centrifugation, washed with ethanol and water and dried at room temperature in an inert atmosphere.

2.3 Characterization Techniques

2.3.1 X-Ray Diffraction

The X-ray Diffraction (XRD) is used as a primary tool to characterize the crystal structure and crystallite size of nanoparticles. It exploits the wave nature of electromagnetic radiation. The phenomenon of diffraction occurs whenever wave motion of an electromagnetic wave encounter a set of regularly spaced scattering objects, provided the wavelength of electromagnetic is in the same order of distance between the scattering centers. Since the wavelength of X-rays (0.1 to 1 Å) is equal to the interatomic distance in crystals, X-ray diffraction can be observed when X-rays interact with crystalline materials.[236] If many atoms are scattering the X-rays together, scattered waves from all the atoms can interfere. If the scattered X-rays are in phase, they interfere constructively resulting diffracted beams in specific directions. These directions are governed by the wavelength (λ) of incident X-rays and the nature of crystalline sample. Bragg's law, formulated by W. L. Bragg in 1913, relates the wavelength of the X-rays to the spacing of the atomic planes (d_{hkl}) as $n\lambda=2d_{hkl}\sin\theta$, where θ is the angle of incident X-rays and 'n' is the order of diffraction. Bragg's law is extremely important in indexing X-ray diffraction pattern and for determining crystal structure of materials.

The three basic components of an X-ray diffractometer are the X-ray source, specimen and the X-ray detector, all lie on the circumference of a circle, which is known as the focusing circle. The angle between the plane of the specimen and the X-ray source is θ, the Bragg angle. The angle between the projection of the X-ray source and the detector is 2θ. For this reason the X-ray diffraction patterns produced with this geometry are often known as θ-2θ scans. In the θ-2θ geometry, the X-ray source is fixed, and the detector moves through a range of angles. A 2θ

range from 30° to 140° is an example of a typical scan. X-rays are generated by directing an electron beam of high voltage on a metal target anode inside an evacuated X-ray tube. Copper is the most frequently used target and the typical operating conditions are 40 kV and 30 mA. The unwanted k_β radiation is removed using a monochromator. On the X-ray source side, a line source of X-rays passes through a series of slits called sollar slits which consist of a series of closely spaced parallel metal plates that define and collimate the incident beam. In a typical X-ray diffraction experiments, a thin layer of crystalline powder is spread onto a planar substrate, which is a nondiffracting material such as a glass microscope slide and exposed to the X-rays. The quantity of powder used for each experiments is quite small, usually a few milligrams. After the beam has been diffracted by the specimen, it passes through another set of slits. The antiscatter slit reduces the background radiation, improving the peak to background ratio, making sure that the detector can receive X-rays only from the specimen area. The beam converges on passing the receiving slit, which defines the width of the beam admitted to the detector. An increase in slit width increases the maximum intensity of the reflections in the diffraction pattern. Three main types of X–ray detectors used in X-ray diffractometer are proportional, scintillation and solid state detectors.

Ideally, the specimen should contain numerous small, equiaxed and randomly oriented grains. In a powder or a polycrystalline material in general, the grains are often randomly oriented, and some grains will always be oriented in a favorable direction with respect to the X-ray beam, to allow the diffraction occur from a specific set of lattice planes. Each set of lattice planes in the crystal having spacing $d_{hkl(1)}$, $d_{hkl(2)}$, $d_{hkl(3)}$,…, will diffract at different angles θ_1, θ_2, θ_3,…, where θ increases as 'd_{hkl}' decreases in such a way to satisfy Bragg's law. The intensity of the diffracted beam at each of these different angles is detected, and forms the X-ray diffraction pattern. The intensity is proportional to the number of X-ray photons of a particular energy that has been counted by the detector for each angle of 2θ.

Phase identification is accomplished by comparing the data (peaks and relative intensities) from a very large set of "standard" data provided by the Joint Committee on Powder Diffraction Standards (JCPDS). It is possible to determine the average crystallite size and lattice strain in a powder specimen by X-ray peak broadening analysis. If the crystallites are smaller, the number of parallel planes available is too small for a sharp diffraction maximum to build up, and peaks in the diffraction pattern become broadened. The broadening of diffraction peaks arises mainly due to three factors: Instrumental effects; crystallite size and lattice strain. The broadening is evaluated by measuring the width in radians, at intensity equal to half the maximum of intensity (FWHM). Scherrer has derived an expression for broadening of X-ray diffraction peaks due to small crystallite sizes which is given by $B_{\text{crystallite}} = C\lambda / d\cos\theta$, where λ is the wavelength of X-rays used, θ is the Bragg angle, 'd' is the average crystallite size measured in a direction perpendicular to the surface of the specimen and 'C' is a constant that depends on shape of the crystallite (for spherical particles C = 0.9). The above equation is known as Scherrer equation is derived based on the assumptions of Gaussian line profiles and small cubic crystals of uniform size.

In the present study, Philips-X'pert MPD X-ray diffractometer is used to obtain X-ray diffraction patterns of the samples. 2θ values are taken from 20^{o} to 70^{o} a step size of 0.02^{o}. A copper target serves as X-ray source to producing CuK_{α}radiation. The samples are dusted on to plates with low background. Thin layered dried samples (30 ± 2 mg) spread over 5 cm^{2} plate area are prepared to minimize the error in peak location and the broadening of peaks due to reduced thickness of the sample. Control, acquisition and preliminary analysis of the data are performed by the Philips X'pert pro software. The peaks of the X-ray diffraction pattern are compared with the available standard data to confirm the crystal structure. The peak position and full width at half maximum are determined by fitting the peak with voigt function using the PEAKFIT program from Jandel Scientific.

2.3.2 Transmission Electron Microscopy

One of the most powerful tools for determining particle size and morphology is Transmission Electron Microscopy (TEM).[237] This technique gives particle size, crystallite size and can provide details of size distribution. In many cases, aggregates of smaller particles can be discerned. TEM enables one to see things as small as the order of a few angstroms. If the nanoparticles consist of more than one phase and the phases provide enough contrast, then the individual phases may also be visible. The possibility for high magnifications has made TEM a valuable tool in both medical, biological and materials research. The TEM operates on the same basic principles as the light microscope but uses electrons as source instead of light. Theoretically, the maximum resolution one can obtain with a light microscope has been limited by the wavelength of light used to probe the sample. The image resolution in TEM in terms of the classic Rayleigh criterion for visible light microscopy, which states that the smallest distance that can be resolved is approximately given by $\delta = 0.61\lambda/\mu\sin(\theta)$, where λ is the wavelength of the radiation, μ is the refractive index of the viewing medium and θ the semi-angle of collection of the magnifying lens. For green light (λ=400 nm) with oil immersion ($\mu \sim 1.7$) and $\sin(\theta) \sim 1$, estimated resolution of an optical microscope is ~ 150 nm. TEM uses electrons as light source, which has much lower wavelength compared to light, thus making the resolution ten thousand times better than a light microscope. For a 200kV electrons ($\lambda \sim 0.0025$nm), with vacuum ($\mu \sim 1$ since no medium in electron lenses) and $\sin \theta \sim \theta \sim 0.1$ radians, resolution is ~ 0.02 nm for an electron microscope.

When electrons are accelerated up to high energy levels (few hundred keV) and focused on a material, they can scatter or backscatter elastically or inelastically, or produce many interactions, source of different signals such as X-rays, Auger electrons or light. The scattering processes experienced by electrons during their passage through the specimen determines the kind of information obtained. Elastic scattering involves no energy loss and gives rise to diffraction patterns. Inelastic interactions between primary electrons with grain boundaries, dislocations, defects, density variations, etc., can cause complex absorption and scattering effects, leading to a spatial variation in the intensity of the transmitted electrons. In a typical experiment, a stream of electrons is formed by an electron source and accelerated (~100–400 kV) towards a thin specimen in vacuum. The beam is confined and focused by apertures and magnetic lenses. Electron beam-specimen interaction generates elastic and inelastic events. The objective lens forms a diffraction pattern in the back focal plane and a magnified image of the sample in image plane. A number of intermediate lenses are used to project either the image or the diffraction pattern onto a fluorescent screen or film. The electron gun uses LaB_6 thermionic emission source or a field emission source. The vacuum system is one of the main components in TEM, without which proper functioning of TEM is not possible. Because of strong interactions of electron with matter, gas particles must be absent in the column. Sample is placed on a specimen stage which serves as a platform for in situ observations during annealing, electric field or mechanical stress induced structural analysis of nanostructures. Instead of glass lenses focusing the light in the light microscope, the TEM uses electromagnetic lenses to focus the electrons into a very thin beam. These electromagnetic lenses are used to (de)focus the electron beam, focus image/diffraction pattern, change magnification and to switch between image and diffraction modes. In electromagnetic lenses, a strong magnetic field is generated by passing a current through a set of windings. This field acts as a convex lens, bringing off axis rays back to focus. The image is rotated, to a degree that depends on the strength of the lens. Focal length can be altered by changing the strength of the current. The double condenser system or illumination system consists of two or more lenses and an aperture. The first condenser lens creates a demagnified image of the gun crossover and control the minimum spot size in the rest of the condenser system. The second condenser lens affects the convergence of the beam at the specimen and the diameter of the illuminated area of the specimen. The condenser aperture controls the fraction of the beam which is allowed to hit the specimen and helps to control the intensity of illumination. The objective lens forms an inverted initial image, which is subsequently magnified. In the back focal plane of the objective lens, a diffraction pattern is formed. The objective aperture placed in the back focal plane of the image. Its function is to select those electrons which contribute to the image, and affect the appearance of the image and improve the contrast of the final image. The first intermediate lens magnifies the initial image that is formed by the objective lens. This lens can be focused on initial image formed by the objective lens or diffraction pattern formed in the back focal plane of the objective lens. This determines whether the viewing screen of the microscope shows a diffraction pattern or an image. Magnification in the electron microscope can be varied from hundreds to several hundred thousands of times by varying the strength of the projector and intermediate lenses.

JEOL 2011 is used for TEM and high resolution TEM (HRTEM) studies. The TEM operated at an accelerating voltage of 200 kV is used to record images. A drop of nanoparticle suspension in acetone is placed over amorphous carbon-coated copper grids at room temperature and then dried overnight under a lamp. In these studies, TEM images have been used to get the size of the particles.

2.3.3 Dynamic Light Scattering

Dynamic Light Scattering (DLS), also known as photon correlation spectroscopy is an important supplementary technique for determining the sizes of particles in solution, particularly when the size distribution is narrow and approximately log normal.[238] The DLS technique is sensitive to total particle size and yields information which is weighted by the square of the particle volume, although the results are generally 'converted' to volume or number weighting.

When a laser beam is shined through a liquid with suspended particles, the beam scatters off those particles in all directions, resulting in a scattering-angle-dependent intensity pattern. When particles are experiencing Brownian motion, the intensity pattern fluctuates randomly. When the particles are very small compared to the wavelength of the light, the intensity of the scattered light is uniform in all directions (Rayleigh scattering); for larger particles (above approximately 250nm diameter), the intensity is angle dependent (Mie scattering). If the light is coherent and monochromatic, a time-dependent fluctuation in the scattered intensity is observed. Measuring the intensity fluctuations at a given scattering angle can yield a great deal of information about the particles that are scattered by laser beam, including the hydrodynamic radius of the suspended particles. The hydrodynamic radius of a particle is the effective radius of an irregularly shaped particle that is used when describing the manner in which particles in suspension diffuse through the suspending medium. For a hard sphere, the hydrodynamic radius equals the radius of the sphere. The randomness of the fluctuation intensity of scattered light allows us to use random statistical methods to analyze that scattering pattern. The most important one is called correlation. If the intensity at a given scattering angle is recorded over a small sample time, the fluctuations of the intensity arising from Brownian motion can be expected to be small. If two such recordings are made from the same scattering angle simultaneously, then two samples can be compared with one another through cross-correlation, which is a measure of how quickly the scattered light intensity changes with time. Autocorrelation is mathematically identical to cross-correlation, except that rather than comparing two signals with one another; one signal is compared with a time-delayed version of itself. Not surprisingly, cross-correlation offers a particular advantage when concentration levels of suspended particles are relatively high, making secondary scattering more likely.

In a DLS experiment the fundamental quantity obtained is the intensity autocorrelation function $G^{(2)}(\tau)$ of the scattered laser light.[239] This has the form

$$G^{(2)}(\tau) = X + Y\left|g^{(1)}(\tau)\right|^2 \tag{2.4}$$

where X and Y are instrumental constants, τ is the delay time, and $g^{(1)}(\tau)$, which is the electric field autocorrelation function that contains the information of interest. For a monodisperse solution of ideal, non-interacting solid spheres

$$\left|g^{(1)}(\tau) = \exp(-\Gamma\tau)\right| \tag{2.5}$$

where Γ is the decay constant. The particle translational diffusion coefficient ‘D’ is readily determined from Γ using

$$\Gamma = q_S{}^2 D \tag{2.6}$$

Here q_S is the magnitude of the scattering vector. The hydrodynamic size d_{hy} is calculated from D via the Stokes-Einstein relationship.

$$D = \frac{k_B T}{3\pi\eta d_{hy}} \tag{2.7}$$

Where, k_B is the Boltzmann constant and T is the temperature.

A typical DLS system comprises of six main components. A laser is used to provide a light source to illuminate the sample within a cell. Most of the laser beam passes straight through the sample, but some are scattered by the particles in the sample. A detector is used to measure the intensity of the scattered light. As particles scatter light in all directions, it is possible to place the detector in any position and it will still detect the scattering. The intensity of the scattered light must be within a specific range for the detector to measure successfully. If too much light is detected, the detector will become saturated. To overcome this, an attenuator is used to reduce the intensity of the laser and hence the intensity of scattering. For samples that do not scatter much light, such as very small particles or samples of low concentration, the amount of scattered light must be increased. In this situation, the attenuator will allow more laser light to pass through the sample. For samples that scatter more light, such as large particles or sample of higher concentration, the amount of scattered light must be decreased. This is achieved by using the attenuator to reduce the amount of laser light that passes through the sample. The scattering light signal from the detector is then passed to a digital signal processing board called correlator. The correlator compares the scattering intensity at successive time intervals to derive the rate at which the intensity is varying. This correlator information is then passed to a computer, where the specialist software will analyze the data and derives the particle size information.

The size distribution of nanoparticles is determined by using a Zetasizer-Nano (Malvern Instrument). It uses a He-Ne laser (4 mW, λ=633 nm) and avalanche photodiode detector. The Zetasizer-Nano measures the scattering information at an angle close to 180° (the detector position is at 173°). There are several advantages in doing this: (i): Because the backscatter is being measured, the incident beam does not have to travel through the entire sample. As light passes through a shorter path length of the sample, then higher concentrations of sample can be measured; (ii): It reduces an effect known as multiple scattering, where the scattered light from one particle is itself scattered by other particles. The effect of multiple scatter is minimum at 180° and (iii): Contaminants such as dust particles within the dispersant are typically large compared to the sample size. Larger particles mainly scatter in forward direction. Therefore by measuring the backscatter, the effect of dust is greatly reduced.

2.3.4 UV-Visible Spectrophotometer

The absorption of electromagnetic radiation in the ultraviolet and visible regions of the spectrum by the substances results in changes in the electronic structure of ions and molecules through the excitations of bonded and non-bonded electrons. UV-Visible spectrophotometer can be used for both qualitative and quantitative investigations of samples. UV-Vis spectroscopy is routinely used for the quantitative determination of different analytes, such as transition metal ions, highly conjugated organic compounds, biological macromolecules and for the surface plasmon resonance absorption of metal nanoparticles. The wavelength at the maximum of the absorption band will give information about the structure of the molecule or ion and the extent of the absorption is proportional to the amount of the species absorbing the light. Quantitative measurements are based on Beer Lamberts Law which is described as $A = \varepsilon_a c l$, A is the absorbance (no units), ε_a is the molar absorbance or absorption coefficient (in $dm^3\ mol^{-1}\ cm^{-1}$), ‘c’ is the concentration (molarity) of the compound in the solution (in $mol\ dm^{-3}$) and ‘l’ is the path length of light in the sample (in cm).

The basic instrumentation consists of a dual light source viz., tungsten lamp for visible range and deuterium lamp for ultraviolet region, grating, monochromator, photo-detector, mirrors and glass or quartz cells. For measurements to be made under visible region, both glass and quartz cells can be used. For the measurements under ultraviolet region, only quartz cell should be used, since, glass cells absorb ultraviolet rays. The grating can be rotated allowing a specific wavelength to be selected. At any specific orientation of the grating, only a single wavelength is successfully passes through a slit. A filter is used to remove unwanted higher orders of diffraction. In a typical measurement, a beam of light from a visible and/or UV light source is separated into its component wavelengths by a prism or diffraction grating. Each monochromatic beam in turn is split into two equal intensity beams by a half-mirrored device. One beam, the sample beam, passes through a small transparent container containing a solution of the compound being studied in a transparent solvent. The other beam, the reference, passes through an identical cuvette containing the solvent alone. The intensities of these light beams are then measured by electronic detectors and compared. The intensity of the reference beam, which should have suffered little or no light absorption, is defined as I_0 and the intensity of the sample beam is defined as I_S. Over a short period of time, the spectrometer automatically scans all the component wavelengths in the manner described. The ultraviolet (UV) region scanned is from 200 to 400 nm, and the visible portion is from 400 to 800 nm. If the sample compound does not absorb light of a given wavelength, $I_S = I_0$. However, if the sample compound absorbs light then $I_S < I_0$, and this difference may be plotted on a graph versus wavelength. Absorption may be presented as transmittance ($T_a = I_S/I_0$) or absorbance ($A = \log I_0/I_S$). If no absorption has occurred, $T_a = 1.0$ and $A = 0$. Different compounds have very different absorption maxima and absorbance. Intensely absorbing compounds must be examined in dilute solution, so that significant light energy is received by the detector, and this requires the use of completely transparent solvents. The most commonly used solvents are water, ethanol, hexane and cyclohexane.

A double beam with photo silicon diode array system LABINDIA (model UV-VIS 3000) is used for the UV-Visible studies. Dilute hexane based dispersion of Ag nanoparticles is used and the spectrum is recorded within the wave length range of 200-70 nm.

2.3.5 Phase Contrast Optical Microscopy

Phase contrast microscopy is an optical microscopy illumination technique in which small phase shifts in the light passing through a transparent specimen is converted into amplitude or contrast changes in the image. As light travels through a medium other than vacuum, interaction with this medium can cause amplitude and phase changes which depend on the properties of the medium. The changes in amplitude leads to familiar absorption of light, which is wavelength dependent and gives rise to colors. In a phase contrast microscope, partially coherent illumination produced by the tungsten-halogen lamp is directed through a collector lens and focused on a specialized annulus positioned in the sub stage condenser front focal plane. Wavefronts passing through the annulus illuminate the specimen and either passes through undeviated or diffracted and retarded in phase by structures and phase gradients present in the specimen. Undeviated and diffracted light collected by the objective is segregated at the rear focal plane by a phase plate and focused at the intermediate image plane to form the final phase contrast image which is observed through the eyepieces. In the present study, the aggregation effect in nanofluids is studied using a Lecia Inverted microscope attached with a JVC camera and frame grabber card. The obtained images are processed using Lecia Win software.

2.3.6 Vibrating Sample Magnetometer

The Vibrating Sample Magnetometer (VSM) is the basic instrument for characterizing magnetic materials. It works on Faraday's law of induction according to which an electromotive field is induced in a conductor by a time-varying magnetic flux. This electric field can be measured, which gives information about the changing magnetic field. If a sample of any material is placed in a uniform magnetic field, created between the poles of an electromagnet, a dipole moment is induced. If the sample vibrates with sinusoidal motion, a sinusoidal electrical signal is induced in suitably placed pick-up coils. The signal has the same frequency of vibration and its amplitude is proportional to the magnetic moment, amplitude, and relative position with respect to the pick-up coils.

A VSM operates by placing the sample in a constant magnetic field. This constant magnetic field will magnetize the sample by aligning the magnetic domains or the individual magnetic spins with the field. As the sample is moved up and down, this magnetic stray field changes as a function of time. The alternating magnetic field causes an electric field in the pick-up coils according to Faraday's law of induction. This current is proportional to the magnetization of the sample. The greater the magnetization, the greater will be the induced current. The induction current is amplified by a trans-impedance and lock-in amplifier. The various components are hooked on to a computer interface. Using controlling and monitoring software, the system can tell how much the sample is magnetized and how its magnetization depends on the strength of the constant magnetic field.

Model 4500 Vibrating sample magnetometer from EG & G Princeton is used for the magnetization measurements. The VSM measurements are taken in the magnetic field range of ± 15 KOe. Before starting the actual measurement, the system is calibrated with a cylindrical nickel specimen of standard size and weight of 92.5 mg at a uniform magnetic field to give a saturation moment of about 56 emu/g. Calibration could be maintained within ± 0.05% using a vibrating sample magnetometer. The output of the VSM is the applied magnetic field versus magnetic moment in emu.

2.3.7 Thermo Gravimetric Analysis

Thermo Gravimetric Analysis (TGA) is an analytical technique used to determine a material’s thermal stability and the fraction of volatile components by monitoring the weight change that occurs as specimen is heated. The measurement is normally carried out in air or in an inert atmosphere, like helium or argon, and the weight is recorded as a function of temperature. The TGA can give information such as composition of multi-component systems, thermal stability of materials, oxidative stability of materials, estimated lifetime of a product, decomposition kinetics of materials, the effect of reactive or corrosive atmospheres on materials, moisture and the volatile content of materials. These essential components include a container in the form of a crucible to hold the sample, a furnace that can heat the sample to a high temperature, and an appropriate balance that continuously monitor the sample weight. The test material is placed in an alumina cup that is supported on an analytical balance located outside the furnace chamber.

The balance is zeroed, and the sample cup is heated according to a predetermined thermal cycle. The balance sends the weight signal to the computer for storage, along with the sample temperature and the elapsed time. The TGA curve plots the TGA signal, converted to percent weight change on the Y-axis against the reference material temperature on the X-axis.

Mettler Toledo TG/SDTA-851e is used for thermo gravimetric analysis. The TGA is used in this study not only to get the moisture but also the amount of surfactant present. Weight loss measurements are taken from 50–600 ^{0}C in inert atmosphere (argon), at a constant temperature increment of 5 ^{0}C/min. The quantity of the sample used for analysis is typically 30–40 mg.

2.3.8 Fourier Transform Infrared Spectroscopy

In infrared (IR) spectroscopy, infrared radiation is passed through a sample. A part of the infrared radiation is absorbed by the sample and some is transmitted. The resulting spectrum represents the molecular absorption and transmission, creating a molecular fingerprint of the sample. Like a fingerprint no two unique molecular structures can produce the same infrared spectrum. This makes infrared spectroscopy useful for several types of analysis. Fourier Transform Infrared (FT-IR) spectrometry was developed in order to overcome limitations like slow scanning process encounterd with dispersive instruments. A method for measuring all of the infrared frequencies simultaneously, rather than individually, is needed. A solution is, developed which employed a very simple optical device called an interferometer. The interferometer produces a unique type of signal which has all of the infrared frequencies ‘encoded’ into it. The signal can be measured very quickly, usually on the order of a second or so. Because the analyst requires a frequency spectrum (a plot of the intensity at each individual frequency) in order to make identification, the measured interferogram signal cannot be interpreted directly. A means of ‘decoding’ the individual frequencies is required. This is accomplished via a well-known mathematical technique called the Fourier transformation. This transformation is performed by the computer which then presents the user with the desired spectral information for analysis.

In normal instrumental process, infrared energy is emitted from a glowing black-body source. This beam passes through an aperture which controls the amount of energy presented to the sample. The beam enters the interferometer where the ‘spectral encoding’ takes place. The resulting interferogram signal then exits from the interferometer. The beam enters the sample compartment where it is transmitted through or reflected off the surface of the sample, depending on the type of analysis being accomplished. This is where the specific frequencies of energy, characteristic of the sample are absorbed. The beam finally passes to the detector for the final measurement. The detectors used are specially designed to measure the special interferogram signal. The measured signal is then digitized and sent to the computer where the Fourier transformation takes place. Because there needs a relative scale for the absorption intensity, a background spectrum must be measured. This is normally a measurement with no sample in the beam. This can be compared to the sample in the beam to determine the ‘percent transmittance’.

Hartmann & Braun (model AB BOMEM MB 100) FTIR spectrometer is used for IR absorption studies in the spectral range of 4000–400 cm^{-1}. The spectral resolution of the instrument is 4 cm^{-1}. Pellets made with KBr powder and ferrite nanoparticles is used for the IR studies. For characterizing oleic acid, a thin film of oleic acid is formed between ZnSe windows and the measurements are carried out from 4000–650 cm^{-1}.

2.4 Thermal Conductivity Measurements

Thermal conductivity is measured using a transient hot wire (KD2-pro). Here, the thermal conductivity of the nanofluid is measured by monitoring of heat dissipation from a line heat source. The KD2 works on the assumption that the probe is an infinitely long heat source and that the material (fluid or solid) being measured is homogeneous and isotropic and of a uniform initial temperature. For a long, electrically heating probe applied to the fluid; the rise in temperature is calculated using the equation

$$T - T_0 \cong \left[\left(\frac{q}{4\pi k} \right) \left(\ln(t) - \gamma - \ln\left(\frac{r_a{}^2}{4\alpha_T} \right) \right) \right] \tag{2.8}$$

where T is the temperature (K), T_0 is the initial temperature (K), ‘q’ is the heat produced per unit length per unit time (W m^{-1}), ‘k’ is the thermal conductivity of the medium (W m^{-1} C^{-1}), ‘t’ is the time (s), γ is Euler’s constant (0.5772), r_a is the radial distance (m), and α_T thermal diffusivity (m^2 s^{-1}). By plotting ΔT against ln(t), the thermal conductivity is simply calculated from the gradient of the slope, m, which is equal to $q/4\pi k$. A measurement cycle consists of 30s equilibration time, 30s heating time and 30s cooling time. Temperature measurements are made at 1s intervals during heating and cooling. The measurements are then fit with exponential integral functions using a nonlinear least squares procedure. A linear drift term corrects for temperature changes of the sample during the measurement, to optimize the accuracy of the readings.

The probe length of thermal conductivity meter is 60 mm and the diameter is 1.28 mm. The thermal conductivity range of the probe is 0.02–2 W m^{-1} C^{-1}. The accuracy in the k measurement is within 5%. The vial, in which the sample is taken, had a diameter of 24 mm.

Calibration of the probe is carried out by measuring the thermal conductivity of four standard liquids—water, glycerol, ethylene glycol and kerosene; the measured values are in good agreement with the literature values. To measure the thermal conductivity at different temperatures, the sample vial with the thermal conductivity probe is immersed in a circulating water bath and the temperature of the water bath is maintained within ± 0.1 ^{0}C. The entire sample assembly is insulated for temperature gradient and vibrations. The thermal conductivity measurements are made 10 minutes after achieving the desired temperature for better temperature equilibrium.

2.5 Rheological Studies

The rheological behavior of dispersions is studied using a rotational rheometer (Anton Paar Physica MCR 301) with magneto rheology attachment. The electrically commutated (EC) synchronous motor is the key component of Physica MCR rheometer. High-energy permanent magnets mounted on a small rotor disc produce a constant magnetic field, providing fast, delay-free response. The rotor moves at the same speed, i.e. synchronous with the stator field, which is produced by a series of coils. It is possible to adjust the torque in such a way that it is linear to the total amount of stator current. A change in the stator current therefore causes a simultaneous change in the torque. In contrast to induction motors, the rotor field in a synchronous motor does not change. This means there are no eddy currents causing heating problems, which significantly alter the motor characteristics and lead to signal drifts. Rapid, linear response coupled with advanced control electronics results in unmatched speed and strain control. The system has exceptional low torque capabilities down to a minimum of 10 nNm. A normal force sensor located inside the air bearing performs a capacitive measurement and detects the natural movement of the bearing due to applied normal forces. Air bearing allows position-sensitive torque mapping that reduces the residual torques to insignificant levels for measurements at the lowest torque values. Moreover, excellent normal force measurement with minimal signal drift is possible with them. A transponder chip integrated in the geometry contains all relevant geometry data, which are automatically transferred to the software. The temperature control systems are highly accurate and virtually gradient-free in horizontal and vertical directions with a liquid temperature control (–30 to +180 °C) and peltier temperature control (–40 to +200 °C) with actively heated peltier hood.

The measurements are performed with a cone and plate geometry with a cone diameter of 25 mm and a cone angle of 1°. All experiments are conducted at a constant gap of 0.5 mm and an initial stabilization period of 2 minutes is given for achieving the temperature equilibration. The liquid is placed on horizontal plate and the cone is placed into it. An electrically commutated synchronous motor drive rotates the cone at a set speed and this determines the shear rate inside the annulus of the sample. The sample tends to drag the plate, and the force it exerts on that plate (torque) is measured, which can be converted to a shear stress. Viscosity is calculated from the shear stress shear rate relation.

The Magneto-rheological measurements are performed by using Physica Rheometer MCR 301 with a Magneto-Rheological Device head (Physica MRD). A parallel-plate measuring system with a diameter of 20 mm is used at a gap of 0.5 mm. The measuring system is made of non-magnetic metal to prevent the occurrence of radial magnetic forces acting on the shaft of the measuring system. A two part cover is used as a magnetic bridge and for setting a defined air gap. There are several reasons to use parallel plates despite the fact that the shear rate is not constant in this geometry, instead of cone-plate counterparts. First, the field-induced structure in ferrofluids strongly depends on the confining geometry;[240] by changing the gap, it can be easily modified. Second, the average aggregate length is one of the major features determining the rheological response;[241] for parallel plates, gap thickness is constant in all the sample volume. Moreover, it has the advantage of much easier operation and cleaning procedures compared to a concentric cylinder system. The temperature is set to 25°C for all tests with a fluid circulator.

The magnetic field is applied perpendicular to the plates. The coil current and the magnetic field strength can be controlled using a separate control unit and the rheometer software (Physica US 200). The magnetic field strength can be applied as linear or logarithmic ramps. The software enables to set the magnetic field strength as well as to perform all rheological tests. When the test is finished the system can be automatically demagnetized by the control unit. Theoretical consideration of the magnetic field leads to the following equations. As the relative permeability of the sample μ_r is not a constant but depends on the magnetic field strength, the calculation has to be done iteratively. Magnetic flux density 'B' in Tesla is given by

$$B = 7.539 \times 10^{-4} \times Q \times \frac{I}{0.0035 - x\left(\frac{\mu_r - 1}{\mu_r}\right)} \tag{2.9}$$

Where, 'I' is the current in Ampere and 'x' denotes the gap size in meter. The Calibration Factor Q is an adjustment parameter dependent on the geometry. Here, this parameter equals one for the measuring system being used (20 mm diameter parallel plate and 0.5 mm gap). Magnetic field strength 'H' is given by

$$H = \frac{B}{\mu_0 \times \mu_r} \tag{2.10}$$

With the vacuum permeability, $\mu_0 = 1.256 \times 10^{-6}$ in Volt. second/Ampere. meter

Chapter – III

Size Controlled Synthesis of Nanoparticles and Nanofluids

Contents

Chapter III

Size Controlled Synthesis of Nanoparticles and Nanofluids

3.1 Introduction

Nanoparticles in the size range of 1–50 nm are core materials for implementing many nanotechnology initiatives.[242] The electrical, optical and magnetic properties of the nanoparticles strongly depend on their size.[243-245] For example, the color of semiconductor nanoparticle based display is strongly dependent on the size of the nanoparticles. Thus, many studies on nanoparticles have focused on size controlled synthesis of uniform spherical nanoparticles.[188, 246-248] This chapter focuses on the synthesis and characterization of magnetite Fe_3O_4, CuO and Ag nanoparticles.

3.2 Size Controlled Synthesis of Nanoparticles

3.2.1 Magnetite

Fe_3O_4 nanoparticles with different particle size are synthesized by changing the solvent polarity during chemical coprecipitation.[201-203] According to nucleation theory,[249] the equilibrium critical radius (r*) of the particles during nucleation in a supersaturated solution is directly proportional to solvent dielectric constant (ε) according to the expression

$$\frac{2V_m\gamma_e}{k_BTr^*} = \ln X + \frac{Z_+Z_-e^2}{4\pi\varepsilon_0\varepsilon k_BT(r_+ + r_-)} \qquad (3.1)$$

where, V_m is the molecular volume of the precipitated species, γ_e is the surface free energy per unit surface area, 'T' is the absolute temperature, k_B is Boltzmann constant, r_+ and r_- are radii of metal ions having charge values of Z_+ and Z_- respectively, 'e' is the elementary charge, ε is the solvent dielectric constant, ε_0 is the permittivity in vacuum. According to eq. (3.1), the critical radius is directly proportional to the solvent dielectric constant. Thus, by controlling the dielectric constant of solvent with suitable ratio of ethanol to water, it is possible to vary the critical nuclei size and hence the nanoparticle size. Accordingly, Fe_3O_4 nanoparticles having different sizes are synthesized in a mixed solvent of ethanol and water at six different ratio of 0:100; 20:80; 40:60, 50:50, 60:40 and 80:20. The particles are sterically and electrostatically stabilized by coating with oleic acid and TMAOH respectively. Table 3.1 shows the ethanol–water composition of the solvents used, corresponding size of Fe_3O_4 nanoparticles obtained and their saturation magnetization (M_S) values.

Table 3.1: The values of solvent dielectric constant, particle size and M_S of Fe_3O_4 nanoparticles

Ethanol: Water Ratio	**Dielectric Constant (ε)**	**Particle Size (nm)**	**M_S (emu/g)**
0:100	80	9.5	57
20:80	69	8.4	42
40:60	58	6.1	25
50:50	46	4.5	28
60:40	41	3.6	15
80:20	35	2.6	8

The XRD pattern (Fig. 3.1) of Fe_3O_4 nanoparticles synthesized at different ethanol-water ratio (0:100, 20:80, 40:60, 50:50, 60:40 and 80:20) show diffraction peaks corresponding to Bragg reflections from (220), (311), (400), (422), (511) and (440) crystal planes, which can be indexed to the cubic spinel structure with the Fe_3O_4 phase. These characteristic peaks are well matched with the standard JCPDS card no. 19-0629.

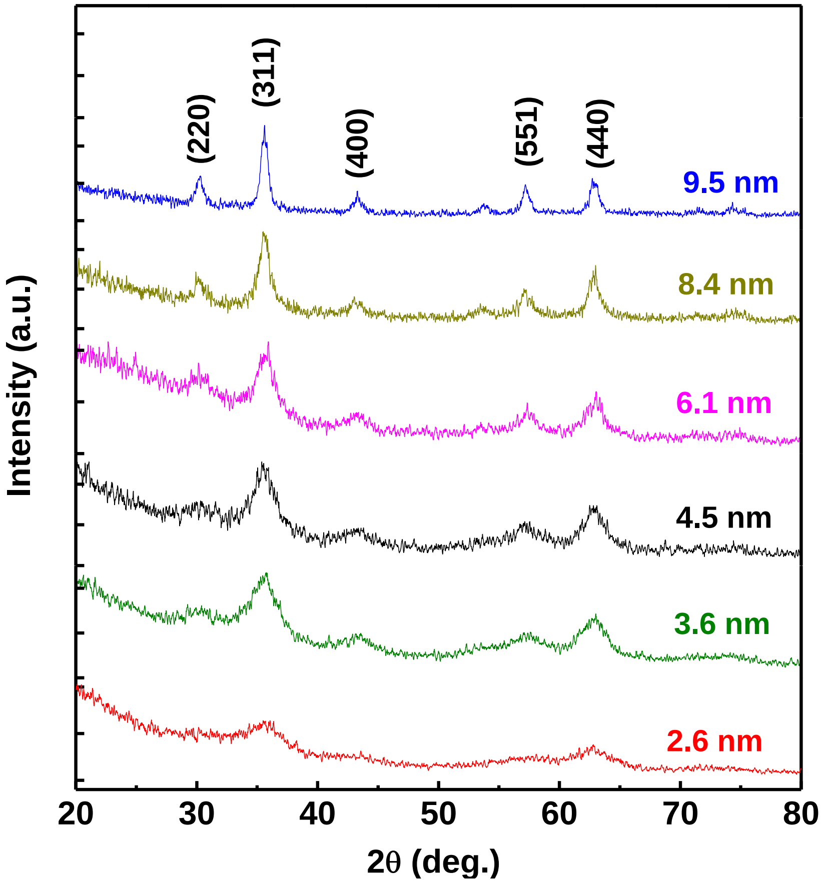

Fig. 3.1: The XRD pattern of Fe_3O_4 nanoparticles obtained with different solvent dielectric constants (ε = 35, 41, 46, 58, 69 & 80).

The XRD patterns show broadening of peaks with increase in ethanol concentration. The average crystallite size (d) is obtained from the most intense peak, corresponding to (311) reflection using the Debye-Scherrer formula. The particle size increase from 2.6 to 9.5 nm, as the solvent dielectric constant is varied from 35 to 80. Figure 3.2 shows a linear relationship between 'd' and ε, in good agreement with the nucleation theory. The lattice constants for ε values of 35, 41, 46, 58, 69 and 80 are 0.833, 0.833, 0.835, 0.838, 0839 and 0.839 nm respectively. The decrease in lattice constant at low particle size (low ε) is due to very high surface energy of particles. Figure 3.3 shows the hydrodynamic size (d_{hy}) distribution measured using DLS for Fe_3O_4 nanoparticles synthesized at different solvent dielectric constants. A single peak with narrow size distribution is observed in all the cases. Moreover, the average particle size measured by DLS matches with the average crystallite size obtained from the XRD results indicating the absence of aggregation of primary nanoparticles in suspensions due to proper surfactant capping.

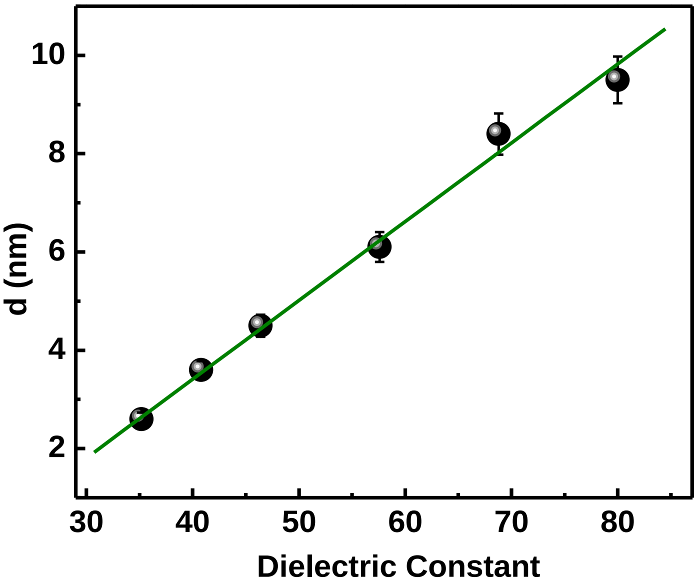

Fig. 3.2: The variation of crystallite size of Fe_3O_4 nanoparticles with ε. The best fit is shown by the solid line.

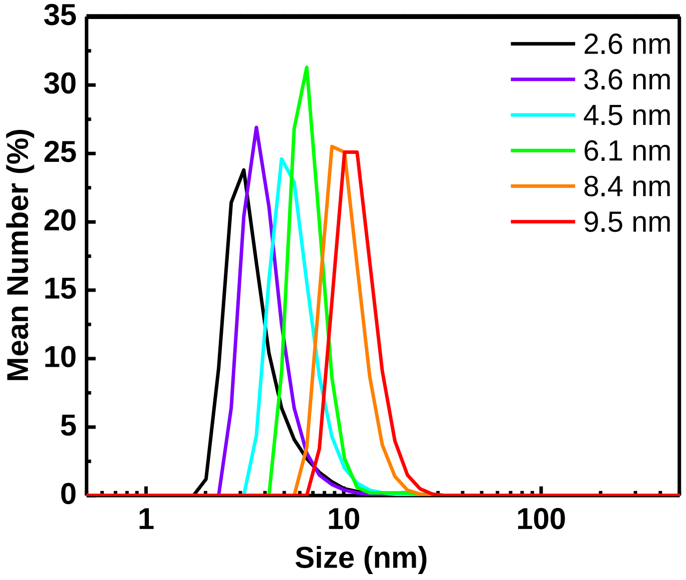

Fig. 3.3: The hydrodynamic particle size distribution of Fe_3O_4 nanoparticles synthesized with different solvent dielectric constants (ε = 35, 41, 46, 58, 69 & 80).

Figure 3.4 shows the room-temperature magnetization of Fe_3O_4 nanoparticles as a function of the applied magnetic field. The M-H loops confirm the superparamagnetic behavior with zero coercivity and remanence for Fe_3O_4 nanoparticles in the size range of 2.6 to 9.5 nm. The M_S of the Fe_3O_4 nanoparticles decreases with the decrease in nanoparticle size. The obtained values of M_S are 8, 15, 21, 28, 42 and 57 emu/g (after correcting the surfactant contribution) for Fe_3O_4 nanoparticles synthesized at solvent dielectric constant of 35, 41, 46, 58, 69 and 80 respectively. These values are comparable with the reported values of M_S, which ranges from 62 to 17 emu/g for oleic acid/oleylamine coated Fe_3O_4 nanoparticle in the size range of 12 to 4 nm[250] and pyrrolidone coated Fe_3O_4 nanoparticle in the size range of 11 to 5 nm.[251] The reported value of magnetite bulk M_S is 92 emu/g.[252] The observed decrease in M_S with particle size is attributed to the contributions originating from the magnetically disordered shell.

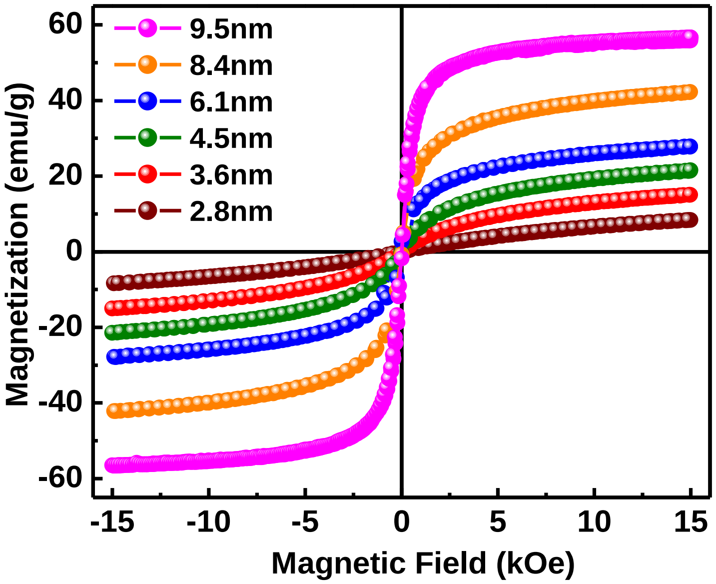

Fig. 3.4: The magnetization curve of Fe_3O_4 nanoparticles synthesized with different solvent dielectric constants (ε = 35, 41, 46, 58, 69 & 80).

The surface of nanostructured magnetic material known to exhibit lower magnetic properties compared to the bulk due to the lack of structural periodicity that leads to the formation of noncollinear spin configuration at the surface. With the decrease in nanoparticle size, the reduced coordination and hence broken superexchange bonds between surface spins result in an alteration of the orientation of each magnetic moment and consequently to a disordered spin configuration and a reduction of the average net moment.[253, 254] Assuming a core-shell structure, with a shell of thickness 'h' that does not contribute to M_S, the variation of M_S with particle size 'd' is given by Tang et al. and Berkowitz et al[255, 256] as

$$M_s = M_{Bulk}(1-6h/d) \qquad (3.2)$$

where M_{Bulk} is the bulk magnetization value. Figure 3.5 shows the variation of M_S with reciprocal of average particle size of Fe_3O_4 nanoparticles and the best fit on the experimental data. The best linear fit gives a 'h' value of 4.45 Å and M_S value of 64 emu/g, which corresponds to 70% of the bulk M_S value of 92 emu/g. The obtained value of 'h' is comparable with the reported value of 6.8 Å (at 300 K) for oleic acid/oleylamine coated Fe_3O_4 nanoparticle in the size range of 4 to 12 nm.[250]

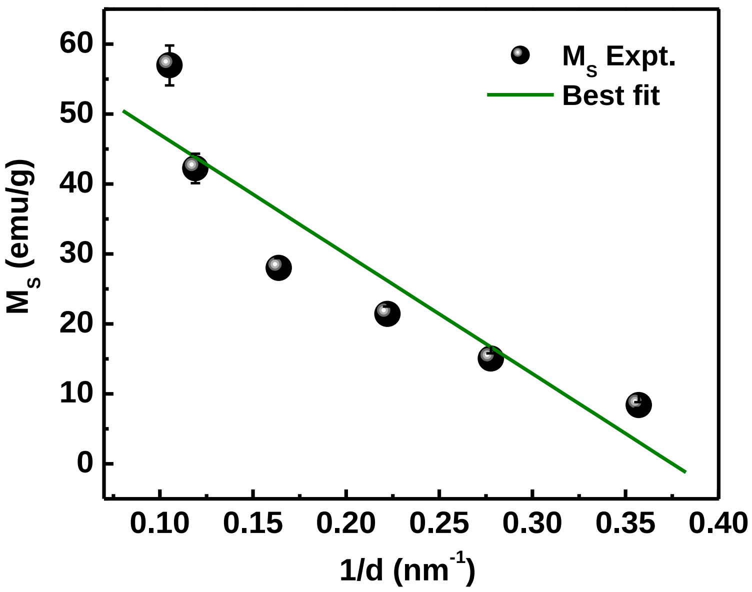

Fig. 3.5: The variation of saturation magnetization (solid circle) with reciprocal of size. Solid line shows the best fit [M_S = 64 x (1-(6x4.45/d))].

The amount of surfactant present on Fe_3O_4 nanoparticle is examined by TGA. The oleic acid coated Fe_3O_4 nanoparticles show a two-step weight loss as shown in Fig. 3.6. Initial broad weight loss observed in the temperature range 100–300 ^{0}C corresponds to the removal of moisture present in the sample. The second weight loss occurs at the boiling point of oleic acid, which is in the range of 350–400 ^{0}C. A total weight loss of 32 and 13% is observed for 2.6 and 9.5 nm sized oleic acid coated Fe_3O_4 nanoparticles respectively. A similar two step weight loss is reported for oleic acid coated magnetite nanoparticles in the size range of 6-8 nm[257]. Oleic acid coated cobalt (Co) and nickel (Ni) nanoparticles also showed a similar weight loss trend in TGA studies.[258]

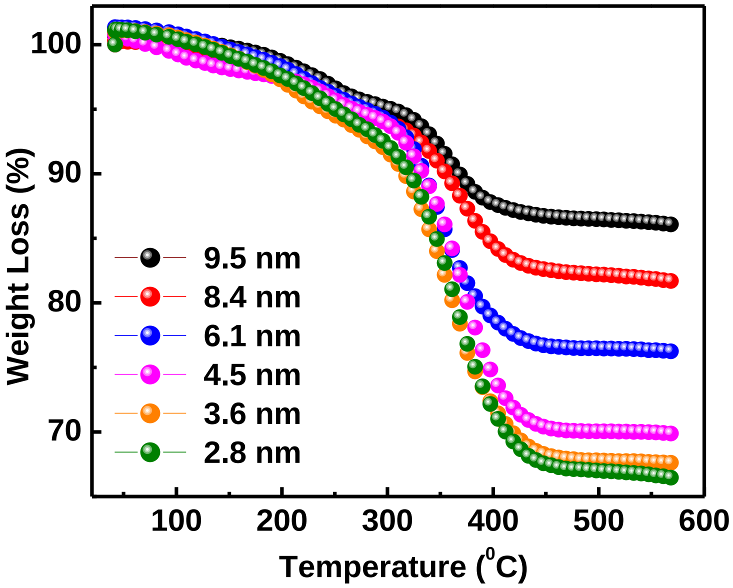

Fig. 3.6: The weight loss as a function of temperature for Fe_3O_4 nanoparticles synthesized with different solvent dielectric constants.

The binding of oleic acid on Fe_3O_4 nanoparticle surface is examined by FTIR spectroscopy. Figure 3.7 shows the FTIR spectrum of pure oleic acid, uncoated Fe_3O_4 nanoparticles and oleic acid coated Fe_3O_4 nanoparticles. For pure oleic acid [Fig. 3.7 (a)], broad features between 3500 and 2500 cm^{-1} is undoubtedly due to the O–H stretch of the carboxylic acid. No other functional group has such a broad and intense band at high wavenumber. Two sharp bands at 2926 and 2854 cm^{-1}, which are superimposed on the O–H stretch, are attributed to the asymmetric CH_2 stretch and the symmetric CH_2 stretch, respectively.[259] The intense peak at 1710 cm^{-1} is from the existence of the C=O stretch and the band at 1286 cm^{-1} shows the presence of the C–O stretch.[260] The O–H in-plane and out-of-plane bands are appeared at 1462 and 937 cm^{-1}, respectively.[261] Uncoated [Fig. 3.7 (b)] and oleic acid coated [Fig. 3.7 (c)] Fe_3O_4 nanoparticles show the peak of 578 cm^{-1}, corresponding to stretching vibration mode of Fe–O bonds and a peak at 636 cm^{-1} confirms that iron (Fe) is located at two environments i.e., octahedral and tetrahedral sites of spinel ferrite.[262]

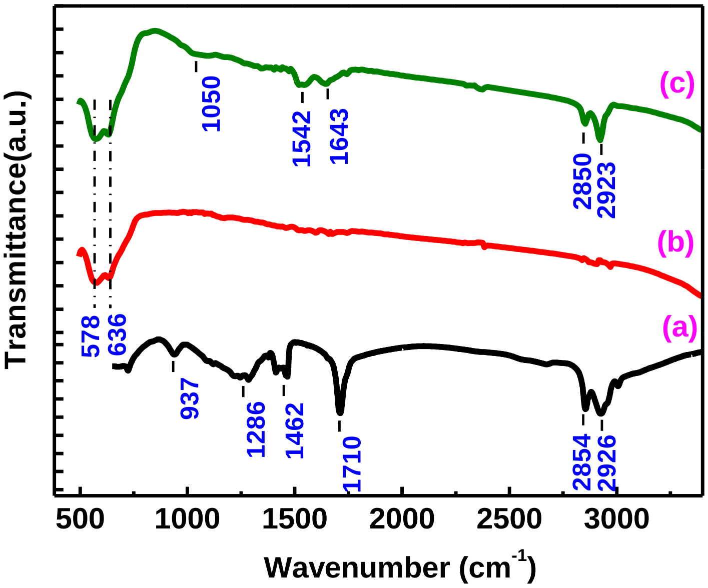

Fig. 3.7: The FTIR spectra of (a) oleic acid (b) uncoated Fe_3O_4 nanoparticles and (c) oleic acid coated Fe_3O_4 nanoparticles.

Figure 3.7 (c) shows the IR spectrum of Fe_3O_4 nanoparticles coated with oleic acid. With the adsorbed surfactant, the asymmetric CH_2 and the symmetric CH_2 peaks are shifted to 2923 and 2850 cm^{-1} respectively. The surfactant molecules in the adsorbed state are subject to the field of the solid surface. As a result, the characteristic bands shifted to a lower frequency region and indicate that the hydrocarbon chains in the monolayer surrounding of the Fe_3O_4 nanoparticles are in a close-packed crystalline state.[263, 264] The C=O stretch band of the carboxyl group, which is present at 1710 cm^{-1} in the IR spectrum of pure liquid oleic acid, is absent in the spectrum of the coated Fe_3O_4 nanoparticles. Instead, two new bands at 1542 and 1643 cm^{-1} appears that are characteristic of the asymmetric $\upsilon_{as}(COO^{-})$ and the symmetric $\upsilon_{s}(COO^{-})$ stretch. A strong adsorption at 1050 cm^{-1} arises from C–O single bond stretching. This reveals that oleic acid is chemisorbed as a carboxylate group onto the Fe_3O_4 nanoparticles, and the two oxygen atoms in the carboxylate are coordinated symmetrically to the Fe_3O_4 atoms.[264, 265]

Figure 3.8 shows the schematic representation of binding of oleic acid on Fe_3O_4 nanoparticle surface. During coprecipitation, after the addition of the precipitating agent (ammonia), the Fe_3O_4 nanoparticles will have surface bound OH^{-} ions. The oleic acid forms water soluble ammonium oleate salt in the presence of ammonia. The negative charge at the oleate anion delocalizes between the two oxygen atoms because of the resonance effect. In the coating process, the oleate anions replace the magnetite surface bound OH^{-} ions by ion exchange adsorption. The two oxygen atoms in the chemisorbed oleate ion are coordinated symmetrically to the Fe atoms. The XPS studies substantiate the formation of Fe–O chemical bonds between the iron oxide substrate and the oxygen atoms of the carboxylic acid.[261, 266]

To prepare stable water based ferrofluid, particles are coated with TMAOH. When the particles are coated with TMAOH, surface of the particles is charged with hydroxide ions and the tetramethyl ammonium group acts as counter ions in the solution that creates a double layer in an aqueous environment. The net repulsion between two similarly charged particles raises the energy required for the particles to agglomerate and stabilize the nanoparticle suspensions.[267, 268]

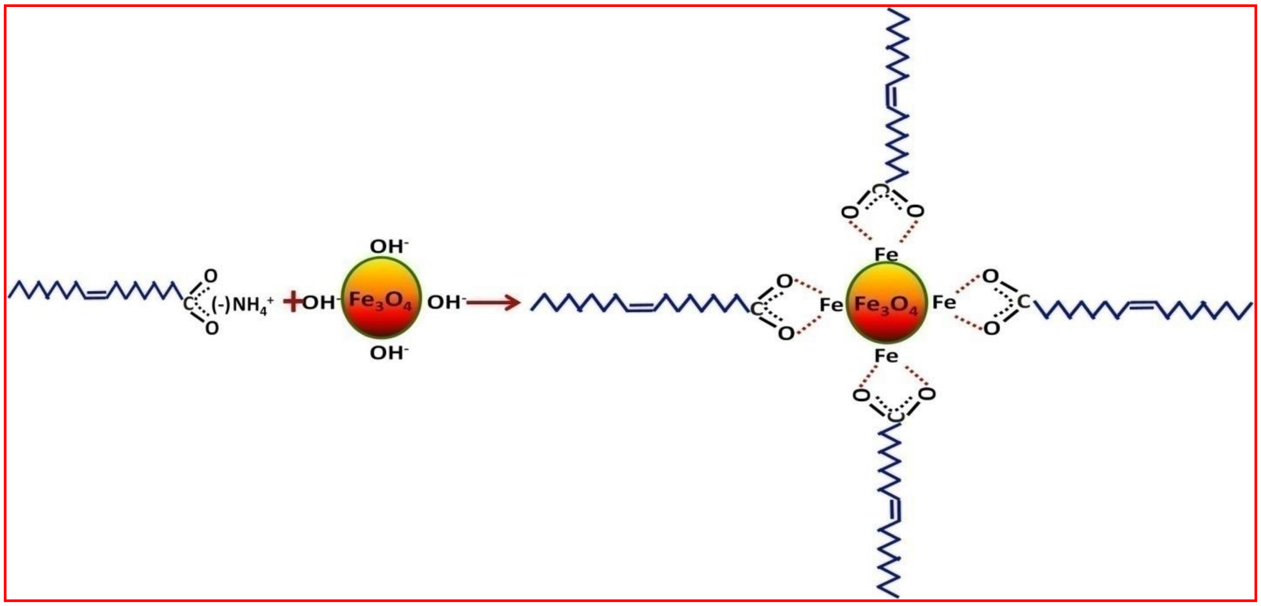

Fig. 3.8: The schematic representation of binding of oleic acid on Fe_3O_4 nanoparticle surface.

Figures 3.9 (a) and (b) shows the schematics of steric and electrostatic stabilization of Fe_3O_4 nanoparticles respectively. The carboxylic acid group of oleic acid binds to the surface of the magnetite, and the aliphatic chain extends into the nonpolar solvent, preventing aggregation of particles by steric hindrance. Tetramethyl ammonium hydroxide coats the magnetite particles with hydroxide anions, which attract tetramethyl ammonium cations, forming a diffuse shell around each particle and creating repulsion between particles.

The typical TEM image of oleic acid coated Fe_3O_4 nanoparticles is shown in Fig. 3.10 (a). The TEM micrograph shows that the size distribution is fairly narrow. The HRTEM image shows an amorphous contrast around the nanoparticles due to the presence of a hydrophobic organic layer [Fig. 3.10 (b)]. Analysis of the image shows that the thickness of the surfactant coating is about 1.5 nm.

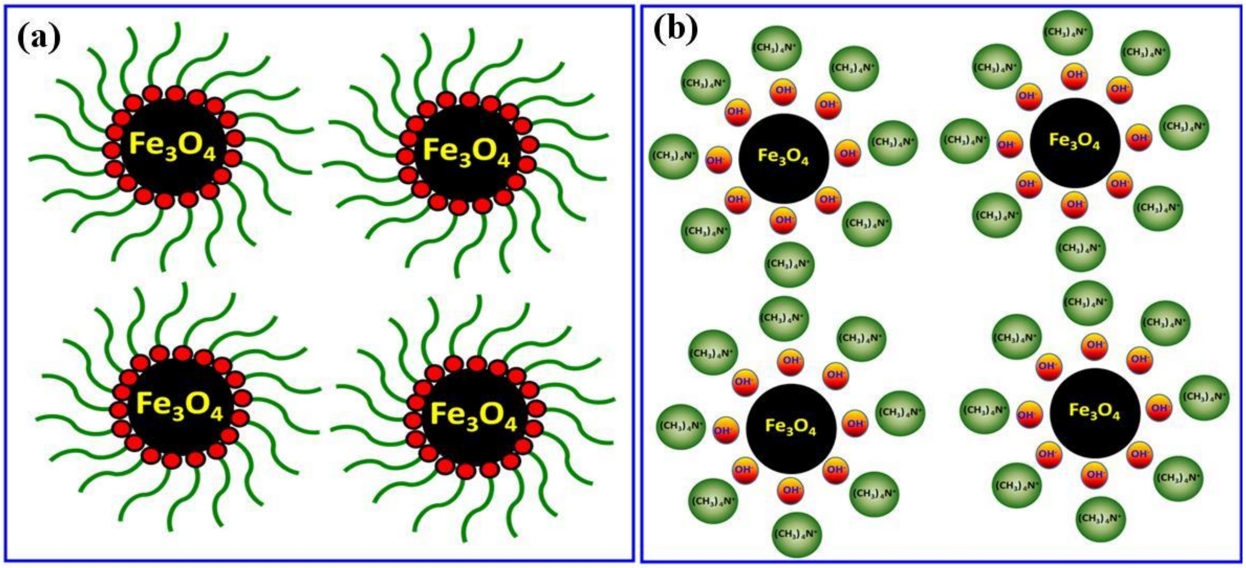

Fig. 3.9: The schematic representation of (a) steric and (b) electrostatic stabilization of Fe_3O_4 nanoparticles by oleic acid and TMAOH coating respectively.

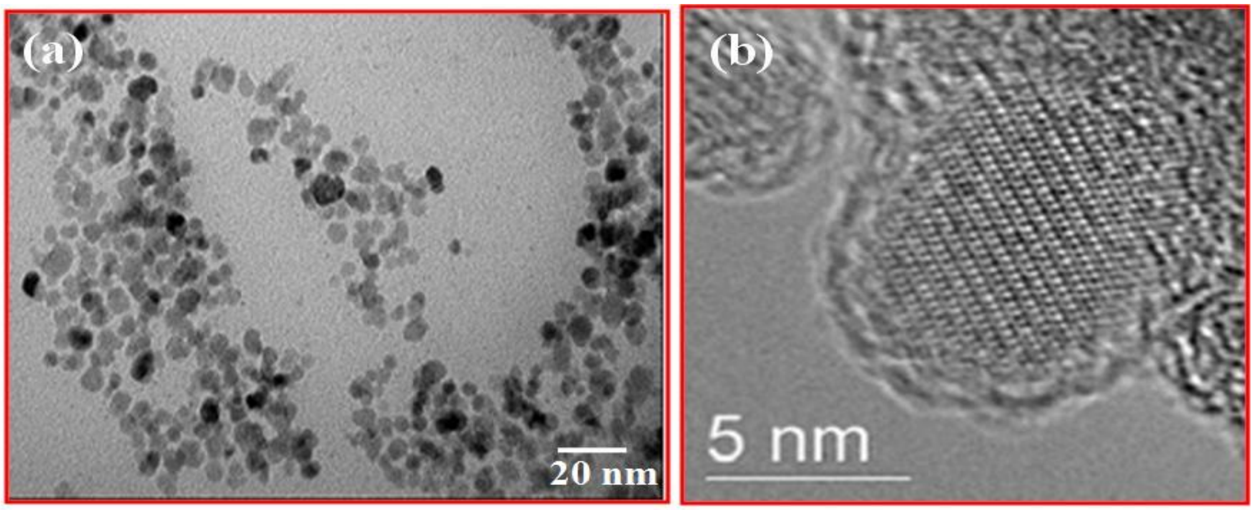

Fig. 3.10: (a): TEM and (b): HRTEM image of oleic acid coated Fe_3O_4 nanoparticles.

3.2.2 Copper Oxide

Using the knowledge of varying the critical nuclei size and hence the particle size by changing the dielectric constant of solvent, CuO nanoparticles having different sizes are synthesized in a mixed solvent of ethanol and water at six different ratio of 0:100; 20:80; 40:60 and 50:50. No surfactant is employed here. Table 3.2 shows the ethanol–water composition of the solvents used and the corresponding size of CuO nanoparticles obtained. The XRD pattern (Fig. 3.11) of CuO nanoparticles synthesized at different ethanol-water ratio (0:100, 20:80, 40:60 and 50:50) show diffraction peaks corresponding to Bragg reflections from (110), (002), (111), $(\bar{2}02)$, (020), (202), $(\bar{1}13)$, $(\bar{3}11)$, (310), (220), $(\bar{3}12)$ and (004) crystallographic planes, which can be indexed to the monoclinic CuO crystal (JCPDS card no. 45-0937). The XRD pattern does not show any impurity peaks. A broadening of peaks is observed with increase in ethanol concentration. The average particle size is obtained from the most intense peak, corresponding to (111) reflection using the Debye-Scherrer formula.

Table 3.2: The values of solvent dielectric constant and the size of CuO nanoparticles

Ethanol: Water Ratio	**Dielectric Constant (ε)**	**Particle Size (nm)**
0:100	80	12.4
20:80	69	10.1
40:60	58	8.9
50:50	46	7.6

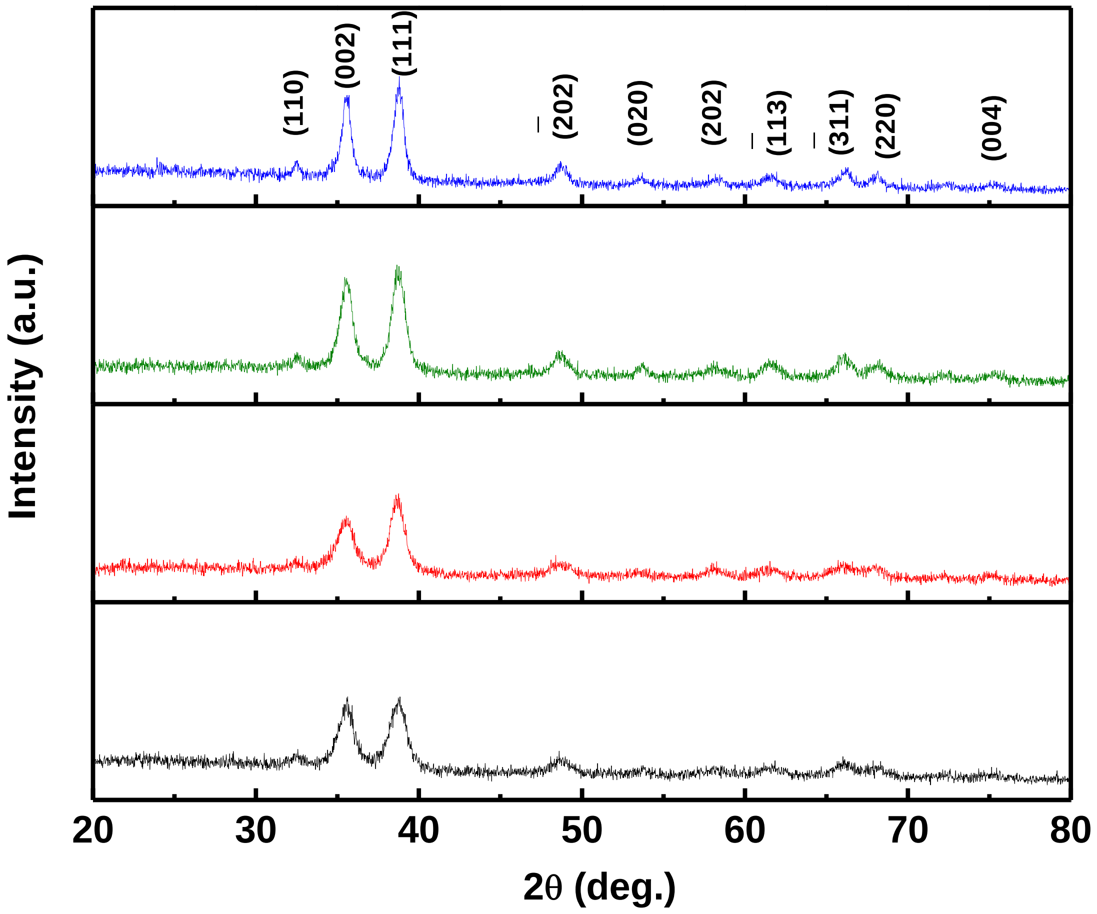

Fig. 3.11: The XRD pattern of CuO nanoparticles obtained with different solvent dielectric constants (ε = 46, 58, 69 & 80).

The particle size increase from 7.6 to 12.4 nm as the solvent dielectric constant is increased from 46 to 80 (Fig. 3.12). The typical TEM images of as prepared CuO nanoparticles at two different concentrations are shown in Fig. 3.13. From the micrograph, it is clear that the CuO nanoparticles are agglomerated, due to the absence of stabilizing moieties on nanoparticles.

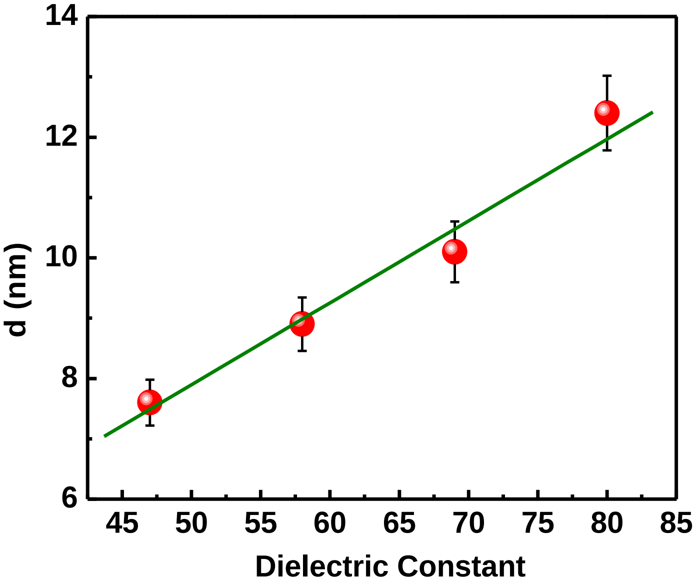

Fig. 3.12: The variation of crystallite size of CuO nanoparticles with ε. The best fit is shown by the solid line.

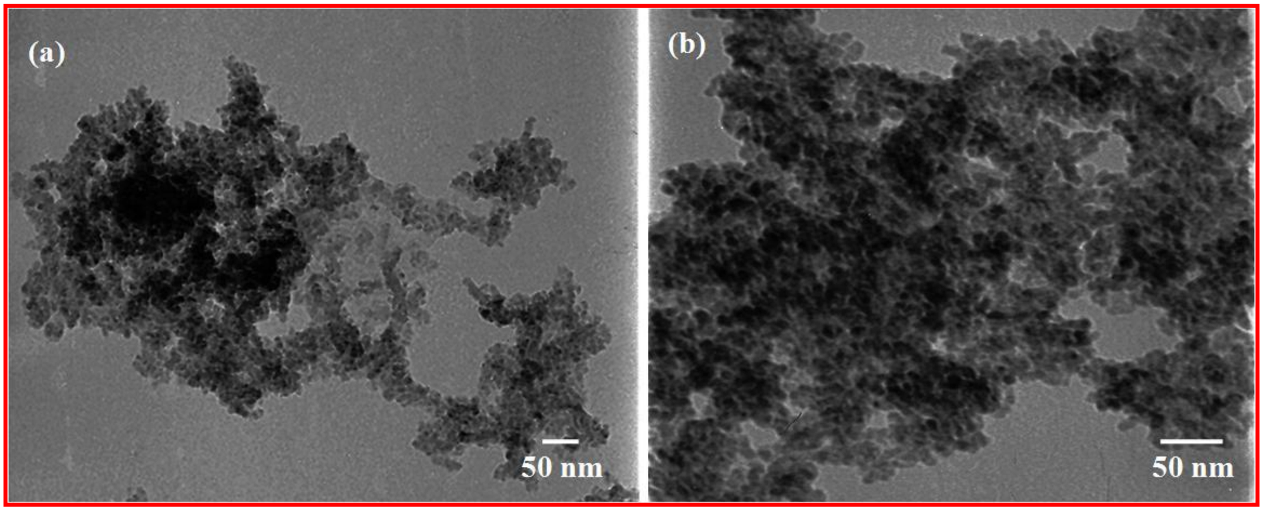

Fig. 3.13 (a) and (b): The TEM images of CuO nanoparticles at two different concentrations.

3.2.3 Silver

Oleylamine coated Ag nanoparticles are synthesized by reduction of silver salt in presence of surfactant in a mixture of polar and nonpolar solvents. The XRD pattern (Fig. 3.14) of Ag nanoparticles shows diffraction peaks corresponding to Bragg reflections from (111), (200), (220) and (311) crystallographic planes, which is indexed to face-centered cubic (FCC) of silver crystal. The absence of peaks in any other planes indicates a phase pure Ag. The lattice constant calculated from this pattern is 4.077 Å, in agreement with the reported value of 4.086 Å (JCPDS file No. 04-0783). The average particle size obtained I 7 nm from the most intense peak, corresponding to (111) reflection using the Debye-Scherrer formula.

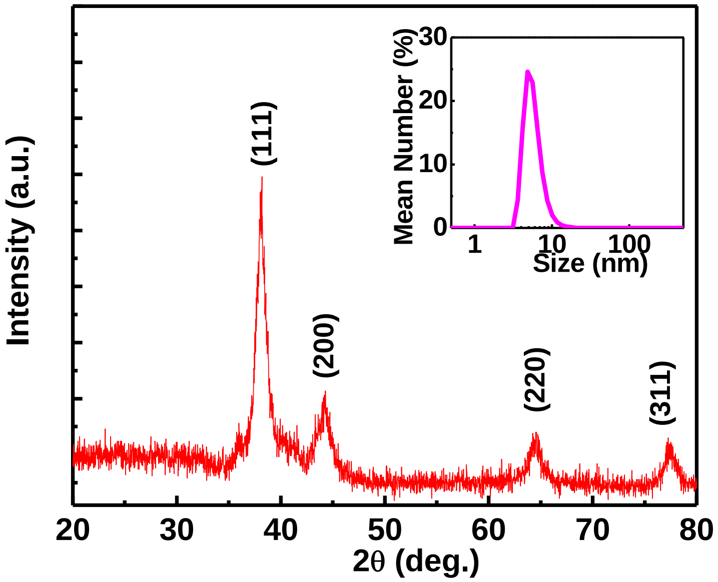

Fig. 3.14: The XRD pattern of Ag nanoparticles. Inset shows particle size distribution measured by DLS.

Fig. 3.14 inset shows the particle size distribution of Ag nanoparticles measured using DLS. Single and narrow size distribution is observed, and the average size matches with the primary nanoparticle size obtained from the XRD results. The DLS result confirms the absence of aggregation of primary Ag nanoparticles in the suspension due to steric stabilization by oleylamine.

Fig. 3.15 shows the UV–Visible absorption spectrum of hexane based oleylamine capped silver nanofluids. An intense absorption peak observed at 400 nm is attributed to the excitation of surface plasma resonance in spherical silver nanocrystals.[229, 269] The electron motion within the metal essentially creates a dipole moment represented by a positive and negative charge on the metal where electron motion directs the negative charge to one side thus, leaving a positive charge on the other. This dipole resonance represents the surface polarization of the metal, which is affected not only by the shape of the material, but also by the size, material content and the surrounding medium.[270]

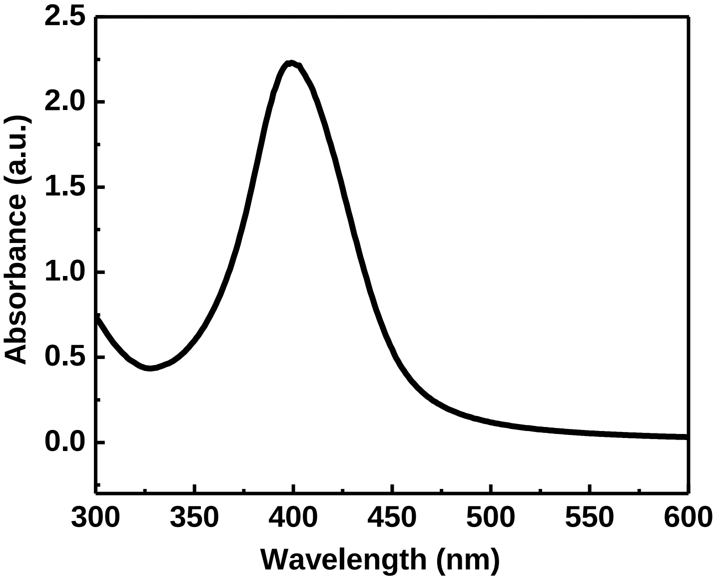

Fig. 3.15: The UV visible spectrum of Ag nanoparticles. The absorption peak at 400 nm corresponds to surface plasmon resonance.

3.3 Preparation of Nanofluids

Nanofluids for thermal and rheological study are prepared by dispersing the Fe_3O_4, CuO and Ag nanoparticles in various base fluids. Stable oil based nanofluids are prepared by dispersing the oleic acid coated Fe_3O_4 nanoparticles in kerosene and hexadecane. Stable water based nanofluids are prepared from TMAOH coated Fe_3O_4 nanoparticles. CuO nanofluid is prepared by dispersing the uncoated copper oxide in Ethylene Glycol (EG) by means of sonication. Highly stable oil based Ag nanofluids are prepared by dispersing the oleylamine coated Ag nanoparticles in hexadecane. The nanofluids with different ϕ are calculated according to the formula.

$$\phi = \frac{\omega_P \times \rho_f}{(\omega_P \times \rho_f) + \rho_p (-\omega_p)} \tag{3.3}$$

Where, ω_P is the weight fraction of particles, ρ_f and ρ_P the density of fluid and particle respectively. ρ_f are 1, 0.8, 0.77 and 1.11 g/cm^3 for water, kerosene, hexadecane and ethylene glycol. ρ_P are 5.046, 6.31 and 10.49 g/cm^3 for Fe_3O_4, CuO and Ag nanoparticles respectively.

3.4 Conclusions

Surfactant stabilized Fe_3O_4 nanoparticles with different particle size are synthesized by varying the solvent dielectric constants of the medium during coprecipitation. The XRD pattern confirms the cubic spinel structure of magnetite for nanoparticles synthesized at different solvent dielectric constants. The particle size increases with the increase in dielectric constant of the solvent in agreement with the nucleation theory. The average particle size measured by DLS matches with the primary crystallite size obtained from XRD, indicating the absence of aggregation of primary Fe_3O_4 nanoparticles due to surfactant stabilization. The magnetization data confirm the superparamagnetic behavior with zero coercivity and remanence for Fe_3O_4 nanoparticles in the size range of 2 to 9 nm. The saturation magnetization of the Fe_3O_4 nanoparticles decreases with the decreases in nanoparticle size. The TGA confirms the presence of surfactant monolayer on nanoparticle surface and the FTIR studies show the formation of Fe–O chemical bonds between the iron oxide substrate and the oxygen atoms of the carboxylic acid. The HRTEM image shows that the surfactant layer thickness is about 1.5 nm.

Uncoated CuO nanoparticles of different particle sizes are synthesized by varying solvent dielectric constant of the medium. The particle size increases with increase in dielectric constant of the solvent in agreement with the nucleation theory. The XRD pattern confirms the monoclinic copper oxide crystal structure for CuO nanoparticles synthesized at different solvent dielectric constants. Since the nanoparticles are not surface functionalized, the average particle size measured using DLS is greater than the crystallite size obtained from XRD results because of aggregation of primary particles in the suspension.

Oleylamine coated Ag nanoparticle are synthesized by the reduction of silver salt in presence of surfactant in a mixture of polar and nonpolar solvents. The XRD pattern confirms face centered cubic silver crystal. The average particle size measured by DLS matches with the primary nanoparticle size obtained from the XRD results, indicating the absence of aggregation of primary nanoparticles in suspensions due to oleylamine coating. The UV-Visible Spectroscopy results show an intense plasmon resonance absorption at 400 nm due to the excitation of surface plasmon resonance of spherical silver nanocrystals.

Nanofluids with different particle loading are prepared by dispersing the Fe_3O_4, CuO and Ag nanoparticles in different base fluids.

Chapter – IV

Effect of Nanoparticle Aggregation on Thermal and Rheological Properties of Nanofluids

Contents

Chapter IV Effect of Nanoparticle Aggregation on Thermal and Rheological Properties of Nanofluids

4.1 Introduction

Preparation of stable nanofluids is the key issue of nanofluid research and application.[271] Nanoparticles can exist in several configurations ranging from a well-dispersed mode to totally agglomerated state. The stability of nanofluids can be classified into three categories: (i) Kinetic stability: Nanoparticles dispersed in the nanofluids are under Brownian motion which can overcome their sedimentation caused by gravitational force; (ii) Dispersion stability: Due to the aggregation of nanoparticles, the dispersion of nanoparticles in fluids may deteriorate with time; and (iii) Chemical stability: No chemical reactions between the suspended nanoparticles or between the base fluid and nanoparticles are desired in nanofluids. Therefore, nanofluids are to be carefully prepared to ensure their long term stability.

In stationary state, the sedimentation velocity of small spherical particles in a liquid follows the Stokes law[272]

$$V = \frac{2d^2}{9\eta}\left(\rho_P - \rho_f\right)g \tag{4.1}$$

where 'V' is the sedimentation velocity of particles, 'd' is the size of particles, η is the viscosity of the liquid medium, 'g' is the gravitational acceleration, ρ_P and ρ_f are the density of the particles and the liquid medium respectively. This equation reflects a balance of the gravity, buoyant force and frictional force that are acting on the suspended nanoparticles. According to Eq. (4.1), to reduce the sedimentation velocity of nanoparticles and to produce stable nanofluids, one should reduce the size of nanoparticle and increase the base fluid viscosity or minimize the density difference between the nanoparticles and the base fluid. Among the above, reducing the particle size should remarkably decrease the sedimentation velocity of the nanoparticles and improve the stability of nanofluids. However, the smaller nanoparticles have higher surface energy, thereby increases the possibility of aggregation of nanoparticles. Therefore, the key to prepare stable nanofluids is to use smaller nanoparticles and to prevent the aggregation of the small nanoparticles by proper surface stabilization.

In majority of nanofluid studies, nanoparticles are produced from dry powder and then dispersing in base fluids with the help of added dispersants or by pH adjustment of the base fluid.[273] The dispersion is usually prepared under mechanical stirring, ultrasonic bath, ultrasonic disruptor or high-pressure homogenizer with the help of added dispersants or by pH adjustment of the base fluid. The effect of ultrasonication and mechanical stirring is to break down the aggregates of the nanoparticles. The dispersant addition and pH adjustment is to prevent the reaggregation of nanoparticles thereby producing stable nanofluids. Among the different dispersion techniques, ultrasonication is a simple and well accepted technique for the production of well dispersed nanofluids.[102, 103, 114, 274]

DLS, rheology and microscopy studies are often used to probe the stability and aggregation effects in nanofluids. There are many studies on aggregation in nanofluids using DLS.[58, 62, 63, 128, 136, 148, 152, 275] Viscosity (η) measurements are also used to probe the aggregation kinetics in nanofluids. The mean number of nanoparticles within the aggregates depends on the hydrodynamic interactions and there will be an enhancement of viscosity with increasing volume concentration of particles or aggregates.[147, 150, 152, 155-159] Microscopy is another powerful tool to examine the aggregation in nanofluid. Some of the previous reports show direct evidence for nanofluid aggregation using microscopy studies.[138, 152, 155, 157]

Improved dispersion stability with least enhancement in η is inevitable for the practical applications of nanofluids. However, in most experimentally tested nanofluids, there is a competition between the growth of fractal-like structures, coalescence into large clumps, sedimentation and fragmentation. To have a better understanding on k enhancements, one should use model nanofluids with long term stability. Towards this goal, both stable and aggregating nanofluids with particle size less than 10 nm are synthesized for the present study and k is measured as function of ϕ. Even if there are many studies on effect of aggregation on k of nanofluids, a systematic k study together with rheology, DLS and microscopy is still lacking, which is yet another objective of the present study. We follow the time dependant k, average particle size, microstructure and η of a stable and aggregating nanofluid after sonication.

4.2 Effect of Volume Fraction on Thermal Conductivity of Stable and Aggregating Nanofluids

In the present study, k is measured as a function of ϕ for both stable and unstable nanofluids. Stable oil based nanofluids are prepared by dispersing oleic acid coated Fe_3O_4 nanoparticles in kerosene and hexadecane. These nanofluids are perfectly stable with no aggregation due to steric stabilization offered by oleic acid. The DLS, rheology and microscopy studies confirm the absence of aggregation in the above nanofluids. The particle size measured by DLS matches with the primary crystallite size obtained from XRD results indicates the absence of aggregation of nanoparticles in suspensions. Moreover, rheology studies in these nanofluids show a

Newtonian behavior and the microscopy images show no aggregates (with size > 200 nm). Figure 4.1(a) shows the variation of k/k_f (k_f being the base fluid thermal conductivity) and the percentage of k enhancement as a function of ϕ for kerosene based Fe_3O_4 nanofluids together with Maxwell's lower fit. Only moderate k enhancement within the predictions of EMT is observed here. The maximum k enhancement observed is 23% for nanofluid with $\phi=0.078$. The data fitted with Maxwell model show good agreement especially at higher volume fractions. The enhancement above $\phi=0.0176$ could be due to small clusters (dimmers or trimmers) formed in the nanofluid due to magnetic dipolar attractions. It appears that the wetting of nanoparticles is enhanced due to the organic sheath, which in turn leads to a lower interfacial thermal resistance. We find that nanofluids with very small particles (~ 5 nm) are also prone to settling when particles are uncoated. The stable hexadecane based Fe_3O_4 nanofluids also exhibit similar k variations within the predications of EMT. Moderate k enhancement within the predications of EMT is observed for TMAOH coated stable water based Fe_3O_4 nanofluids [Fig. 4.1 (b)]. The maximum k enhancement observed is 9% for nanofluid with $\phi=0.038$. The electrostatic stabilization offered by TMAOH render long term stability against aggregation to water based nanofluids. The moderate k enhancement within the predictions of EMT observed for stable nanofluids in the present study is in agreement with the recent reports.[60-62, 69]

For a nanofluid containing non-interacting spherical nanoparticles, the EMT[37] predicts $\frac{k}{k_f}=\frac{1+2\beta\phi}{1-\beta\phi}$ where ϕ is the nanofluid volume fraction; k and k_f are the thermal conductivities of the nanofluid and the base fluid respectively. β is given by $(k_p-k_f)/(k_p+2k_f)$, where k_p is the thermal conductivity of nanoparticle. When a finite temperature discontinuity exists at the nanoparticle-fluid interface, $k_f \rightarrow k_f + \alpha k_p$, where $\alpha = 2R_b k_f / d$, R_b is the interfacial thermal resistance and 'd' is the nanoparticle size.

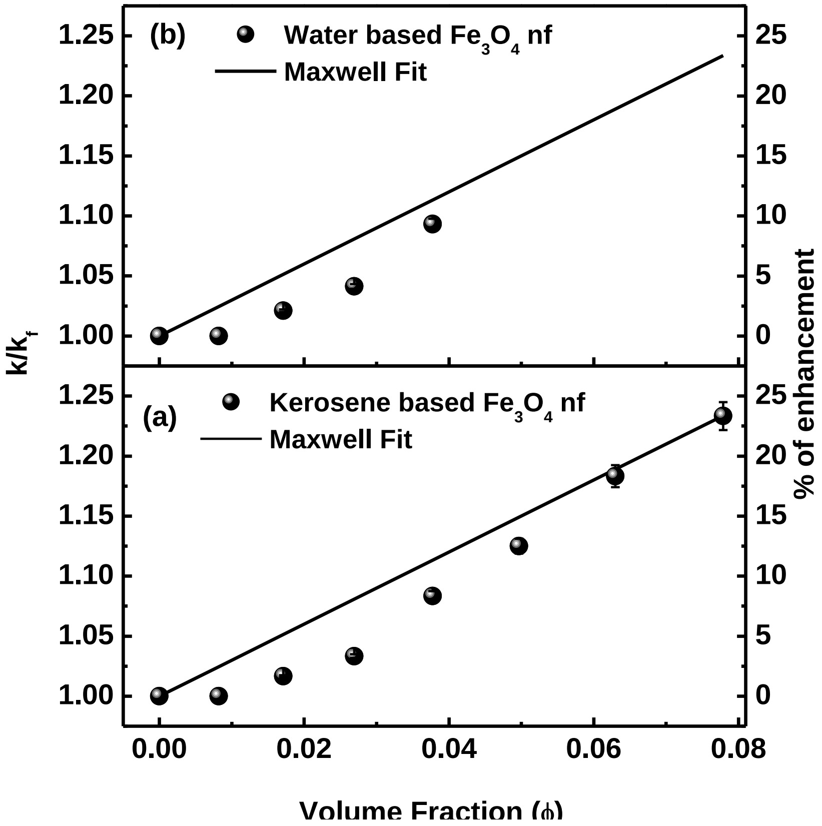

Fig. 4.1: The variation of k/k_f and the percentage (%) of k enhancement as a function of ϕ (a): For kerosene based and (b): For water based Fe_3O_4 nanofluids together with Maxwell's lower fit using $k/k_f = 1 + 3\phi$.

CuO nanofluids are prepared by dispersing uncoated CuO nanoparticles in EG. The lack of surface functionalization leads to aggregation in the above nanofluids, which is evident in DLS, rheology and microscopy results. The particle size measured by DLS is much higher than the crystallite size obtained from XRD results that confirm the aggregation of nanoparticles in suspensions. Moreover, rheology studies show a shear thinning behavior with enhanced zero shear η values and the microscopy images confirm the presence aggregates in the above nanofluids. Figure 4.2 shows the variation of k/k_f and % of k enhancement as a function of ϕ for EG based CuO nanofluids together with Maxwell's lower fit. Here, the enhancement in k/k_f is much above the EMT predictions. Maximum k enhancement observed is 13% for a nanofluid with ϕ=0.0131.Water based aggregating CuO nanofluids also shows k enhancement beyond EMT predictions. Similar enhancement in k is reported in aggregating nanofluids.[59, 61, 138, 276]

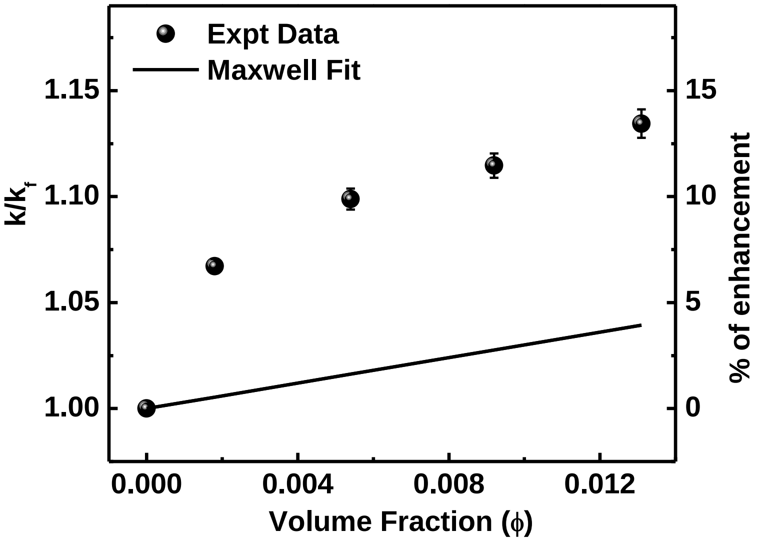

Fig. 4.2: The variation of k/k_f and % of k enhancement as a function of ϕ for EG based CuO nanofluids together with Maxwell's lower fit using $k/k_f=1+3\phi$.

The present results unambiguously confirm the prominent role of agglomeration on thermal properties of nanofluids and the importance of surface functionalization of nanoparticles for improved stability.

4.3 Effect of Aggregation on Thermal and Rheological Properties of Nanofluids

Ultrasonication is often used to improve the dispersion stability of nanofluids.[39, 102, 103, 114, 121-124, 128, 138, 277, 278] The cluster size of EG based iron (Fe) nanofluids are found to decrease with the increase in ultrasonication duration.[39, 128] In a recent study, it is shown that the size of agglomerated particles and number of primary particles in a cluster is significantly decreased with elapsed ultrasonication time in alumina and copper oxide nanofluids.[124] In an ultrasonic system, the tip of a horn is driven at ultrasonic frequencies by piezo transducers to induce oscillations (typically 20–50 kHz). Energy is transferred into the fluid in the form of pressure waves that induce cavitations that is subsequently forced to collapse, and releases intense pressure waves into the fluid. Particles adjacent to the cavity are subjected to normal and shear forces which can cause breakage of particle if they are of sufficient intensity.[279] In the present study, the effects of ultrasonication and subsequent aggregation on thermal and rheological properties of various nanofluids are investigated together with DLS and microscopy studies.

4.3.1 Kerosene Based Magnetite Nanofluids

The nanofluids are sonicated for 30 minutes at a power of 20 W using an ultrasonicator horn and k is monitored as a function of time, ten minutes after the sonication is stopped. Figure 4.3 shows the variation in k/k_f and the k enhancement with time for kerosene based Fe_3O_4 nanofluids at three different volume fractions ϕ=0.0171, 0.050, and 0.082. It can be seen that the kc values are time independent, though the particle number density is much high. Moreover, the observed k enhancement with ϕ is within the limits of EMT.

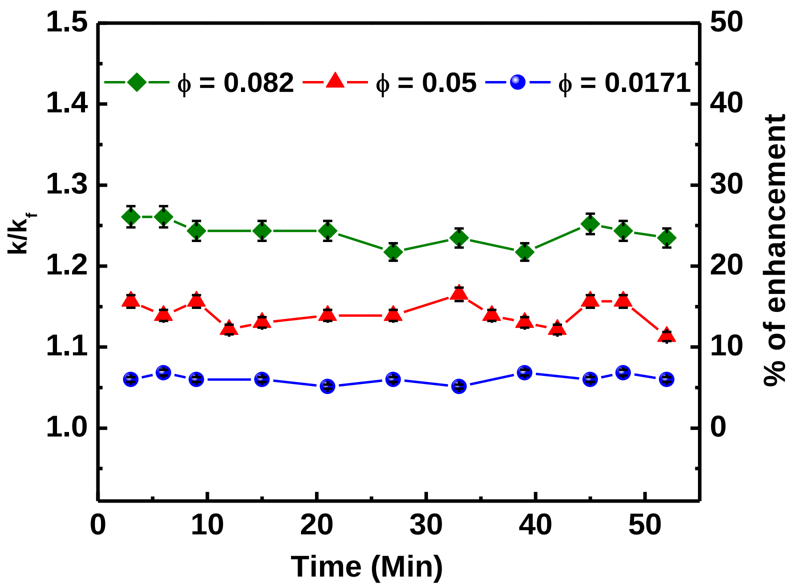

Fig. 4.3: The variation of k/k_f and % of k enhancement with time after sonication for kerosene based Fe_3O_4 nanofluids with ϕ=0.0171, 0.050 and 0.082.

DLS studies confirm the absence of aggregation in the above nanofluids due to steric stabilization of nanoparticles. Figures 4.4 (a), (b) and (c) shows the mean number percentage as a function of particles size at different time intervals after sonication of 5, 20, 40, and 60 minutes, for kerosene based Fe_3O_4 nanofluids at different particle loading of ϕ=0.082, 0.05 and 0.0171 respectively. An invariant average particle size with time is observed, which is consistent with the primary crystallite size obtained from XRD results.

Rheological studies also support the absence of aggregation in properly functionalized Fe_3O_4 nanofluids. Figure 4.5 shows the variation in η/η_0 (η_0 being the base fluid viscosity) and the η enhancement with elapsed time, after sonication, for kerosene based Fe_3O_4 nanofluids at three different volume fractions of ϕ=0.0171, 0.050, and 0.082. The viscosity ratio does not show any variation with time. Moreover, the flow curves show Newtonian behavior with less η enhancement, a characteristics of well dispersed nanofluids.

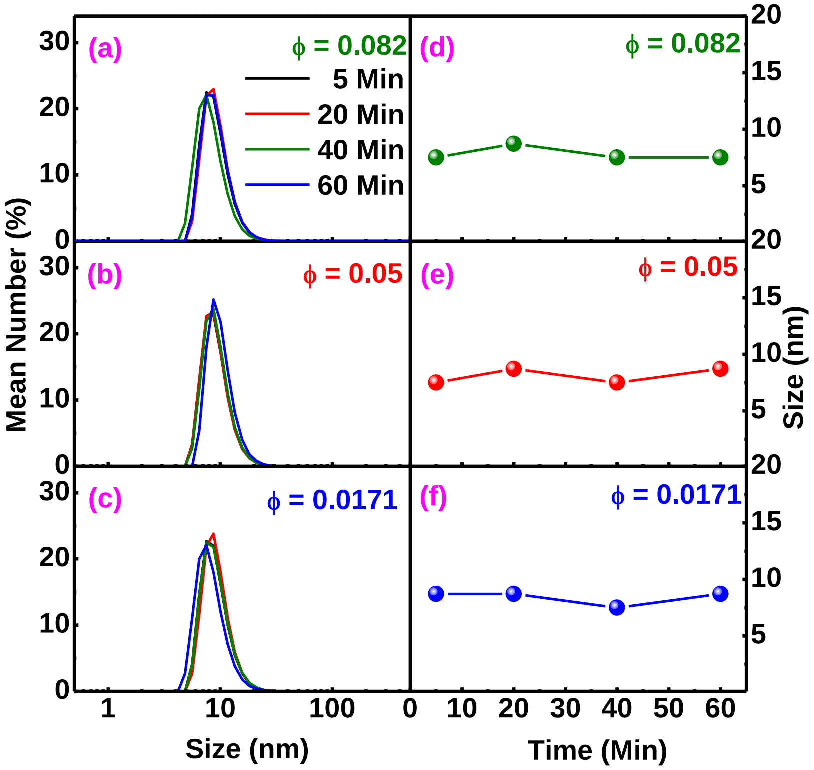

Fig. 4.4 (a), (b) and (c): The plot of mean number percentage as a function of particles size at different time intervals after sonication of 5, 20, 40, and 60 minutes for kerosene based Fe_3O_4 nanofluids with ϕ=0.082, 0.05 and 0.0171 respectively. (d), (e) and (f) shows the variation of average particle size with time for kerosene based Fe_3O_4 nanofluids with ϕ=0.082, 0.05 and 0.0171 respectively.

Finally, the stability of surface functionalized Fe_3O_4 nanofluids is confirmed by optical microscopy studies. Figures 4.6 (a–c) shows the micrograph of kerosene based Fe_3O_4 nanofluid with a particle loading of ϕ =0.050 at three different time intervals (t=5, 30, and 60 minutes) after sonication. The Fe_3O_4 nanofluid micrographs show no aggregation (with cluster size > 200 nm) with elapsed time after sonication, due to sufficient repulsion through steric hindrance.

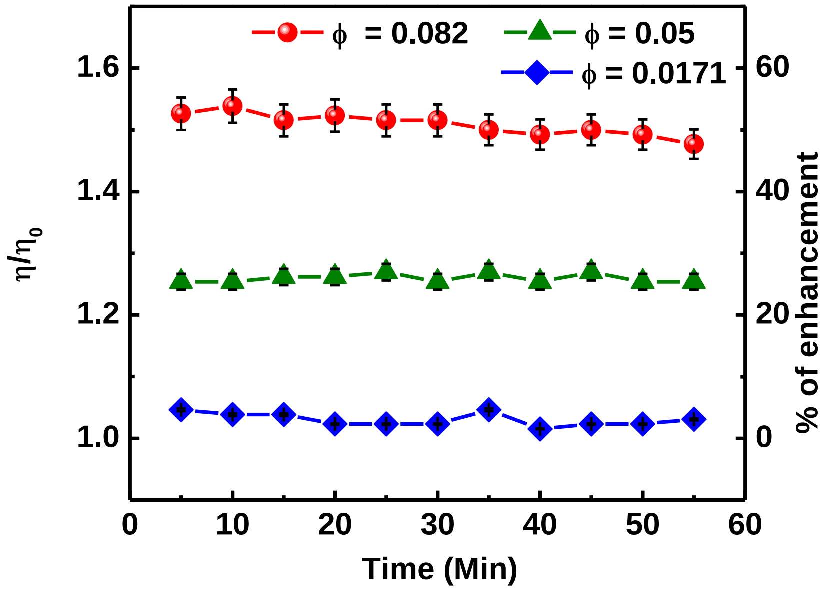

Fig. 4.5: The variation in η /η_0 and the percentage of enhancement of η with time after sonication for kerosene based Fe_3O_4 nanofluids with ϕ=0.082, 0.05 and 0.0171.

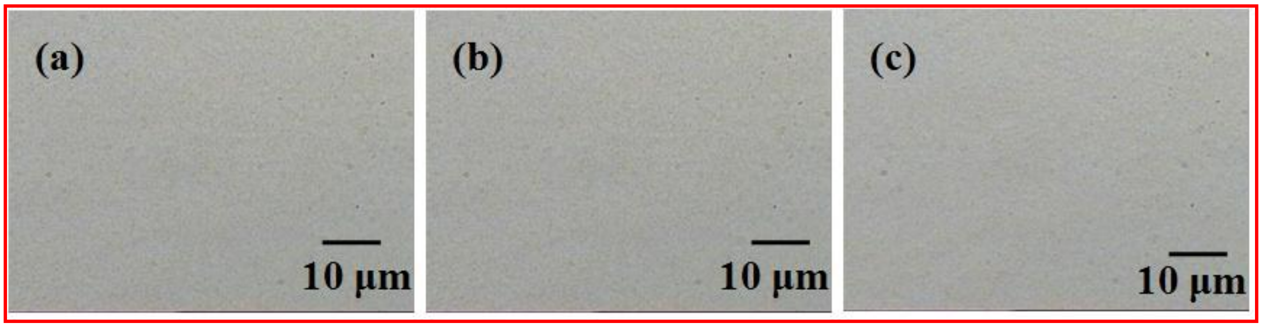

Fig. 4.6 (a), (b) and (c): The phase contrast microscopy images taken immediately after sonication, after 30 and 60 minutes of sonication for Fe_3O_4 nanofluids with ϕ=0.05

4.3.2 Hexadecane and Water Based Magnetite Nanofluids

k is measured as a function of time after sonication for stable hexadecane and water based Fe_3O_4 nanofluids.

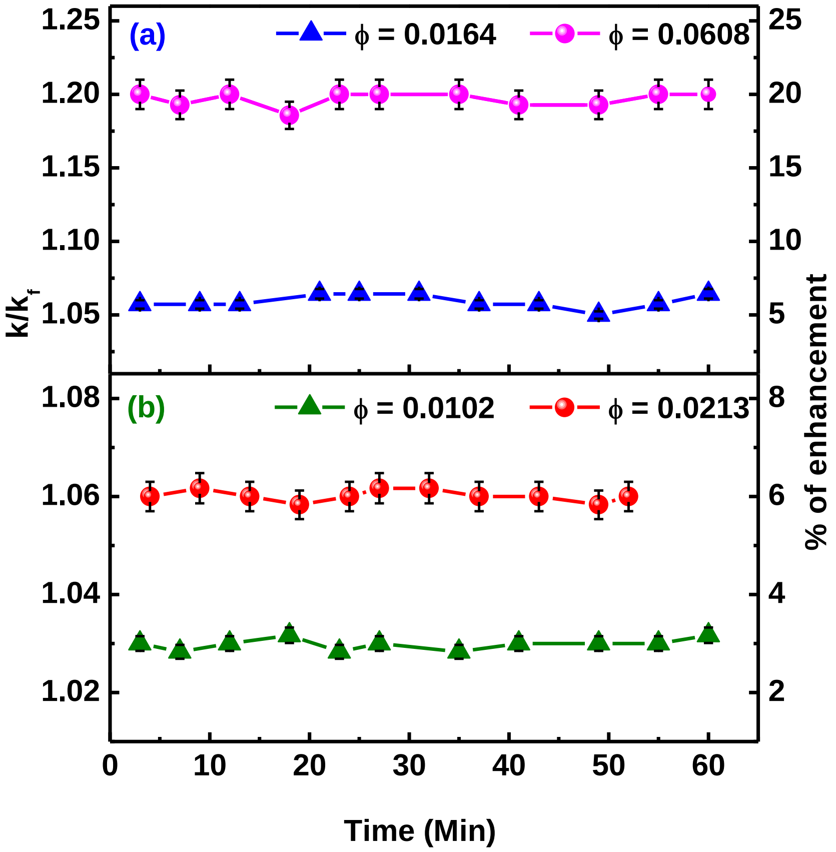

Fig. 4.7: The variation of k/k_f and % of k enhancement with time after sonication for (a): Hexadecane based Fe_3O_4 nanofluids with $\phi=0.0164$ and 0.0608. (b): Water based Fe_3O_4 nanofluids with $\phi=0.0102$ and 0.0213.

Figure 4.7 (a) shows the variation of k/k_f and % of k enhancement with time after sonication for hexadecane based Fe_3O_4 nanofluids with $\phi=0.0164$ and 0.0608. Fig. 4.7 (b) shows the variation of k/k_f and % of k enhancement with time after sonication for TMAOH coated water based

Fe_3O_4 nanofluids with ϕ=0.0102 and 0.0213. Time independent k is observed in both the cases after sonication. Oleic acid and TMAOH coating renders steric and electrostatic stabilization respectively to hexadecane and water based Fe_3O_4 nanofluids.

DLS studies confirm the absence of aggregation in the above nanofluids. Both hexadecane [Fig. 4.8 (a)] and water based [Fig. 4.8 (b)] Fe_3O_4 nanofluids show an invariant particle size distribution with time, after sonication. Moreover, the average particle size measured using DLS matches with the primary crystallite size obtained from XRD results in both the cases.

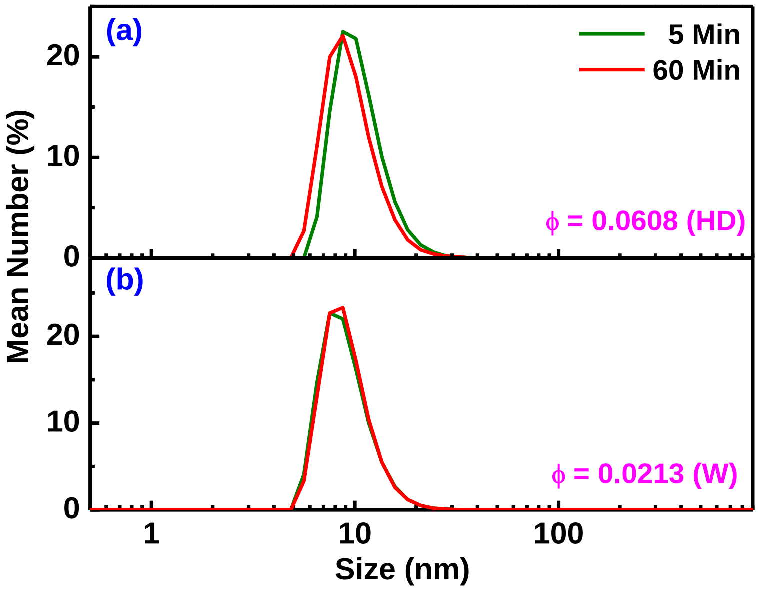

Fig. 4.8: The plot of mean number percentage as a function of particles size at different time intervals after sonication of 5 and 60 minutes for (a): Hexadecane based Fe_3O_4 nanofluids with ϕ=0.0608. (b): Water based Fe_3O_4 nanofluids with ϕ=0.0213.

η studies confirm the long term stability of surface functionalized hexadecane and water based Fe_3O_4 nanofluids. An invariant η with time after sonication is observed in both water based [Fig. 4.9 (a)] and hexadecane based [Fig. 4.9 (b)] Fe_3O_4 nanofluids. Moreover, the flow curves show a Newtonian behavior with least enhancement in η. Finally, the absence of aggregation in the above nanofluids is corroborated by microscopy studies which show no aggregation of particles with elapsed time after sonication.

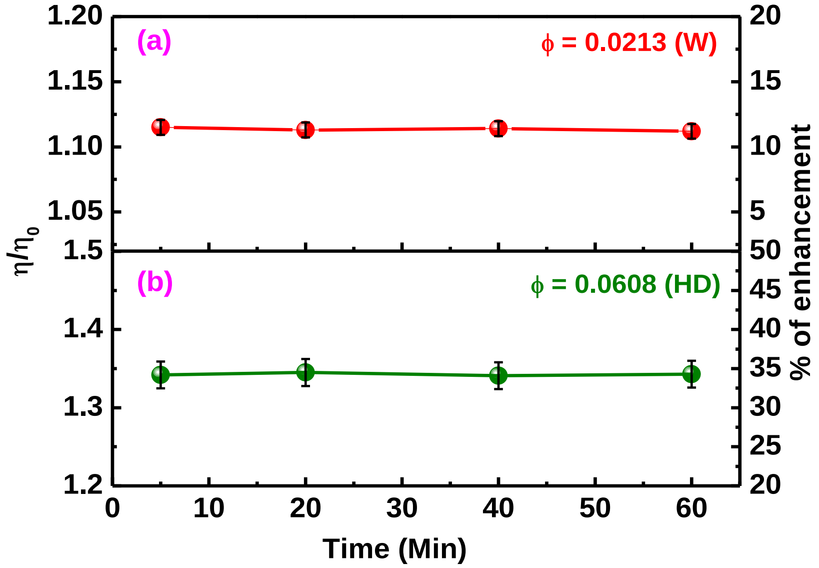

Fig. 4.9: The variation in η/η_0 and the percentage of enhancement of η with time after sonication for (a): Water based Fe_3O_4 nanofluids with $\phi=0.0213$ and (b): Hexadecane based Fe_3O_4 nanofluids with $\phi=0.0608$.

4.3.3 Hexadecane Based Silver Nanofluids

k is measured as a function of time, after sonication, for Ag nanofluids. Figure 4.10 shows the variation of k/k_f and % of k enhancement with time after sonication for hexadecane based Ag nanofluids with $\phi=0.0116$. An invariant k is observed with elapsed time after sonication. Here, the Ag nanoparticles are stabilized by oleylamine surfactant. The amine group of oleylamine binds to the surface of the silver, and the aliphatic chain extends into the nonpolar solvent, preventing aggregation of particles due to steric hindrance. DLS studies (Fig. 4.11) show an invariant particle size distribution (in agreement with XRD results) with time, after sonication, in these nanofluids.

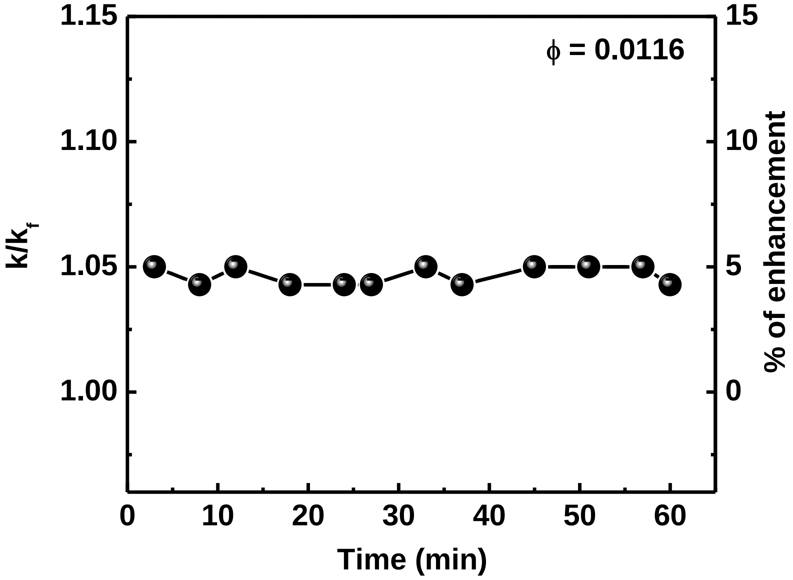

Fig. 4.10: The variation of k/k_f and % of k enhancement with time after sonication for hexadecane based Ag nanofluids with $\phi=0.0116$.

Fig. 4.12 shows the variation in η /η_0 and the percentage of enhancement of η with time after sonication for hexadecane based Ag nanofluids with $\phi=0.0116$. An invariant η ratio observed with elapsed time after sonication, confirms the absence of aggregation in the Ag nanofluids

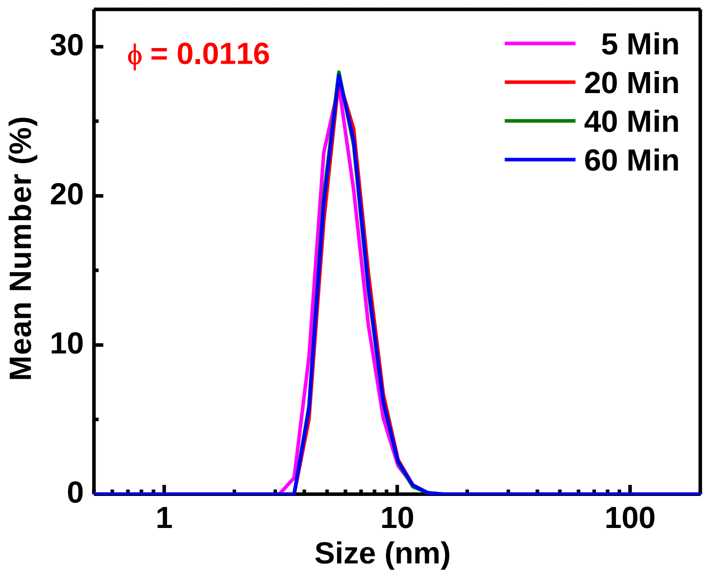

Fig. 4.11 : The plot of mean number percentage as a function of particles size at different time intervals after sonication of 5, 20, 40 and 60 minutes for hexadecane based Ag nanofluids with ϕ=0.0116.

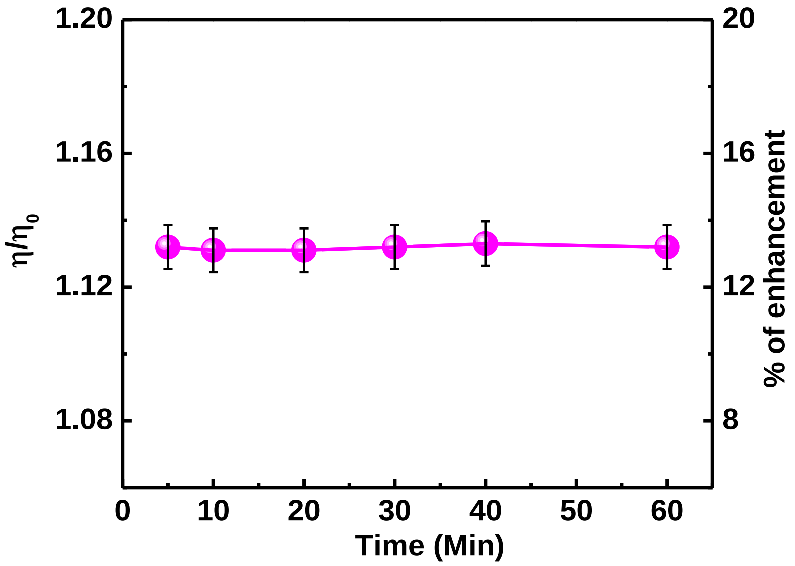

Fig. 4.12: The variation in η/η_0 and the percentage of enhancement of η with time after sonication for hexadecane based Ag nanofluids with ϕ=0.0116.

UV-Vis spectroscopy is often used to detect aggregation in metal nanoparticle. This method relies on the fact that the plasmon band, characteristic of small nanoparticles, is red-shifted and broadened when nanoparticles come into close contact.[280] In the present study, Ag nanofluids show intense surface plasmon resonance absorption (SPR) at 400 nm. Figure 4.13 shows the UV Visible spectra of Ag nanofluids with varying Ag nanoparticle concentrations. No shift in SPR with increasing Ag nanoparticle concentration (from ϕ=0.00001 to ϕ=0.0001) is observed. Moreover, no shift in SPR is observed with time after sonication (Fig. 4.13 inset). This indicates the absence of aggregation in the above nanofluids. Microscopy images also show no aggregation with elapsed time.

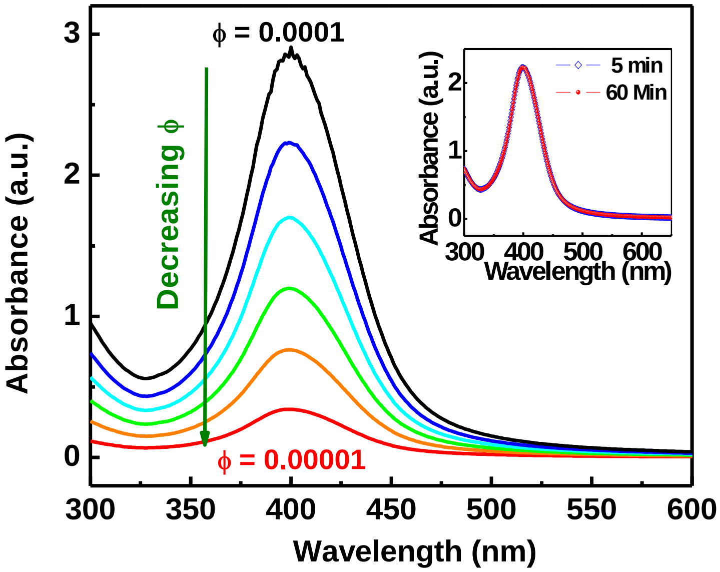

Fig. 4.13: The UV Visible spectra of Ag nanofluids with varying Ag nanoparticle concentrations (from ϕ=0.00001 to ϕ=0.0001). Inset shows the UV visible spectra of silver nanofluids after 5 and 60 minutes of sonication.

4.3.4 Ethylene Glycol Based Copper Oxide Nanofluids

k is measured as a function of time after sonication in EG based CuO nanofluids. Here, the sonication time and power (20 W) are exactly the same as in the case of Fe_3O_4 nanofluid. Figure 4.14 shows the variation of k/k_f and the k enhancement with time, after 30 minutes of sonication for EG based CuO nanofluids of four different particle concentrations of ϕ= 0.0018, 0.0054, 0.0092, and 0.0131. Here, the highest value of k/k_f is observed immediately after sonication. The k/k_f decreases with elapsed time and finally reaches an equilibrium value after a time interval of about 45 minutes. A systematic increase in k/k_f with particle loading is observed. The peak enhancement in k at ϕ=0.0131 is ~ 14%. A similar effect of aggregation on thermal conductivity is observed for water and EG based Cu nanofluids earlier.[138]

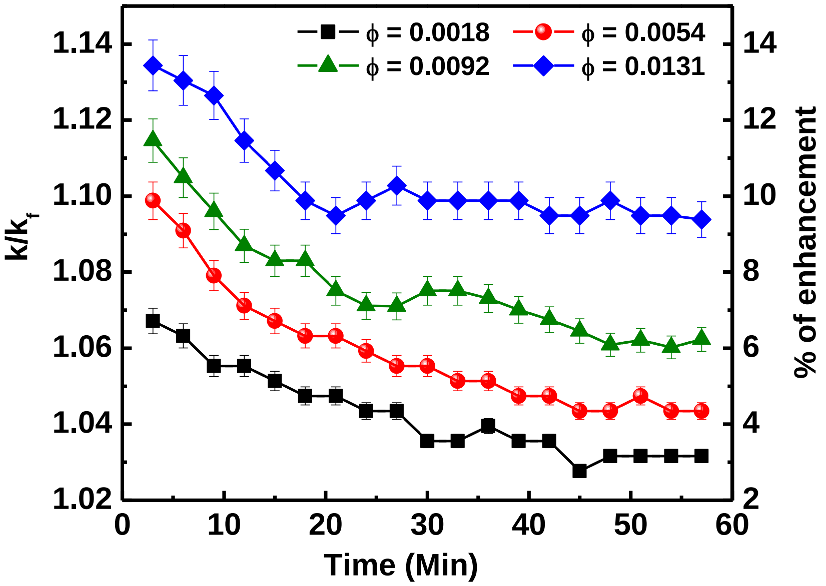

Fig. 4.14: The variation of k/k_f and % of k enhancement with time after sonication for ethylene glycol based CuO nanofluids with ϕ=0.0018, 0.0054, 0.0092, and 0.0131.

In aggregating CuO nanofluids, the ultrasonication leads to disintegration of larger nanoparticle clusters into smaller ones. Due to the absence of stabilizers, once the sonication is stopped, the small nanoparticle clusters reaggregate and form bigger clusters that are subsequently settled. This leads to a decrease in k with elapsed time after sonication. In recent reports, it is shown that the measurement of k, immediately after the ultrasonication, will result in unfinished micro-oscillations of nanoparticles and fluid molecules that can contribute to thermal energy transport, leading to higher k enhancement.[86, 109] If the above prediction is true, base fluid also should have exhibited a time dependent k variation after sonication. We have measured k of base fluids (kerosene, hexadecane, water and EG) as a function of time after sonication where we observe a time independent k. Sonication time and power is exactly the same as in the case of other nanofluids. These finding disprove the micro-oscillation concept.[86, 109]

To confirm the aggregation in CuO nanofluids, the cluster size is measured as a function of time after sonication. Figures 4.15 (a)-(d) shows the mean number percentage as a function of cluster size at different time intervals after sonication of 5, 20, 40, and 60 minutes for EG based CuO nanofluids of different particle loading ϕ=0.0131, 0.0092, 0.0054 and 0.0018 respectively. Figures 4.4 (e)-(h) shows the variation of average particle size with time for the above nanofluids. The average particle size is found to increase with time after sonication in CuO nanofluids. The average size of CuO nanoaggregates have grown from 23 to 95 nm for the lowest concentration, while its value exceeded 300 nm for nanofluid with ϕ=0.0131.

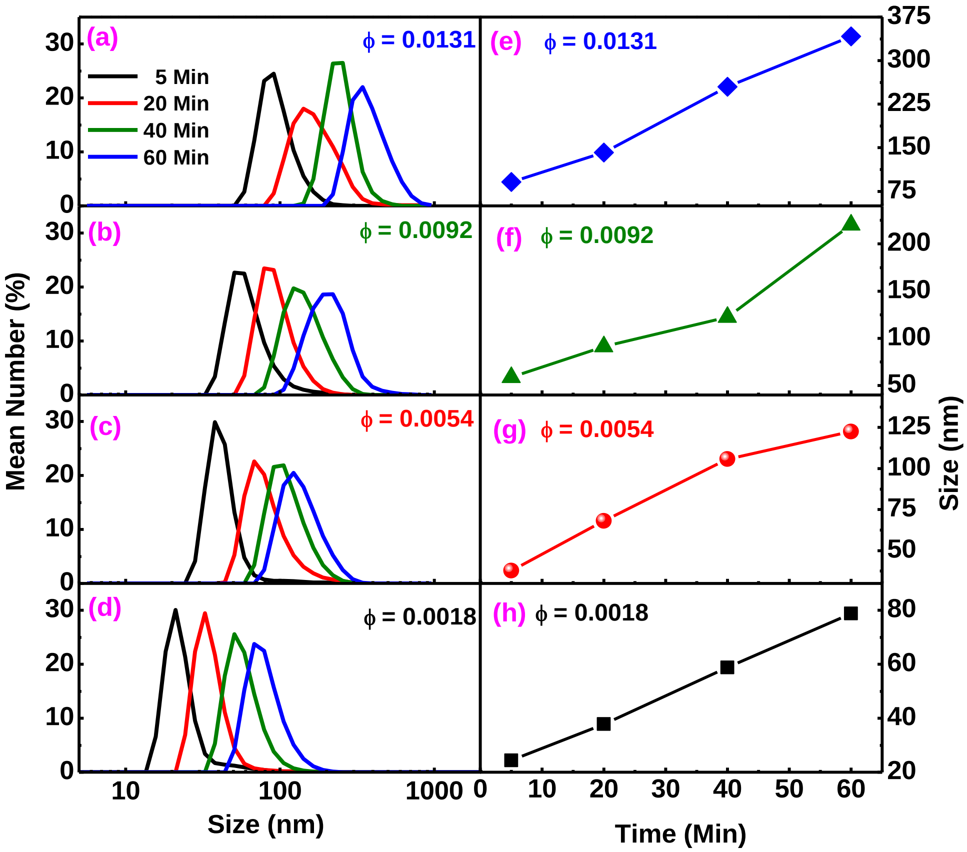

Fig. 4.15: (a), (b), (c) and (d): The plot of mean number percentage as a function of particles size at different time intervals after sonication of 5, 20, 40, and 60 minutes for ethylene glycol based CuO nanofluids with ϕ=0.0131, 0.0092, 0.0054 and 0.0018 respectively. (e), (f), (g) and (h) shows the variation of average particle size with time for ethylene glycol based CuO nanofluids with ϕ=0.0131, 0.0092, 0.0054 and 0.0018 respectively.

The additional evidence for aggregation in CuO nanofluids is obtained from the time dependent rheology studies after sonication. Figure 4.16 shows the variation in viscosity ratio (η/η_0) and the percentage of enhancement of η with time for EG based CuO nanofluids at different particle loading of ϕ=0.0018, 0.0054, 0.0092, and 0.0131. The η ratio increases with time after sonication in all the nanofluids. The nanofluid with lower particle loading shows least enhancement in η with time and the extent of η enhancement is higher for nanofluids with higher particle loading owing to the greater degree of aggregation. As aggregates are formed with time, interaction among nanoparticles increase and the flow resistance also increases, that leads to an increase in η.

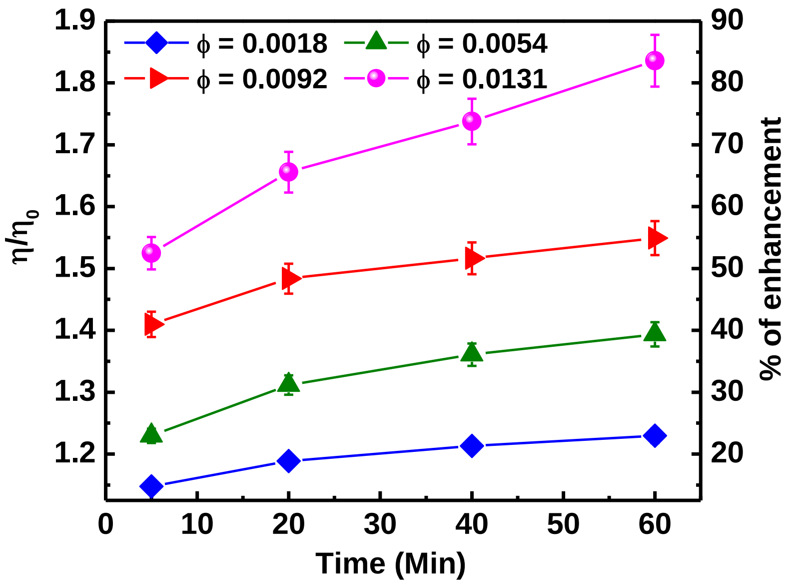

Fig. 4.16: The variation in η /η_0 and the percentage of enhancement of η with time after sonication for ethylene glycol based CuO nanofluids with ϕ=0.0018, 0.0054, 0.0092, and 0.0131.

Flow curves performed at different time intervals after sonication also confirm the progressive aggregation of particles in CuO nanofluids. Figure 4.17 shows the variation of η with shear rate at different intervals after sonication for EG based CuO nanofluids with ϕ=0.0152. A progressive increase in η is observed with time. Moreover, a shear thinning behavior is observed for all time intervals.

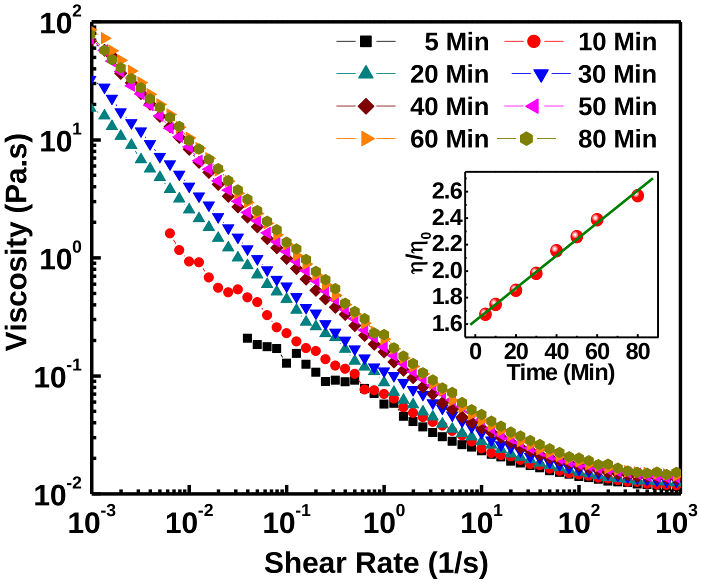

Fig. 4.17: The variation of η with shear rate at different time intervals after sonication for ethylene glycol based CuO nanofluids with ϕ=0.0152. Inset shows the variation of η /η_0 with time after sonication at a shear rate of 50 s^{-1}.

The rapid increase of η at low shear rate indicates the formation of an interacting network of aggregated nanoparticles. As the shear rate is increased, nanoparticle network is broken, leading to a decrease in η. Figure 4.17 inset shows the variation of η /η_0 with time after sonication for EG based CuO nanofluids with ϕ=0.0152, at a shear rate of 50 s^{-1}. η ratio increases linearly with time after sonication. Figure 4.18 shows the variation of η with shear stress at different intervals after sonication for the above nanofluid. A progressive increase of the yield stress and shear-thickening is observed with time. The elapsed time and the concomitant yield stress push the onset of shear thickening to higher stress values. A similar enhancement in shear stress is reported in dielectric glass spheres in mineral oil and magnetite-filled polyethylene glycol (PEG) rods suspended in PEG recently.[281]

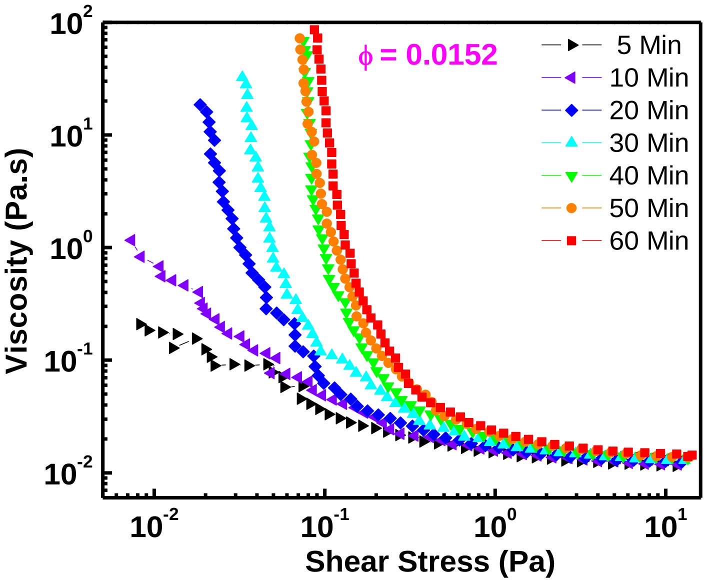

Fig. 4.18: The variation of η with shear stress at different time intervals after sonication for ethylene glycol based CuO nanofluids with ϕ=0.0152.

To obtain macroscopic evidence of the aggregation process, the phase contrast microscopic images are taken at different time intervals. Figure 4.19 shows the microscopy images of CuO based nanofluids at three different time intervals (t=5, 30, and 60 minutes) after sonication for different ϕ values of 0.0054 (a1–a3), 0.0092 (b1–b3) and 0.0131 (c1-c3), respectively. The micrographs confirm that cluster formation in CuO nanofluids with elapsed time after sonication where the cluster size increases with time.

The present study confirms that aggregation has a prominent role on thermal conductivity enhancement of nanofluids. However, the large aggregates and clumps formed by sedimentation have a negative impact on k enhancements in nanofluids.

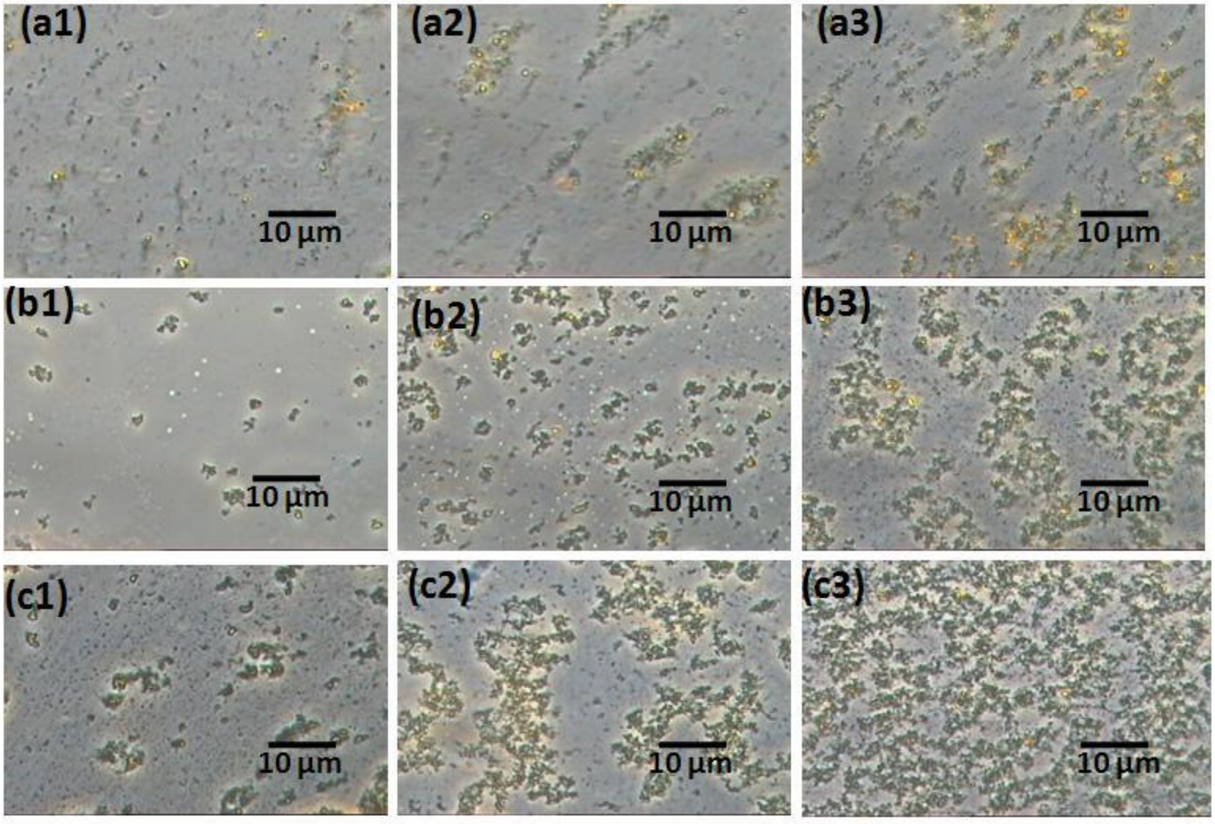

Fig. 4.19: The phase contrast microscopy images taken immediately after sonication, after 30 and 60 minutes of sonication for ethylene glycol based CuO nanofluids ϕ =0.0054 (a1–a3), ϕ=0.0092 (b1–b3), ϕ =0.0131 (c1–c3).

4.4 Conclusions

Stable nanofluids exhibits moderate k enhancement within the predictions of EMT. However, aggregating nanofluids show enhancement in k beyond EMT predictions, immediately after sonication.

The aggregating nanofluids show a time dependent variations in k with elapsed time after sonication. The highest value of k/k_f is observed immediately after sonication, which decreases with elapsed time and finally reaches an equilibrium value after a time interval of about 45 min.

In the absence of stabilizers, the aggregation and the subsequent settling of agglomerates leads to a decrease in k with elapsed time in aggregating nanofluids. The cluster size increases with elapsed time after sonication in aggregating nanofluids. The η ratio also increases with time in these nanofluids. The nanofluid with low particle loading shows a least enhancement in η with time and the extent of η enhancement is higher for nanofluids with higher particle loading, owing to the great degree of aggregation. Moreover, a shear thinning behavior is observed for aggregating nanofluids. The optical micrographs confirm the cluster formation in unstable nanofluids with elapsed time where the cluster size increases with time.

Stable nanofluids with proper steric and electrostatic stabilization show time independent k behavior with time. They show an invariant average particle size distribution and η values with elapsed time. Sterically stabilized Ag nanofluids show no shift in plasmon resonance absorption with time and increasing metal nanoparticle concentration, indicating the absence of aggregation. The surface modified nanofluids show no aggregation (with cluster size > 200 nm) with time in microscopy studies.

The present results enlighten the need of surface functionalization of nanoparticles to improve the dispersion stability of nanofluids with least viscosity enhancement in order to make them ideal for practical applications.

Chapter – V

Tuning of Thermal Conductivity of Nanofluids Using an External Stimulus

Contents

Chapter V | Tuning of Thermal Conductivity of Nanofluids Using an External Stimulus

5.1 Introduction

Magnetic nanofluid is a unique material that has both the liquid and magnetic properties.[282] Since the properties and the location of these fluids can easily be influenced by an external magnetic field, they have recently attracted many scientific, industrial, and commercial applications.[283-285] These fluids have been found to have several fascinating applications such as magneto-optical wavelength filter,[286, 287] optical modulators,[288] nonlinear optical materials,[289] tunable optical fiber filter,[290] optical grating,[291] and optical switches.[292] In addition, they have been a wonderful model system for fundamental studies.[293] Besides they have applications in magneto-fluidic seals, lubricants, density separation, ink jet printers, refrigeration, clutches, tunable dampers, medical diagnostics etc. In the present study, tunable thermal and rheological properties of magnetic nanofluid are demonstrated which is yet another fascinating application of magnetic nanofluid for thermal management. By controlling the linear aggregation length from nano to micron scales, the k and η of the magnetic nanofluid is tuned from a low to very high value.

Stable magnetic nanofluids are prepared by dispersing the oleic acid coated Fe_3O_4 nanoparticles in kerosene and hexadecane. The advantage of this system is that one can achieve controlled aggregation with different chain lengths by varying the magnetic field strength. Moreover, the dispersions had excellent long term stability, as nanoparticles are not influenced by the gravitational force owing to their small size. As the particles are sterically stabilized, no permanent aggregation due to van der Waals attraction occurs. The particles are superparamagnetic in nature where the individual dipoles align under an applied magnetic field, exhibiting magnetizations similar to those of the bulk magnetic material. But in contrast to bulk materials, the suspensions exhibits no remanence (i.e., residual magnetization) i.e. once the field is removed, the oriented dipoles quickly relax by Brownian and Neel relaxation phenomena. Thus, the aggregation phenomenon is perfectly reversible here. This chapter focuses on results on field induced k and η enhancement of magnetite nanofluids.

5.2 Field Induced Thermal Conductivity Enhancement in Magnetite Nanofluids

In the present study, k of magnetic nanofluids is measured under varying magnetic field strengths and field orientations. For the measurement, the sample cell containing magnetite nanofluid is kept inside a solenoid-like electromagnet and the current is varied to change the magnetic field strength. The k measurements are made two minutes after achieving the desired magnetic field; this time is sufficient for equilibrating the structures formed in the fluid. All the measurements have been done at 25 °C.

5.2.1 Effect of Volume Fraction

k is measured as a function of magnetic field strength for kerosene and hexadecane based Fe_3O_4 nanofluids having different ϕ. Figure 5.1 shows the variation of the k ratio (k/k_f) and the percentage of k enhancement with magnetic field strength for kerosene based Fe_3O_4 nanofluids having different particle loading, where the field orientation is parallel to the temperature gradient. The k/k_f values remain unchanged irrespective of the magnetic field strength for the lowest particle loading (ϕ = 0.00031). However, for nanofluids with higher particle loading, the k/k_f increases with increase in applied field strength. The higher the particle loading, the larger is k enhancement for a given magnetic field strength. A maximum k enhancement of 125% is observed for the nanofluid with ϕ = 0.0171 at a field strength of 378 G.

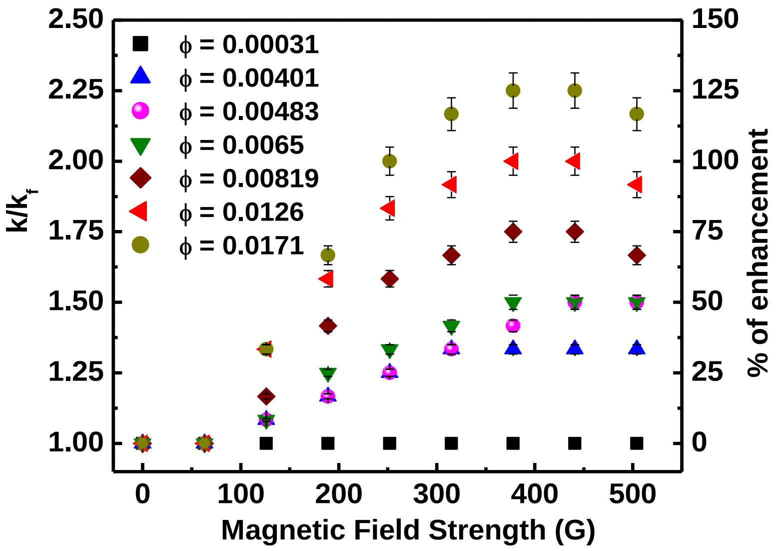

Fig. 5.1: The k/k_f and % of enhancement in k as a function of external magnetic field strength for kerosene based Fe_3O_4 nanofluids with ϕ = 0.00031, 0.00401, 0.00483, 0.0065, 0.00819, 0.0126 and 0.0171. The applied magnetic field is parallel to temperature gradient here.

The large enhancement in k in presence of magnetic field that is parallel to temperature gradient is explained as follows: Ferrofluids consist of a colloidal suspension of single domain superparamagnetic nanoparticles with a magnetic moment 'm'. The interparticle dipole-dipole interaction $U_d(ij)$ between the magnetic particles is[294]

$$U_d(ij) = -\left[3\frac{(m_i \cdot r_{ij})(m_j \cdot r_{ij})}{r_{ij}^5} - \frac{(m_i \cdot m_j)}{r_{ij}^3}\right], r_{ij} = r_i - r_j \tag{5.1}$$

The dipolar interaction energy depends on the distance r_{ij} between the ith and jth particles and the mutual orientation of their magnetic moments m_i and m_j. When the dipolar interaction energy becomes sufficiently strong, the magnetic particles form chain like structures. The effective attraction between two ferromagnetic particles is described by a coupling constant $L = U_d(ij)/\ k_B T$, which involves two competing factors: magnetic dipolar interaction energy $U_d(ij)$ and thermal energy, where, k_B is the Boltzmann constant and T is the temperature. Dipolar structure formation is expected when the dipolar potential exceeds thermal fluctuations; that is, for a dipolar coupling constant $L > 1$. Without any external magnetic field, the magnetic moments of the scatterers are oriented in random direction. In the presence of magnetic field, the nanoparticles align in the direction of magnetic field when the magnetic dipolar interaction energy $U_d(ij)$ dominates over the thermal energy $k_B T$. The equilibrium chain length and flexibility of the chains depends on the orientational correlations between the magnetic moments of particles inside a chain. The chain flexibility decreases with field strength and in strong fields, the chain aggregate resembles a stiff rod like chain.[294]

The particle concentration for hard-sphere suspensions is related to its volume fraction, $\phi = NV_p$, where N is the number density of particles and V_p is their volume (= $4\pi/3r^3$, where r is the particle of radius). The extent of chain formation in presence of an external magnetic field increases with increase in ϕ, since the number of particles per unit volume increases with increase in ϕ. Thus for a given magnetic field strength, the enhancement in k will be higher for the nanofluid with maximum particle loading. Further, the saturation magnetization of Fe_3O_4 nanoparticle dispersions also increases with increase in nanoparticle concentration.[295]

Considering the particles as spherical, the interparticle spacing (IPS) for a colloidal dispersion of monodisperse particles is given by [296]

$$IPS = 2r\left[\left(\frac{\phi_m}{\phi}\right)^{1/3} - 1\right] \tag{5.2}$$

Where ‘r’ is the particle radius and ϕ_m is the maximum particle packing fraction which is 0.63 for random dense packing. The IPS for the concentrations 0.031, 0.401, 0.819, 1.71 are 117.4, 44.15, 32.7 and 23.4 nm respectively. In-situ cryogenic transmission electron microscopy observations of magnetite nanoparticle dispersions under a magnetic field confirmed columnar structures exhibiting distorted hexagonal symmetry.[297] Therefore, when the magnetic field direction is parallel to the temperature gradient inside the fluid, heat energy is effectively transported through the chain like aggregates. This is the plausible reason for the large enhancement in k is observed at higher fields.

Mean field models predicts series and parallel modes of thermal conduction through nanofluids. The parallel mode has the geometric configuration that allows the most efficient means of heat propagation.[298] Therefore, extremely large k enhancement is possible with parallel modes. Hashin and Shtrikman (HS) bounds for k of a nanofluid, on the basis of ϕ alone is given by[299]

$$k_f\left[1+\frac{3\phi[k]}{3k_f+(1-\phi)\kappa}\right] \le k \le \left[1-\frac{3(1-\phi)[k]}{3k_p-\phi[k]}\right]k_p \tag{5.3}$$

Figure 5.2 shows the percentage of enhancement of k without and with magnetic field of different strengths for kerosene based Fe_3O_4 nanofluids. The Maxwell upper, lower bounds, series and parallel bound fits are also shown in Fig. 5.2. In the lower HS limit, nanoparticles are well suspended and conduction is through series modes whereas in the upper HS limit, the conduction path is through dispersed particles. In the absence of magnetic field, the particles are well dispersed, the nanofluids exhibit series mode conduction and the observed variation of k/k_f with ϕ is well within the lower Maxwell limit. In the limit $(\phi k_p/k_f) >> 1$, (k_p and k_f are thermal conductivities of particles and fluid respectively) the predicted values of k/k_f for the upper HS and parallel modes are $(2\phi/3)k_p/k_f$ and $\phi k_p/k_f$ respectively. It can be seen that the experimental data points at the highest magnetic field falls within the parallel mode of conduction.

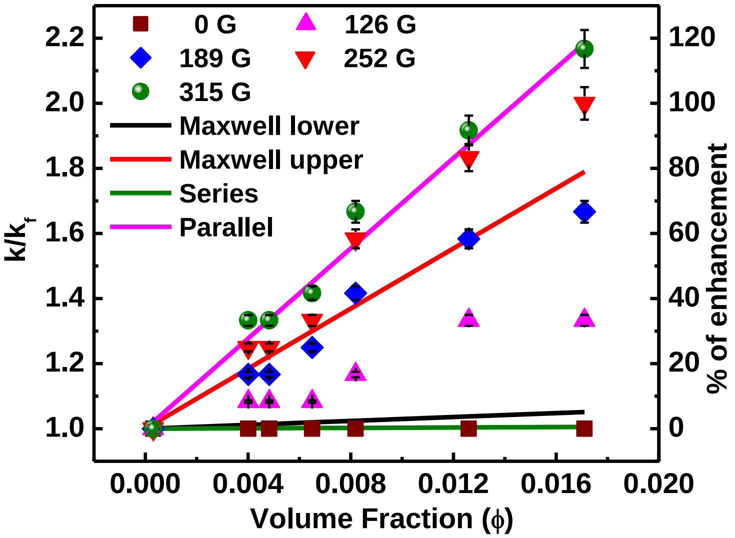

Fig. 5.2: The variation of k/k_f with volume fraction in absence and in presence of different magnetic field strengths of 126, 189, 252 and 315 G for kerosene based Fe_3O_4 nanofluids fitted with Maxwell upper and lower, HS upper and lower bounds.

It was demonstrated that for magnetite nanoparticles, an average particle diameter less than 10 nm is insufficient for significant dipolar structure formation at zero field.[300] Dipolar structure formation is expected when the dipolar potential exceeds thermal fluctuations. The calculated value of L is found to be ~ 0.3 for 10 nm Fe_3O_4 particles coated with a 2 nm thick organic surfactant layer.[301] Since the particles used in our studies is of ~ 10 nm size and capped with a surfactant, the formation of dipolar structures at zero field is ruled out. This is also confirmed from TEM data. Further, the observed k/k_f variation with ϕ at zero field also supports the series mode conduction and is in agreement with the predictions of EMT for well dispersed stable nanofluids. As the magnetic field strength is increased progressively, continuous conduction paths emerge along the nanoparticle chains that result from series to parallel mode of conduction. At a magnetic field strength of 315 G, the k/k_f data fits fairly well with the parallel mode conduction.

Figure 5.3 shows the k/k_f and the corresponding percentage of enhancement in k as a function of applied magnetic field for kerosene based Fe_3O_4 nanofluids with ϕ=0.063 and 0.049. Here, the k started to increase drastically at very low magnetic fields. The highest value of enhancement in k observed is 300% for nanofluid with a particle loading of ϕ=0.063. A drop in the k is observed at high magnetic field strengths. After the formation of linear chains, they come together to form denser chains due to interaction between fluctuations in the shape of the adjacent columns. The decrease in k observed above a critical magnetic field strength is expected to be due to 'zippering' of chains.

For two rigid chains of magnetic colloids aligned parallel to one another, the interaction energy curve consists of an attractive energy well if the chains have different length and a repulsive interaction for parallel chains (of same length) as they approach one another laterally.[302] When the chains are of different lengths or shifted with respect to one another, zippering of chains can take place due to attractive energy well. The lowest energy state of the system as predicted by the Gross model consists of clusters containing zipped chains.[303] The head-to-tail aggregation necessary to form the single chains does not involve any significant energy barrier and therefore the system is not kinetically limited from reaching the lowest energy state.[302]

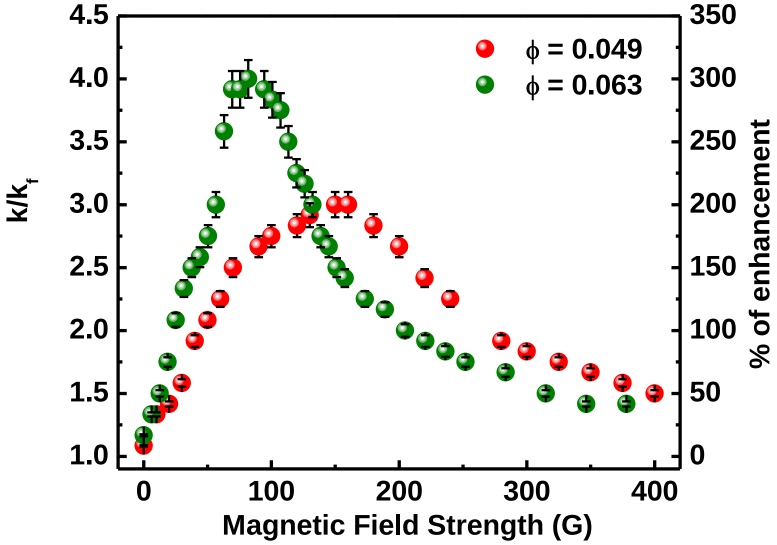

Fig. 5.3: The k/k$_f$ and % of enhancement in k as a function of external magnetic field strength for kerosene based Fe_3O_4 nanofluids with ϕ = 0.049 and 0.063. The applied magnetic field is parallel to temperature gradient here.

The chain with a dipole moment (m) per unit length $m/d \sim \mu_0 \chi d^2 H$ interacts with mean squared lateral field induced by chain fluctuations,[304] where, d is the nanoparticle size, H is the magnetic field strength, μ_0 is the vacuum magnetic permeability and χ magnetic susceptibility The interaction energy per unit length is on the order

$$U \sim (m/d)\langle H^2 \rangle^{1/2} \sim \frac{\chi H (\mu_0 k_B T)^{1/2} d^{5/2}}{z^2} \qquad (5.4)$$

and can be either repulsive or attractive. This energy has strong dependence on the field strength H and separation (z) between the chains. Two chains laterally coalesce when this energy becomes sufficient enough to overcome the potential energy barrier for the lateral aggregation. Due to the lateral aggregation at critical fields, the separation distance (z) between the columns now increases which results in a decrease in U .

To confirm the lateral overlap (zippering) of chains, phase contrast microscopic studies under external magnetic field is carried out at sufficiently high magnetic field strengths. Figure 5.4 (a) shows the micrograph of kerosene based Fe_3O_4 nanofluids with $\phi = 0.05$ in the absence of external magnetic field, where no aggregates are visible. Figures 5.4 (b)-(k) shows the micrograph of the nanofluid in presence of increasing magnetic strengths. At low magnetic field strength [Fig. 5.4 (b)], there is formation of small dipolar chains, whose length increases with increasing magnetic field strength [Fig. 5.4 (c)], resulting in an evenly spaced single nanoparticle chains throughout the nanofluid volume. At very high magnetic field strengths [Figs. (d)-(k)], zippering of the dipolar chain is evident in the microscopic images. Figure 5.4 (l) shows the image after switching off the magnetic field where no permanent aggregates are visible. This confirms the perfect reversibility of the dipolar chains formed in the fluid.

As the nanoparticles starts to form aggregates of larger size or chains, the convection velocity $\upsilon = \sqrt{\frac{18k_BT}{\pi\rho d^3}}$ drops drastically due to the cubic dependence on the particle size or the aspect ratio of the long chain. Therefore, the Brownian motion decreases as the chain length increases. As the convection velocity decreases with increasing magnetic field, the observed enhancement in k cannot be due to the microconvection mechanism. These findings show that microconvection is not the key mechanism responsible for k enhancements in nanofluids and aggregation has a more prominent role.

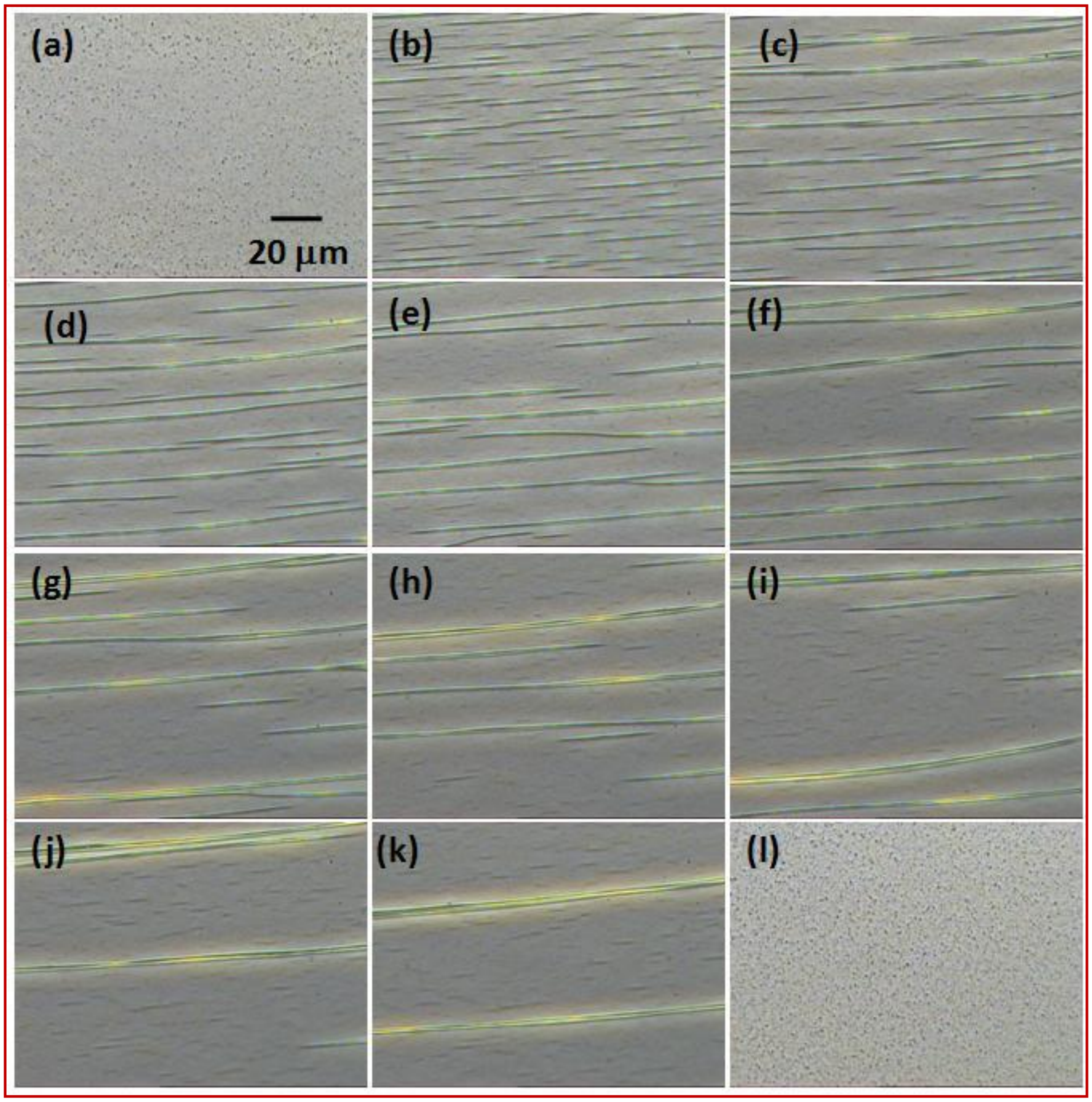

Fig. 5.4: The phase contrast microscopy images of kerosene based Fe_3O_4 nanofluids with $\phi = 0.05$ (a) In the absence of external magnetic field, (b) to (k) In presence of increasing magnetic field and (l) After removal of magnetic field.

5.2.2 Effect of Magnetic Field Orientation

To obtain better insight into the effect of magnetic field orientation (i.e. the orientation of nanochains with respect to the heat flow direction) on k enhancement, thermal conductivity measurements have been done under different magnetic field orientations with respect to the thermal gradient. Figure 5.5 shows the variation of k/k_f with magnetic field strength for kerosene based Fe_3O_4 nanofluids with $\phi = 0.045$ under different field orientations of 0, 20, 70 and 90°.

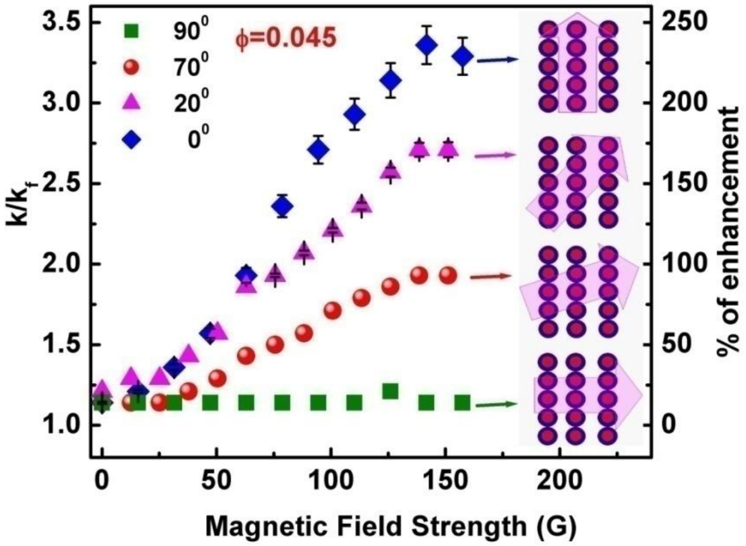

Fig. 5.5: The k/k_f and % of enhancement of k as a function of external magnetic field strength for kerosene based Fe_3O_4 nanofluids with $\phi = 0.045$ in presence of different field orientations of 0, 20, 70 and 90°. Inset shows the schematics of direction of heat and possible nanoparticle structures for different field directions.

The maximum enhancement in k is observed when the field direction is exactly parallel to the thermal gradient whereas practically no enhancement is observed when field is perpendicular to thermal gradient. A gradual reduction in the k enhancement is observed as the field direction is shifted from parallel to perpendicular direction with respect to thermal gradient. Inset of Fig. 5.5 shows the schematics of possible nanoparticle orientation with respect to thermal gradient when the magnetic field direction is varied from parallel to perpendicular direction.

Figure 5.6 shows the variation of k/k_f with magnetic field strength for hexadecane based Fe_3O_4 nanofluids with $\phi = 0.04$ under different field orientations of 0, 20 and 90°. Here, a similar variation is observed at different magnetic field orientation, as in the case of kerosene based nanofluid. As the parallel mode has a geometric configuration that allows the most efficient means of heat propagation through nanoparticle paths, large k enhancement is achieved with parallel fields. No enhancement in k is observed when field is perpendicular to thermal gradient.

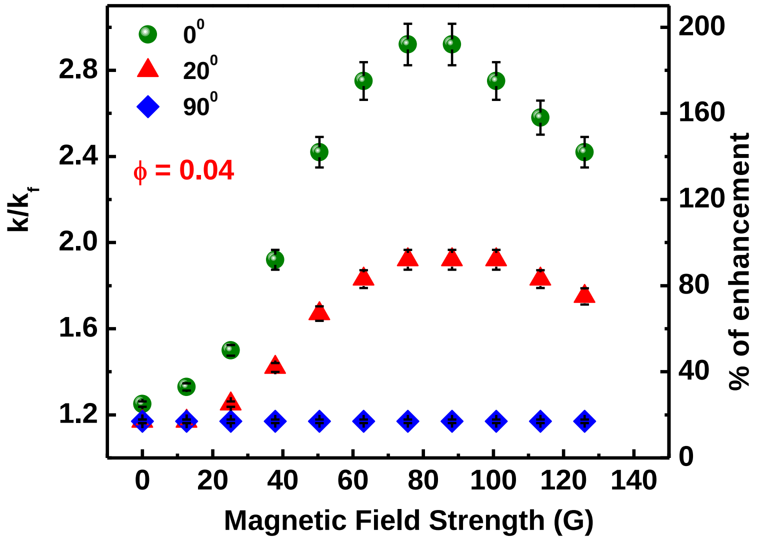

Fig. 5.6: The thermal conductivity ratio (k/k_f) and % of enhancement of k as a function of external magnetic field strength for hexadecane based Fe_3O_4 nanofluids with $\phi = 0.04$ in presence of different field orientations of 0, 20 and 90°.

5.3 Field Induced Viscosity Enhancement in Magnetite Nanofluids

Figure 5.7 shows the variation of η ratio as a function of magnetic field strength for kerosene based Fe_3O_4 nanofluids (d=6.1 nm) with different volume fractions of particles at a constant shear rate of 50 s^{-1}. No change in η ratio is observed with increasing magnetic field strength irrespective of the nanofluid particle loading. Figure 5.8 show the variation of η ratio as a function of magnetic field strength for kerosene based Fe_3O_4 nanofluids (d=9.5 nm) with different particle loading at a constant shear rate of 50 s^{-1}. Least variation in η ratio is observed, up to a magnetic field strength of 200 G, for all the concentrations studied. Above 200 G, η ratio increases with increase in magnetic field strength. The higher the particle loading, the larger the η enhancement for a particular magnetic field strength.

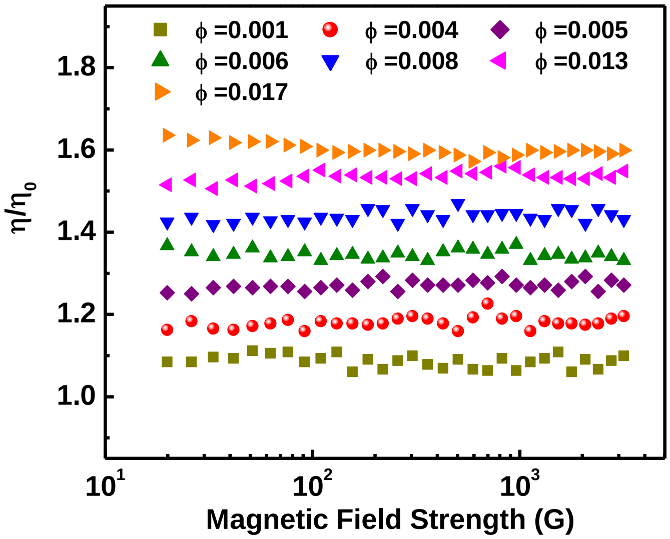

Fig. 5.7: The viscosity ratio as a function of magnetic field strength for kerosene based Fe_3O_4 nanofluids (d=6.7 nm) with ϕ = 0.001, 0.004, 0.005, 0.006, 0.008, 0.013 and 0.0171.

For magnetic fluid in a shear flow, the particles inside the fluid start to rotate in the flow with the axis of rotation parallel to the vorticity of the flow. Applying an external magnetic field to the system, and assuming that the field is collinear with the vorticity of the flow, the magnetic moment of particles align with the field and particles rotate around the field direction; with no influence on the flow. In contrast, if the field is perpendicular to vorticity, the viscous friction tilts particle magnetic moment against the field direction, if the moment is spatially fixed in the particle. The resulting finite angle between the magnetic moment and the field direction gives rise to a magnetic torque counteracting the viscous torque that try to realign the moment with the field. The counteraction of the torques results in a hindrance of the free rotation of the particles in the flow, and thus in an increase in the fluid viscosity.

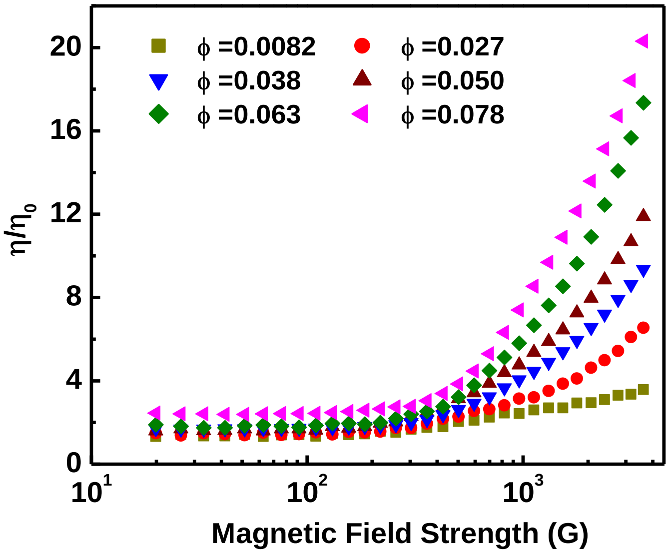

Fig. 5.8: The viscosity ratio as a function of magnetic field strength for kerosene based Fe_3O_4 nanofluids (d=9.5 nm) with ϕ = 0.0082, 0.027, 0.038, 0.05, 0.063 and 0.078.

According to the chain formation model,[305] the magnetoviscous effect is described as a result of the formation of chain-like structures due to strong interparticle interaction under the influence of a magnetic field as discussed in section 5.2.1. At low field strength, the tendency of the nanoparticle magnetic moments to alignment is overcome by thermal agitation. As the magnetic field intensity increases, the interaction among nanoparticles also increases. Consequently, the nanoparticle alignment along the direction of the field is intensified resulting in an increase in flow resistance which leads to an increase in η.

The extent of chain formation in ferrofluids depends on the saturation magnetization of the constituting magnetic nanoparticle. The saturation magnetization is directly proportional to nanoparticle size. The measured M_S values are 28 and 57 emu/g respectively for 6.1 and 9.5 nm size Fe_3O_4 nanoparticles. Thus for a given magnetic field strength, the extent of chain formation will be low in Fe_3O_4 nanofluids comprising of 6.1 nm sized nanoparticles, compared to 9.5 nm sized nanofluids. Apparently the field induced dipolar interaction is not sufficiently strong to induce the formation of a considerable number of chains[241] and that may be the reason for the observed invariant η with the rise in magnetic field strength for 6.1 nm sized nanofluids. Moreover, η enhancement with field strength diminishes with increasing shear rate, an effect which can generally be explained by the rupture of agglomerates of magnetic particles which were formed by the interparticle interaction due to viscous forces in the shear flow.[306] For 9.5 nm sized magnetic nanofluids, the formation of weak dipolar chains resulted no change in η up to a magnetic field strength of 200 G. A further increase of the magnetic field strength results in rigid chains along the field lines and hence the η starts to increase. This interpretation is supported by the microscopy images of the microstructure of the nanofluids in presence of magnetic field.

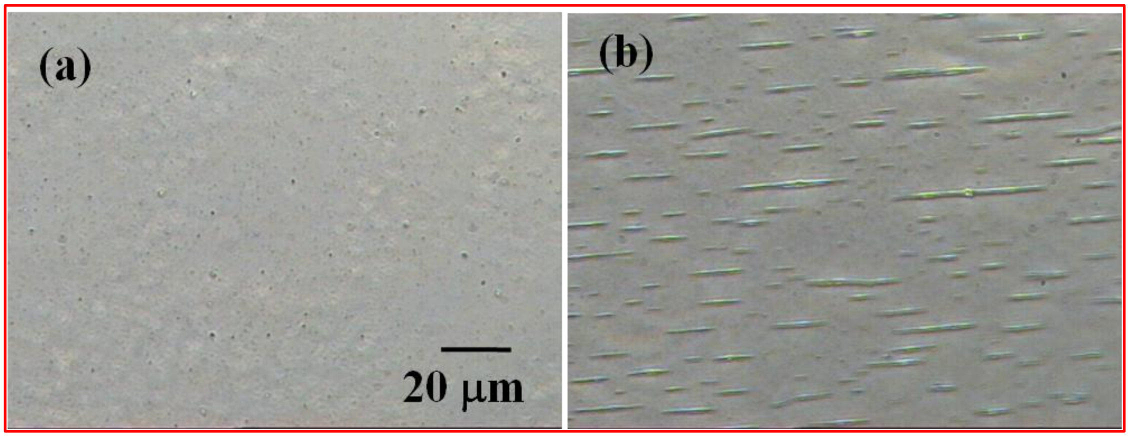

Fig. 5.9: The phase contrast microscopy images taken in presence of identical field conditions for kerosene based Fe_3O_4 nanofluids with $\phi = 0.017$ having particle size of (a) 6.1 nm and (b) 9.5 nm respectively.

These pictures are taken in a Fe_3O_4 nanofluid with ϕ=0.017, shows progressive evolution of chain like structures occurring in the case of the 9.5 nm particles [Fig. 5.9 (b)], but such structures are absent in the case of the 6.1nm particles [Fig. 5.9 (a)], even at the highest field strength.

5.4 Reversibly Tunable Thermal Conductivity and Viscosity in Magnetite Nanofluids

Figure 5.10 shows the k/k_f of kerosene based Fe_3O_4 nanofluid with ϕ=0.026 during rise and decay of applied magnetic field. It can be seen that the enhancement starts above 20 G. Further increase in magnetic field leads to a drastic enhancement in the k. The maximum enhancement of k ~128%; is observed at a magnetic field of 94.5 G, above which the k value starts to decrease slightly. While lowering the magnetic field, the k value shows a small hysteresis but comes back to the original value when the magnetic field is turned off.

The observed hysteresis can be explained in terms of the relaxation times of nanoparticles in the fluid. In ferrofluids, nanoparticles are free to rotate independently from each other and are aligned by an external magnetic field. After turning off the field, the dipole moments can relax by Brownian motion and Neel rotation due to particle and spin rotation respectively.[1] The Brownian relaxation is achieved via bulk rotation diffusion of particles in the fluid and the relaxation time is given by $\tau_B = {}^{3V_{hy}\,\eta}\!/_{k_B}T$, where V_{hy} is the hydrodynamic volume of the particle and η is the dynamic viscosity. Neel relaxation is attributed to the rotation of the moment in the particle with a relaxation time given by $\tau_N = \tau_0 \exp\left({KV_{hy}}/{k_B} \, T \right)$ where K is the anisotropy constant, τ_0 is typically of the order of a few nanoseconds.

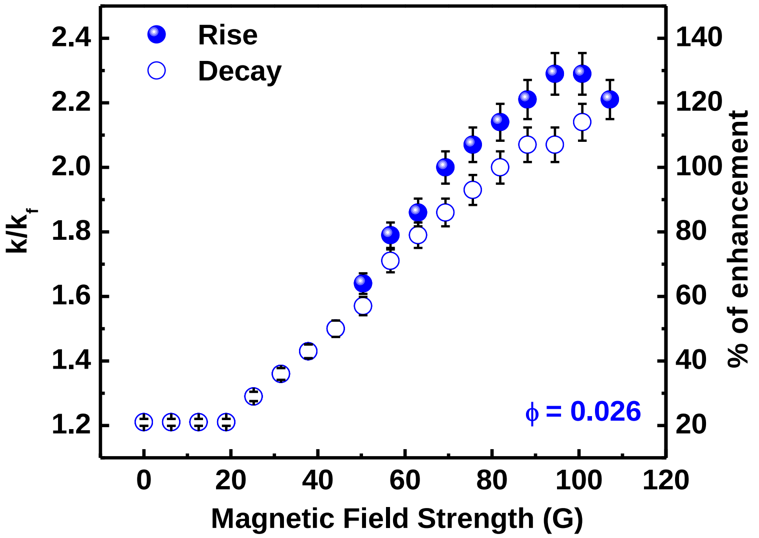

Fig. 5.10: The k/k$_f$ and % of enhancement in k as a function of increasing and decreasing applied magnetic field strengths for kerosene based Fe_3O_4 nanofluids with ϕ = 0.026.

For a particle of 10 nm size, the value of τ_N and τ_B are 10^{-9} and 7.6 x 10^{-7}s respectively. However, the value of τ_N increases sharply with the size of the particle due to the exponential dependence on V_{hy}. Typically, the k measurement requires 30 seconds, which is much larger than τ_B of primary nanoparticles. After the magnetic field is switched off, the net magnetization disappear due to the statistical reorientation of the nanoparticles with an effective relaxation time τ_{eff} that is given by $\tau_{eff} = \frac{\tau_B \tau_N}{\tau_B + \tau_N}$.[307] Therefore, the Brownian relaxation time increases linearly with the particle volume and the Neel relaxation time raises exponentially with increasing particle size. Thus, for small particles, the Neel process dominates while Brownian relaxation dominates for large particles. For Fe_3O_4, the critical size for the transition from Neel to Brownian relaxation is about 13 nm. When the clusters of nanoparticles are formed, the relaxation times can be much larger than the measurement times, which is the reason for the observed hysteresis at higher applied magnetic field.

The variation of η as a function of magnetic field strength for kerosene based Fe_3O_4 nanofluid with $\phi = 0.026$ during the rise and decay of field, at a constant shear rate of 50 s^{-1} is shown in Fig. 5.11.

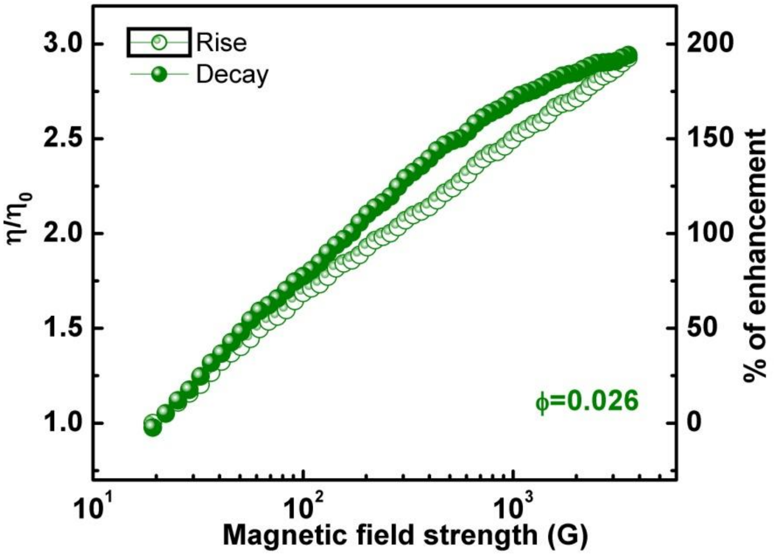

Fig. 5.11: The η/η_0 and % of enhancement in η as a function of increasing and decreasing applied magnetic field strengths for kerosene based Fe_3O_4 nanofluids with $\phi = 0.026$.

The lower η values observed during the decay of magnetic field strength compared to the rise is attributed to the fact that the structures formed during the rise of magnetic field takes longer time than the measurement time for the relaxation. The typical measurement time between each data point is 10 seconds. However, after removal of the magnetic field, η values restore to its original value, indicating the absence of any permanent aggregation under external magnetic field.

Figure 5.12 shows the k/k_f and the corresponding k enhancement as a function of applied magnetic field for kerosene based Fe_3O_4 with ϕ=0.045. The variation of k/k_f at three different magnetic cycles (rise and decay) shows that the enhancement is reversible with a slight hysteresis. The maximum enhancement observed is 216% at an applied magnetic field strength of 101 Gauss.

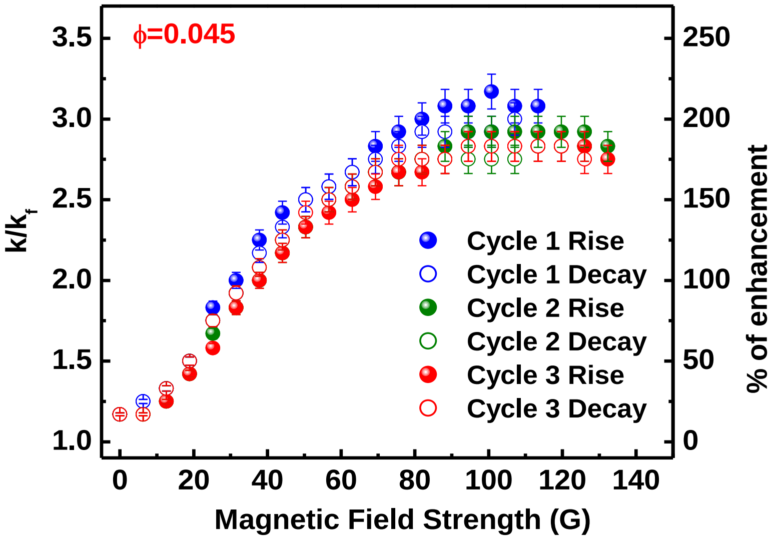

Fig. 5.12: The k/k_f and % of enhancement in k as a function of increasing and decreasing applied magnetic field strengths at three different magnetic cycles for kerosene based Fe_3O_4 nanofluids with ϕ = 0.045.

The observed reversible tunable thermal property of nanofluid may find many technological applications for this fluid in nanoelectromechanical system (NEMS) and microelectromechanical system (MEMS) based devices. For example, depending upon the cooling requirement, the current or magnetic field can be precisely programmed to obtain the desired level of k enhancement or cooling. The mechanism of heat transport from a cylindrical device with nanofluid coolant around it, without and with magnetic field is depicted in the inset of Fig. 5.13. When the field is off, the nanoparticles behave as a normal fluid with random arrangement of particles [Fig. 5.13(a)]. When the field is turned on, the parallel mode conduction leads to drastic enhancement of TC [Fig. 5.13(b)].

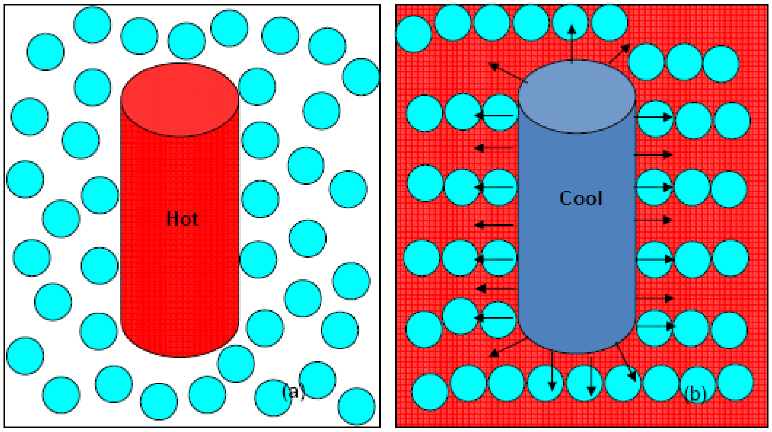

Fig. 5.13: The schematic of the mechanism of heat transport from a cylindrical device immersed in nanofluid (a): Without and (b): With magnetic field.

Figure 5.14 shows the η/η_0 and the corresponding η enhancement as a function of applied magnetic field for kerosene based Fe_3O_4 with ϕ=0.045. The variation of η at two different magnetic cycles (rise and decay) shows that the enhancement in η is reversible with a slight hysteresis. Moreover, the η of the suspension shows monotonic increase with magnetic field. Since the parallel plate gap of the rheometer is much smaller than the path length of the sample used in k measurement, the zippering and subsequent collapse of chains may not be occurring in the former case.

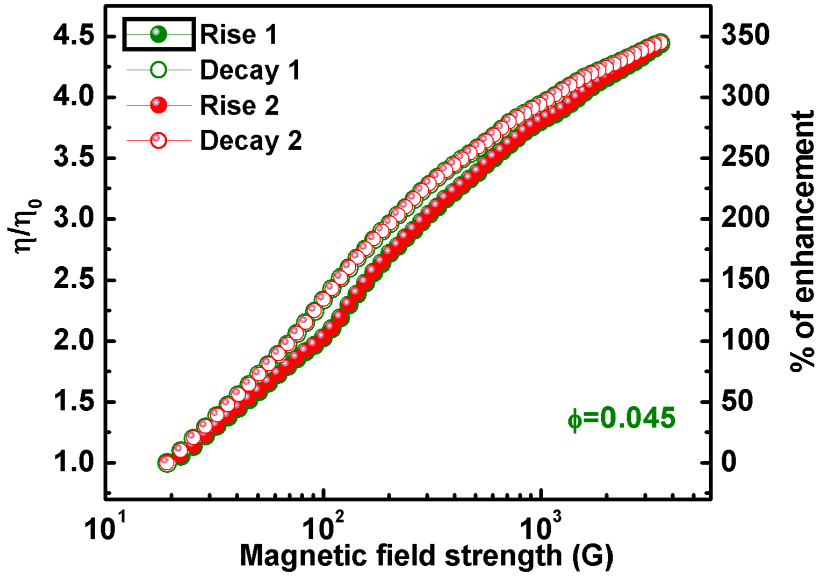

Fig. 5.14: The η/η_0 and % of enhancement in η as a function of increasing and decreasing applied magnetic field strengths at two different magnetic cycles for kerosene based Fe_3O_4 nanofluids with $\phi = 0.045$.

Reversibly tunable field induced k enhancement is also exhibited by stable hexadecane based Fe_3O_4 nanofluids Figures 5.15 (a) and (b) shows the variation of k/k_f during the rise and decay of applied magnetic field, for hexadecane based Fe_3O_4 nanofluids with $\phi = 0.03$ and $\phi = 0.02$ respectively. Here also, k enhancement is perfectly reversible with a slight hysteresis. The maximum k enhancement observed is 135 (at 113 G) and 100% (126 G) for nanofluids with particle loading of $\phi=0.03$ and $\phi=0.02$ respectively.

Therefore, application of magnetic field not only enhance the thermal k of the nanofluid but also the rheological properties of the nanofluid.[308] Such field induced enhancements in k and η of ferrofluids can be exploited for a number of technological applications such as damping cum cooling.[309]

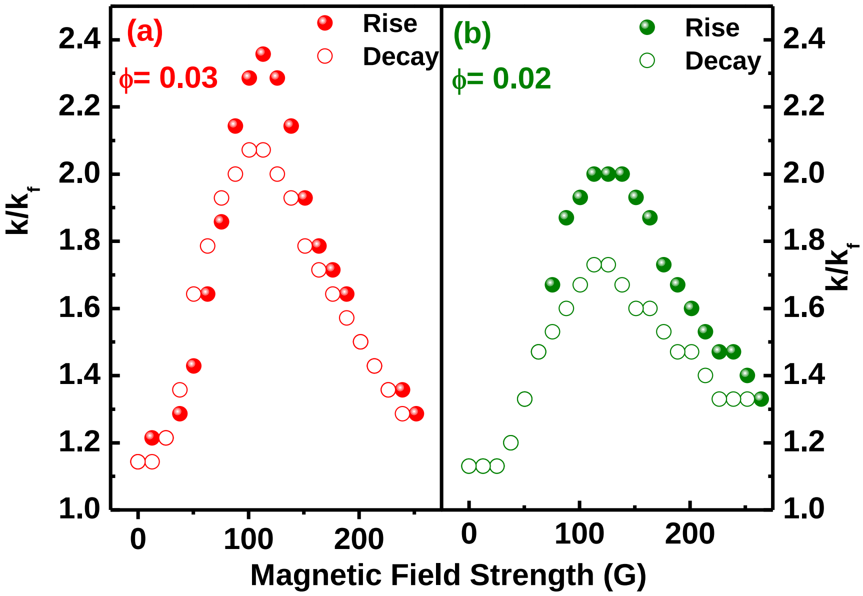

Fig. 5.15: The k/k_f as a function of increasing and decreasing applied magnetic field strengths for hexadecane based Fe_3O_4 nanofluids having (a): $\phi = 0.03$ and (b): $\phi = 0.02$.

Figures 5.16 (a) and (b) shows the viscous and thermal conductivity change of hexadecane based Fe_3O_4 nanofluid with a $\phi = 0.067$, where magnetic field strength is varied in a stepwise manner. Here, both k/k_f and η/η_0 measurements are carried out under on–off conditions where the on and off conditions correspond to a magnetic field strength of 120 G and zero respectively. The shear rate for η measurement was 50 s^{-1}. The steady η with time for a given magnetic field indicates that the magnetic structures are not broken by the shear flow.

Under the influence of an external magnetic field, the magnetic moment of the particle aligns in the field direction and the particle rotate around the field direction. When the field is perpendicular to vorticity, the viscous friction tilts the magnetic moment against the field direction. The resulting finite angle between the magnetic moment and the field direction give rise to a magnetic torque counteracting the viscous torque that tries to realign the moment along the field direction. A hindrance of the free rotation of the particles in the flow occurs due to the counteraction of the torques. Further it also increases the viscosity of the fluid.[310]

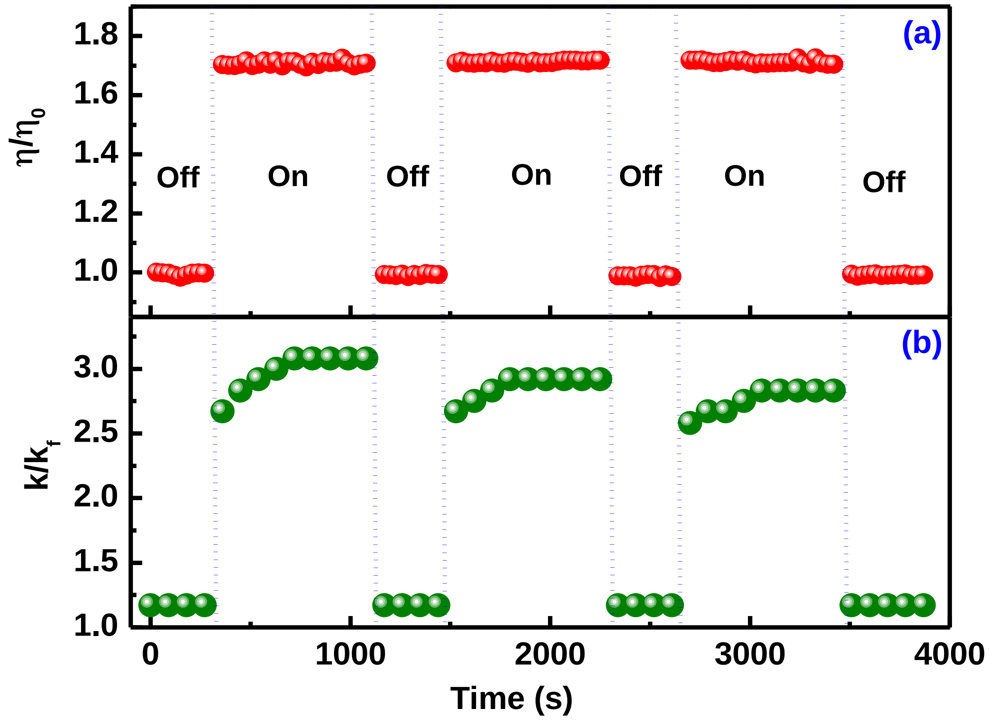

Fig. 5.16: The variation of (a): k/k_f and (b): η/η_0 with time for the switching on and switching off of a magnetic field strength of 120 Gauss for hexadecane based Fe_3O_4 nanofluid with $\phi = 0.067$ (shear rate =50 s^{-1}).

Though the equilibrium value of viscosity is achieved instantaneously, it is realized after ~ 400 seconds in the case of thermal conductivity. With increase in number of switching cycles, the equilibrium value is achieved faster. Upon turning off the magnetic field, both the k/k_f and η/η_0 values drops to zero immediately, showing the perfect reversibility of the observed phenomena and the interesting practical applications is this fluid in 'smart' devices.

The present study offer the unique possibility of tuning the ratio of k_{eff} /η_{eff} in magnetically controllable nanofluids making them superior to carbon nanotubes based suspensions in terms of reversible tunability for heat transport applications. Moreover, these magnetically controllable nanofluids can behave like a multifunctional "smart" material that can remove heat and also arrest vibrations (act as a damper) offering exciting applications in microfluidic devices.

5.5 Conclusions

In the present study, a new approach to tune the thermal properties of magnetic nanofluids from low to very high values is demonstrated by varying the magnetic field strength and its orientation. Moreover, the study reveals the unique possibility of tuning the ratio of k_{eff} /η_{eff} in magnetically controllable nanofluids making them superior to carbon nanotubes based suspensions in terms of reversible tunability for heat transport applications. Further, the present study unambiguously confirms that the microconvection is not the key mechanism responsible for thermal conductivity enhancements in nanofluids and the aggregation has a more prominent role.

A dramatic k enhancement is observed in a nanofluid containing magnetite particles under the influence of an applied magnetic field parallel to temperature gradient. The higher the volume fraction of magnetic nanoparticles, the larger is the observed k increment. The maximum enhancement in k observed is 300% for nanofluid with a particle loading of ϕ=0.063. The decrease in thermal conductivity observed above a critical magnetic field strength is due to 'zippering' of chains which is also confirmed by microscopy studies.

As the magnetic field strength is increased progressively, continuous conduction paths emerge along the nanoparticle chains that result in a series to parallel mode of conduction. k measurements under different magnetic field orientations with respect to the thermal gradient shows maximum k enhancement when the field direction is exactly parallel to the thermal gradient, irrespective of the applied magnetic field strength and ϕ of particles. No enhancement is observed when field was perpendicular to thermal gradient. A gradual reduction in the k enhancement is observed as the field direction was shifted from parallel to perpendicular direction with respect to thermal gradient.

As the nanoparticles starts to form aggregates of larger size or chains, the convection velocity drops drastically due to the cubic dependence on the particle size. Therefore, the Brownian motion is severely arrested as the chain length increases. As the convection velocity decreases with increasing magnetic field, the observed enhancement in k is cannot be due to the microconvection mechanism. The increase in k is attributed to the effective conduction of heat through the chainlike structure formed under magnetic field when the dipolar interaction energy becomes greater than the thermal energy.

The measurement of k in stable oil based magnetite nanofluids during rise and decay of magnetic field strength shows that the k enhancement is reversible with a small hysteresis. k enhancement is reversible even under repeated magnetic cycling. The observed reversible tunable thermal property of nanofluid may find many technological applications in NEMS and MEMs based devices. Reversible field induced η enhancement with a slight hysteresis is observed in stable oil based magnetite nanofluids during rise and decay of magnetic field strength. Such field induced enhancements in k and η of ferrofluids can be exploited for a number of technological applications such as damping cum cooling.

Chapter – VI

Study of Temperature Dependent Thermal Conductivity and Viscosity of Aqueous and Non-Aqueous Magnetite Nanofluids

Contents

Chapter VI

Study of Temperature Dependent Thermal Conductivity and Viscosity of Aqueous and Non-Aqueous Nanofluids

6.1 Introduction

Among various issues pertaining to heat transport in nanofluids, one of the area lacking consensus is the exact dependence of temperature on k of nanofluids.[35, 38, 49, 54, 61-63, 69, 72, 74, 87, 89-93, 96, 98-103, 108-111, 113, 115, 311-314] Some of the studies show an enhancement in k ratio (k/k_f) with temperature[38, 49, 54, 72, 74, 87, 89-93, 96, 98-103, 115, 311, 312] while others reports invariant k/k_f with rise in temperature.[35, 61-63, 69, 108-111, 113, 313] Also, a decrease in k/k_f with temperature is reported in some cases.[116] Contradictory temperature dependent k results are reported both for metal and metal oxide nanofluids even in the same base fluids.[35, 38, 49, 54, 61-63, 69, 72, 74, 87, 89-93, 96, 98-103, 108-111, 113, 115, 311-314] Most of the studies in water based alumina (Al_2O_3) nanofluids show an enhancement in k/k_f with temperature.[49, 54, 72, 74, 87, 89-93, 311] An enhancement in k/k_f with temperature is also reported in EG based Al_2O_3 nanofluids.[87] A few reports show temperature independent thermal conductivity for water, EG and hexadecane based Al_2O_3 nanofluids where the k of nanofluids simply follows that of the base fluids.[61, 69, 110, 313] An enhancement in k/k_f[54, 74, 93] and a constant[110] k/k_f ratio are reported in water based CuO nanofluids with increase in temperature. Similarly, both an enhancement[115] and a constant[110] k/k_f with increase in temperature is reported for water based titania (TiO_2) nanofluids. Among other metal oxide nanofluid studied, kerosene and transformer oil based Fe_3O_4 nanofluids showed least temperature effect on k.[108, 111] Studies in metal nanofluids show an increase in k/k_f with temperature for kerosene[312] and water[38] based Ag nanofluids. Toluene based gold (Au) nanofluids also show an increase in k/k_f with temperature.[38] However, a constant k/k_f was reported for Au in toluene and Au in water nanofluids with increase in temperature.[62, 110] Studies show enhancement in k/k_f with temperature for water and EG based carbon nanotube (CNT) nanofluids.[100-103] Multi Walled CNTs (MWCNTs) dispersed in EG showed a temperature independent k/k_f.[113] Among the other nanofluids studied, TiO_2 nanotubes in water, diamond nanoparticles in water, aluminum (Al) nanoparticles in engine oil, amorphous carbonic nanoparticles in water and tin oxide (SnO_2) nanoparticles in water have shown enhancement in k/k_f with temperature.[87, 90, 96, 98, 99] However, for silicon carbide (SiC) in water, zinc oxide (ZnO) in EG, graphene oxide nanosheets dispersed in water, EG, propyl glycol and liquid paraffin, the k/k_f was found to be independent of temperature.[35, 63, 109] Interestingly barium titnate (Bi_2Te_3) nanorods exhibits a decrease in k/k_f with increase in temperature in both perfluron-heaxane and hexadecane based fluids.[116] These conflicting reports warrant a systematic study on temperature dependent k in stable aqueous and non-aqueous nanofluids. This is the main motivations behind the present study.

Another important and intriguing question that remained unanswered in the domain of thermal properties of nanofluids is the effect of temperature on nanoparticle clustering and viscosity. DLS and η measurements are the two widely accepted tools to probe effect of aggregation in nanofluids.[58, 62, 63, 128, 136, 147, 148, 150-152, 155-160, 275] The purpose of this systematic study is to obtain insight into the exact dependence of temperature on k, particle agglomeration, and η in well tailored ‘stable’ nanofluids.

6.2 Effect of Temperature on Thermal Conductivity of Nanofluids

Stable oil based nanofluids for the present study is prepared by dispersing oleic acid coated magnetite nanoparticles in kerosene and hexadecane. TMAOH coated magnetite nanoparticles are used for preparation of stable water based nanofluids. Figures 6.1 show the variation of k as a function of temperature for kerosene based Fe_3O_4 nanofluids.

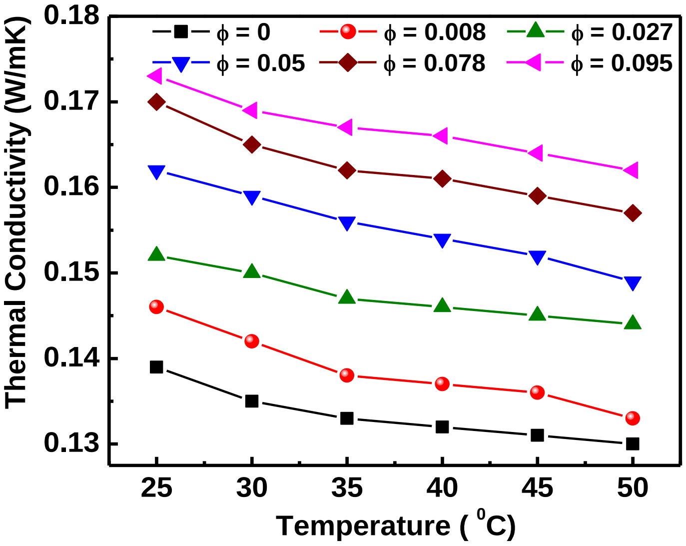

Fig. 6.1: The variation of thermal conductivity with temperature for kerosene based Fe_3O_4 nanofluids with ϕ= 0, 0.008, 0.027, 0.05, 0.078 and 0.095.

Here, the base fluid k includes the surfactant contribution. k experiments are performed with base fluid alone and with the exact amount of surfactant that is adsorbed onto the nanoparticles. In order to take into consideration of the contribution of surfactant present in the base fluid k, the surfactant and base fluid k is used as k_f. Present experiments show no observable changes in the k values upon the addition of surfactant. The ϕ equal to zero corresponds to the base fluid k (i.e., k_f). Over the temperature range of 25 to 50 °C, the absolute k of kerosene based nanofluids and the base fluid decreases with the increase in temperature. A similar trend of decrease in k with the increase in temperature is observed in kerosene-based silver nanofluids.[312] Interestingly, k/k$_f$ (Fig. 6.2) remains constant with an increase in temperature for kerosene based nanofluids.

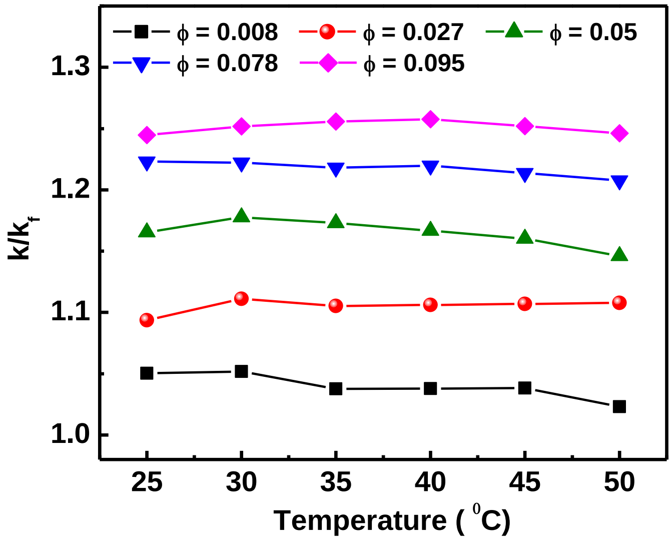

Fig. 6.2: The variation of thermal conductivity ratio with temperature for kerosene based Fe_3O_4 nanofluids with ϕ= 0.008, 0.027, 0.05, 0.078 and 0.095.

Figures 6.3 (a) and (b) shows the variation of k and its ratio as a function of temperature for hexadecane based Fe_3O_4 nanofluids. Over the 25 to 50 °C, the k of hexadecane based nanofluids decreases with the increase in temperature [Fig. 6.3(a)]. But, again the k/k$_f$ remains invariant with the rise in temperature [Fig. 6.3(b)]. Figures 6.4 (a) and (b) shows the variation of k and its ratio as a function of temperature for water based Fe_3O_4 nanofluids. Over 25 to 50 °C, the k of water based nanofluids increases with increase in temperature [Fig. 6.4(a)]. Such an increase in k with temperature was reported earlier in water based nanofluids.[92, 101, 114] Interestingly, the thermal conductivity ratio remains invariant with the rise in temperature for water based nanofluids [Fig. 6.4(b)].

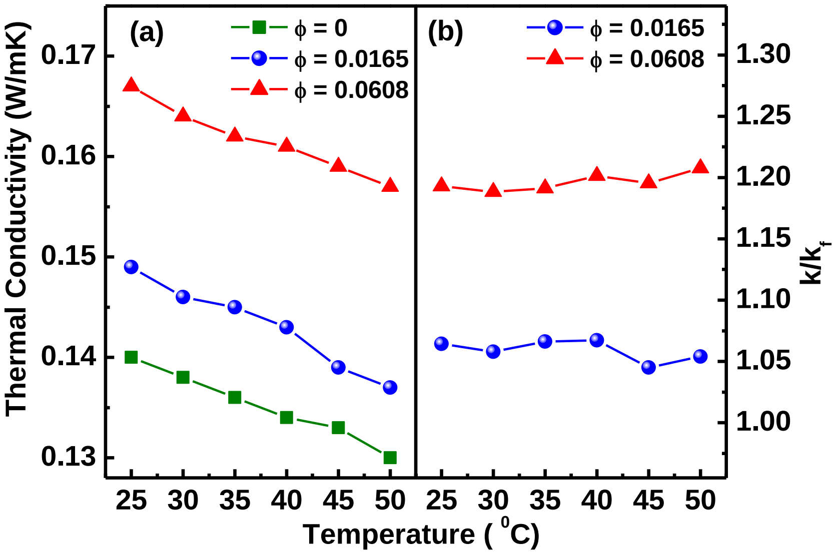

Fig. 6.3 (a): The variation of thermal conductivity with temperature for hexadecane based Fe_3O_4 nanofluids with ϕ=0, 0.0165 and 0.0608. (b): The variation of thermal conductivity ratio with temperature for the above nanofluids.

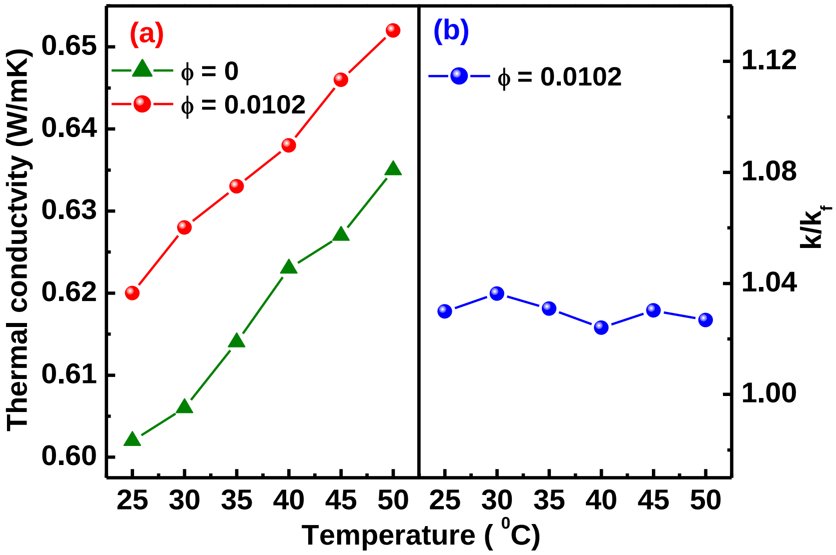

Fig. 6.4 (a): The variation of thermal conductivity with temperature for water based Fe_3O_4 nanofluids with ϕ=0.0102 (b): The variation of thermal conductivity ratio with temperature for the above nanofluids.

Why does the temperature-dependent k show a different trend in water and oil-based nanofluids? The relationship for the k in terms of fundamental properties of the liquid is $k=2R\upsilon\Delta^{-2}$ where R is the gas constant, υ is the velocity of sound in the liquid and Δ is the mean distance of separation of the centers of the molecules.[315] The conductivity of water is three to four times as high as that of the ordinary organic liquids because of its low compressibility and the fact that the centers of the molecules in water are closer together than in the ordinary liquid. The above formula gives the right sign for the temperature coefficient of conductivity at atmospheric pressure, both for ordinary liquids and water. For the ordinary liquid, both υ and Δ^{-2} decrease with rising temperature, so that the conductivity is expected to decrease with rising temperature, as it actually does, whereas for water υ increases with rising temperature (both the isothermal compressibility and the thermal expansion of water vary abnormally with temperature) at a rate more than that is sufficient to compensate for the decrease of Δ^{-2}, so that on the whole the conductivity should increase. This perhaps explains the different trend in temperature dependence observed between aqueous and nonaqueous nanofluids.

These results suggest that the k of the nanofluids simply track the k of the base fluid. A similar k variation with increase in temperature was reported for both water and oil based nanofluids.[35, 61-63, 108, 109, 111, 113, 313] Many studies show an increase in k/k_f with temperature for aqueous and nonaqueous nanofluids.[38, 49, 54, 72, 74, 87, 89-93, 96, 98-103, 115, 311, 312] By taking into consideration the interfacial thermal resistance and the mixing of convection currents from multiple nanoparticles, the ratio k/k_f according to microconvection model is[316]

$$\frac{k}{k_f} = \left(1 + Z\,\mathrm{Re}^{\omega}\,\mathrm{Pr}^{0.333}\,\phi\right)\left(\frac{1+2\beta\phi}{1-\beta\phi}\right) \qquad (6.1)$$

where ω is a system-specific exponent. For aqueous suspensions, ω is found to have an optimal value of 2.5, Z is constant with values as large as 4×10^4, Re is the Reynolds number of the particle and Pr the Prandlt number of the base fluid. The hypothesized microconvection effects appear through Re = v_N d/η, where v_N is the convection velocity, η is the viscosity and d is the particle size. In the microconvection model, the convection velocity is taken to be the root-mean-square velocity (v_N) of the nanoparticle, defined as

$$\upsilon_N = \sqrt{\frac{18k_B T}{\pi\rho d^3}} \qquad (6.2)$$

Where k_B is the Boltzmann constant, T the temperature, ρ the density of particles, and d size of nanoparticle. The k/k_f results observed in our experiments is contrary to the semi-empherical convective model predictions,[316] but the results are in good agreement with the traditional Maxwell-Garnett model for composites.[317]

Figure 6.5 shows the variation of k ratio with volume fraction at three different temperatures (25, 40 and 50 °C) for kerosene based Fe_3O_4 nanofluids. Maxwell fit is shown by the black doted lines. The k increases linearly and the data fit well with Maxwell model. According to kinetic theory, the enhancement in *k* due to the Brownian movement of the particles is $\phi C_N v_N l_N/3$, where C_N is the heat capacity per unit volume of the nanoparticles, v_N root-mean-square velocity of Brownian particle and l_N is the mean free path.

As nanoparticles start to form aggregates of larger size or chains, the convection velocity v_N drops drastically due to the cube dependence of particle size and increases linearly with square root of T and hence the k is also expected to increase in the same manner irrespective of the fluid used. The present observation is in sharp contrast to the microconvection theory predictions of an increase in thermal conductivity with a rise in temperature. These results once again reaffirm that microconvection has a less prominent role on thermal conductivity enhancement of nanofluids.

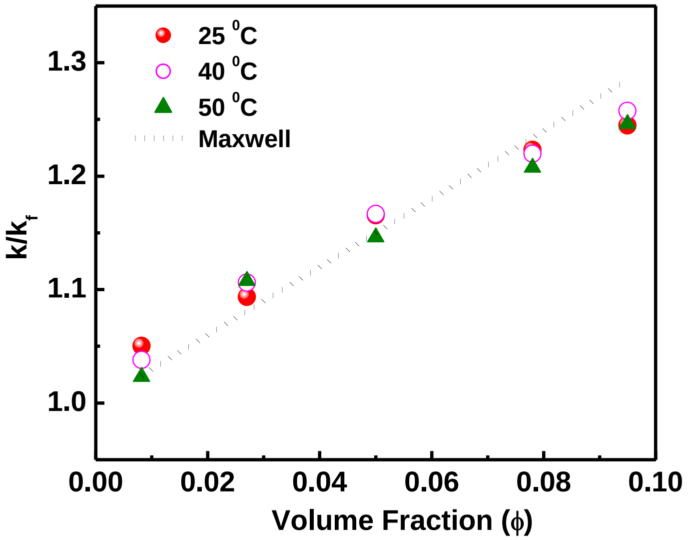

Fig. 6.5: The variation of thermal conductivity ratio with volume fraction at three different temperatures (25, 40, and 50 °C) for kerosene based Fe_3O_4 nanofluids. The Maxwell fit is shown by the dotted line.

According to microconvection models,[142] the time required for a Brownian particle to travel its diameter t_B, is $3\pi\eta d^3/2k_BT$, where η is the viscosity of base fluid, d is the nanoparticle size, T is the temperature and k_B the Boltzmann constant. Their study with dye diffusion shows that Brownian motion of the particles does not contribute directly to the mass transport enhancement but it enhances the convection currents due to increase in the nanoscale stirring of the liquid. The Brownian models assume that the nanofluid k is directly dependent on the self diffusion coefficient of nanoparticles. If micro-convection contributes to the enhanced k, the k/k_f ratio would have increased with increase in temperature. A constant ratio of k/k_f, observed in the present experiments indicates a less important role of microconvection of k enhancement. By a simple analysis Keblinski et al[140] have proved that thermal diffusion is much faster than nanoparticle Brownian motion; thus the movement of nanoparticles has a negligible effect on the effective k of the suspension. Molecular dynamics simulations in a model nanofluid have shown that Brownian motion of the particle does not affect the cooling process.[318] Kinetic theory based analysis of heat flow in nanofluids demonstrates that the hydrodynamics effects associated with Brownian motion have only a minor effect on the k of the nanofluid.[319] Moreover estimation of the k enhancement in nanofluids as a function of temperature from thermal diffusivity measurements on the nanofluids and base fluids at temperatures in the range of 25–75°C have shown that the k enhancement is independent of temperature.[65]

The observed temperature independent k in the present study is consistent with effective medium theory (EMT). EMT is applicable to statistically homogeneous and low volume fraction liquid–solid suspensions with randomly dispersed and uniformly sized spherical particles. According to EMT, the effective k of nanofluids relies on the k of the spherical particle, the base fluid and the volume fraction of the solid particles. No temperature dependence of the k enhancement is considered by this model.

6.3 Effect of Temperature on Particle Size Distribution of Nanofluids

Figure 6.6 shows effect of temperature on average particle size of kerosene based nanofluid at different volume fractions of 0.00819, 0.027, 0.05, 0.078 and 0.095. The DLS measurements show no change in the size with rise in temperature (Inset of Fig 6.6), which indicates the absence of aggregation with temperature. Figure 6.7 shows the variation of average particle size with temperature for hexadecane based ferrofluids with $\phi = 0.0608$. Inset shows the number percentage vs. size for the above nanofluid at 25, 35 and 50 °C. The average particle size does not change with temperature for hexadecane based nanofluids also. Water based nanofluids (Fig. 6.8) also shows an invariant average particle size with temperature.

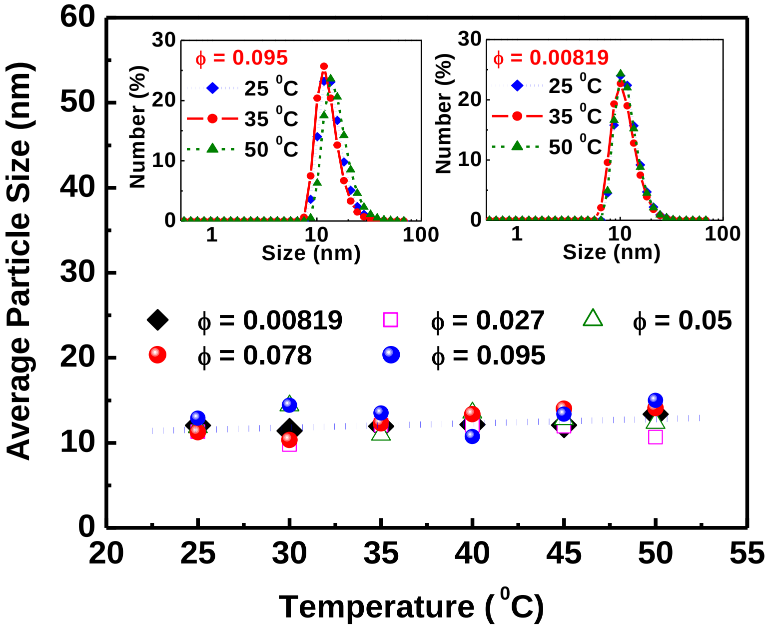

Fig. 6.6: The variation of average particle size with temperature for kerosene based Fe_3O_4 nanofluids with ϕ= 0.00819, 0.027, 0.05, 0.078, and 0.095. Inset shows the number percentage vs size for nanofluids with ϕ=0.00819 and 0.095 at 25, 35, and 50 °C.

The aggregation time constant is given as $t_p= (\pi\eta r^3W)/(k_BT\phi)$, where W is the stability ratio, r is the particle radius; ϕ is the volume fraction. For a stable system, t_p tends to infinity.[142] The stability ratio is assumed to be unity in the absence of a repulsive force and hydrodynamic interactions between the nanoparticles and it is greater than one in the presence of a repulsive forces. According to the above equation, aggregation time constant decreases with decrease in nanoparticle size and with increase in temperature.

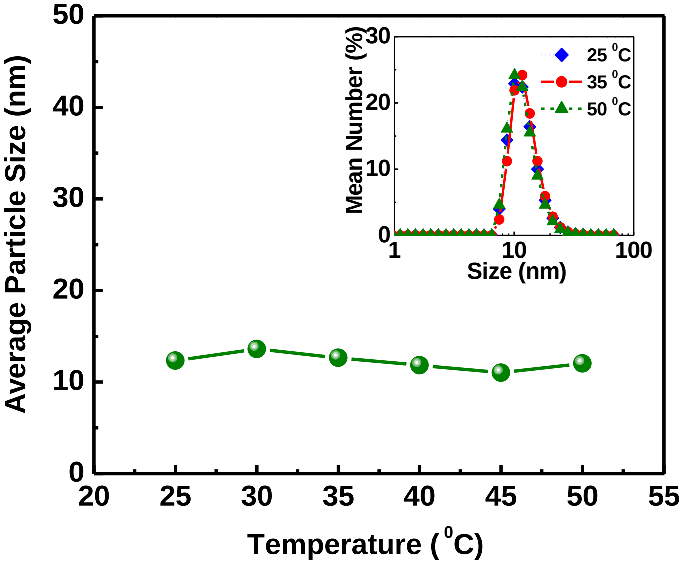

Fig. 6.7: The variation of average particle size with temperature for hexadecane based Fe_3O_4 nanofluids having ϕ=0.0608. Inset shows the number percentage vs size for the above nanofluid at 25, 35, and 50 °C.

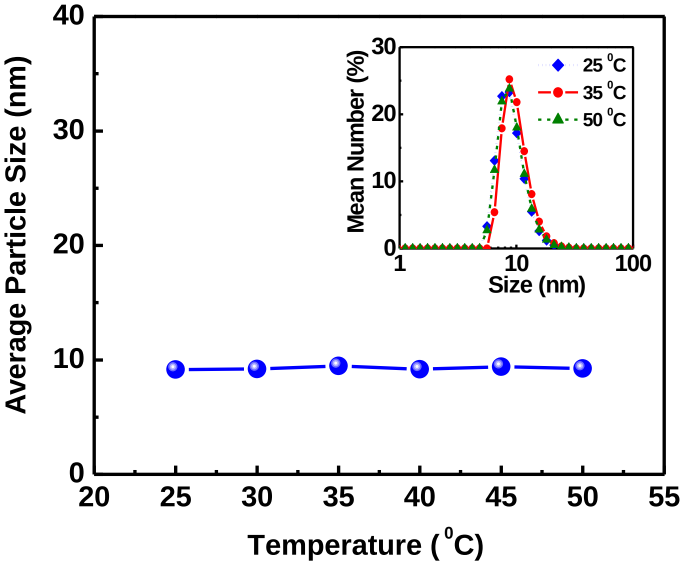

Fig. 6.8: The variation of average particle size with temperature for water based Fe_3O_4 nanofluids having ϕ=0.0102. Inset shows the number percentage vs size for the above nanofluid at 25, 35, and 50 °C.

With increasing temperature, Brownian motion increases and so aggregation time constant decreases, leading to a higher probability for particles to aggregate. Interestingly DLS studies show no sign of aggregation with temperature in our samples. This is also independently confirmed from static light scattering studies.[320]

The present results show that the aggregation is essentially governed by surface chemistry of the nanoparticles and the stabilizing moieties used. Proper steric stabilization with a high potential barrier ($>10k_BT$) prevents the particles crossing the barrier. Further, the presence of surfactant monolayer leads to complete wetting of the particle by the liquid medium, which has a major role on the interfacial resistance. In such stable nanofluids, the aggregation is negligible at higher temperatures.

6.4 Effect of Temperature on Viscosity of Nanofluids

Figures 6.9 and 6.10 show the variation in η of kerosene based Fe_3O_4 nanofluids and its ratio (with respect to base fluid) respectively for three different volume fractions of nanoparticles. Although the absolute η decreases with increase in temperature in both the base fluids and the nanofluids, the η ratio remains almost constant with increase in temperature, which is a clear indication for the absence of aggregation with temperature. A similar viscosity behavior with temperature was reported for other nanofluids also.[63, 113, 144, 146] A constant viscosity ratio is also observed with increase in temperature in water and hexadecane based Fe_3O_4 nanofluids in our study.

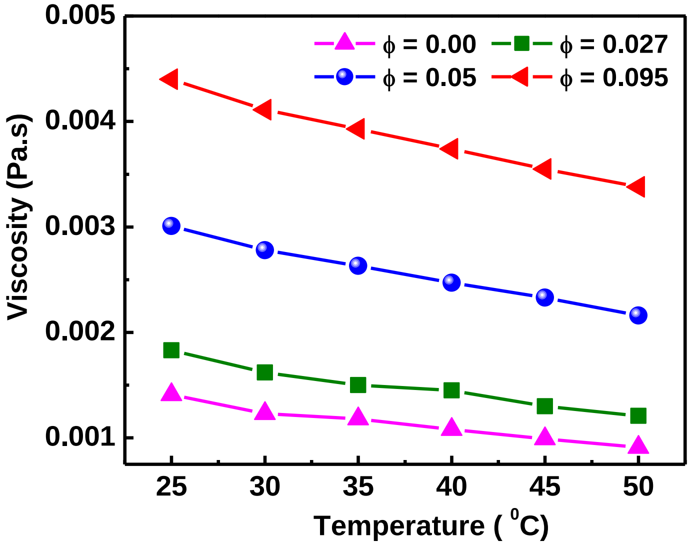

Fig. 6.9: The variation of viscosity with temperature for kerosene based Fe_3O_4 nanofluids having ϕ=0, 0.027, 0.05, and 0.095.

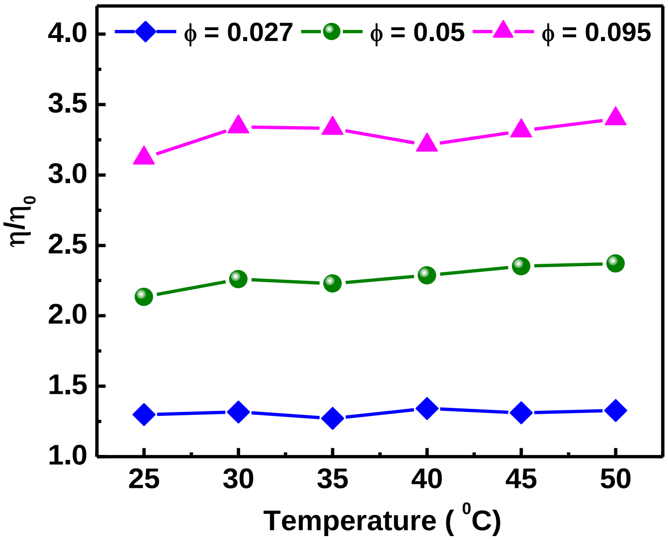

Fig. 6.10: The variation of viscosity ratio with temperature for kerosene based Fe_3O_4 nanofluids with ϕ=0.027, 0.05, and 0.095.

Almost all the exiting theoretical formulas which are used for the determination of particle suspension viscosity was derived from Einstein analysis of infinitely dilute suspensions of hard spheres.[321] In Einstein model, the particles are assumed to be rigid, uncharged and without attractive forces; they are small enough so that the dilatational perturbation of the flow is unbounded and is able to decay to zero. A particle moves at the velocity of the streamline with the particle centre in such a suspension. Einstein equation describes the dependence of viscosity increase with concentration of particles in the simplest case of dilute suspensions ($\phi \leq 0.01$) as

$$\frac{\eta}{\eta_0} = 1 + 2.5\phi \tag{6.3}$$

Where, η is the nanofluid viscosity and η_0 the base fluid viscosity.

When $\phi \geq 0.01$, hydrodynamic interactions between particles become important as the disturbance of the fluid around one particle interacts with that around other particles. The viscosity in such a case is given by Batchelor equation[322]

$$\frac{\eta}{\eta_0} = 1 + 2.5\phi + 6.5\phi^2 \tag{6.4}$$

For $\phi \geq 0.1$, where multi-particle collisions become increasingly important, a semi-empirical relationship for the shear viscosity covering the full range of particle volume fraction was obtained by Krieger and Dougherty.[323]

$$\frac{\eta}{\eta_0} = \left(1 - \frac{\phi}{\phi_m}\right)^{-[\eta]\phi_m} \tag{6.5}$$

where, [η] is the intrinsic viscosity, which is 2.5 for hard spheres and ϕ_m is the maximum packing fraction. For randomly mono-dispersed spheres, the maximum close packing fraction is approximately 0.64. Figure 6.11 shows variation of viscosity ratio with volume fraction for kerosene based ferrofluids together with Einstein and Krieger-Dougherty (KD) fit.

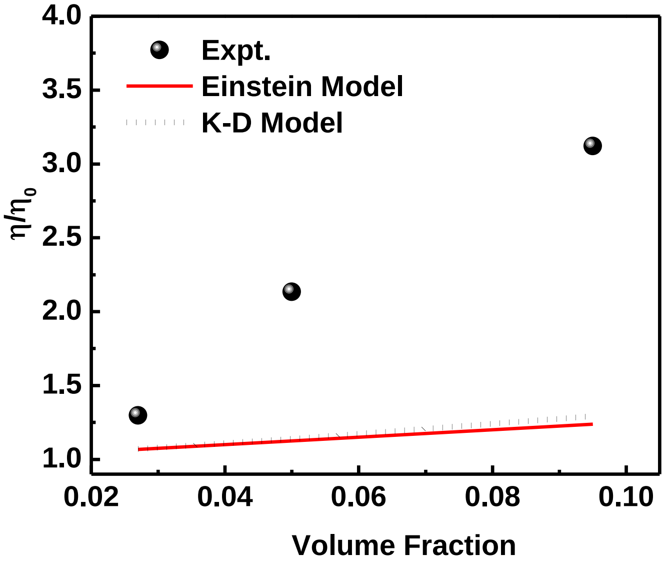

Fig. 6.11: The variation of viscosity ratio with volume fraction for kerosene based Fe_3O_4 nanofluids at 25 °C together with the Einstein and Krieger-Dougherty (KD) fit.

The results show that the enhancement in viscosity ratio with ϕ is much more than the values predicted by Einstein and K-D models. Some of the studies show a moderate viscosity enhancement[63, 87, 115, 143-145, 160] while others reports a very high viscosity enhancement[98, 147, 153, 161, 163] in nanofluids compared to Einstein model.

Functional dependence of the viscosity on the fluid temperature can be expressed by Arrhenius-type equation.[324]

$$\eta = \eta_{\infty T} e^{E_a/RT} \tag{6.6}$$

where η is the viscosity from experimental tests, $\eta_{\infty T}$ is the viscosity at infinite temperature, E_a is the activation energy to fluid flow, R is the universal gas constant, and T is the temperature in Kelvin. The activation energy and infinite temperature viscosity are parameters that reflect the behavior of fluids and can be extracted from experimental data through the logarithmic form of the Arrhenius equation.

We have also measured the viscosity of the nanofluid as a function of the shear rate (10–1000 s^{-1}) at different temperatures. Figures 6.12 and 6.13 shows variation of viscosity with shear rate at different temperatures for kerosene based Fe_3O_4 nanofluids with ϕ=0 (base fluid), ϕ = 0.027, ϕ = 0.050 and ϕ =0.095.

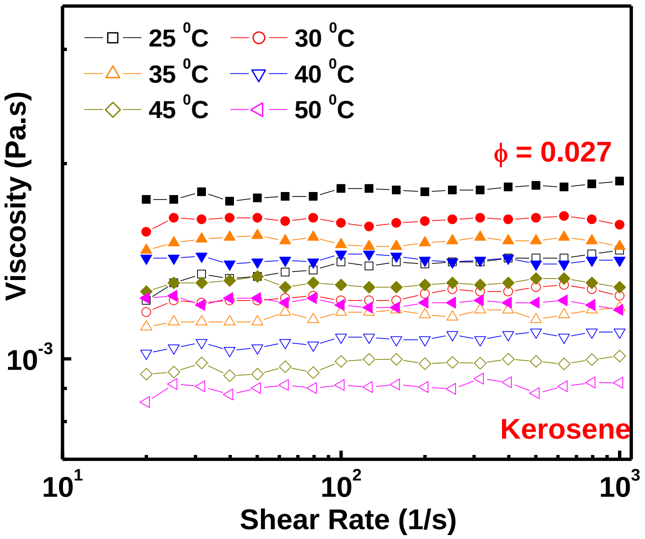

Fig. 6.12: The variation of viscosity with shear rate at different temperatures for kerosene and kerosene based Fe_3O_4 nanofluids with ϕ= 0.027.

Our results show that the viscosity is independent of shear rate from 25 to 50 °C, indicating that the nanofluids are stable and possess Newtonian nature. Such Newtonian nature of viscosity was reported for both metal and metal oxide based nanofluids.

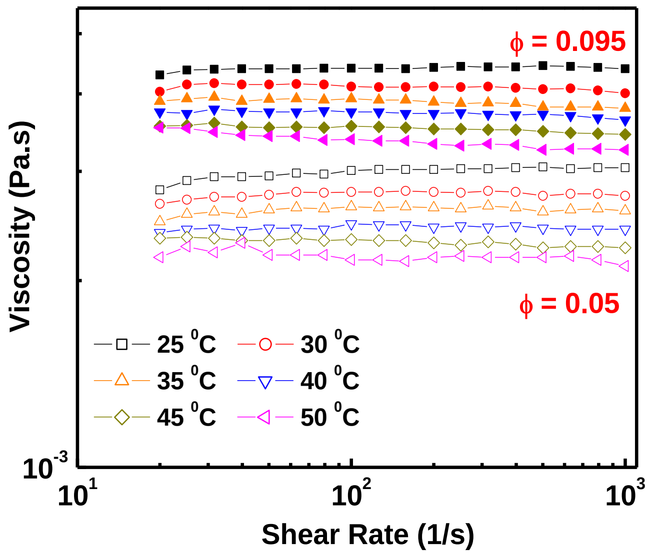

Fig. 6.13: The variation of viscosity with shear rate at different temperature for kerosene based Fe_3O_4 nanofluids with ϕ= 0.05 and ϕ=0.095.

Figure 6.14 shows the variation of viscosity with shear rate at different temperatures for hexadecane and hexadecane based Fe_3O_4 nanofluids with ϕ =0 (base fluid) and ϕ=0.0608. The viscosity did not appreciably vary, indicating Newtonian behavior, over the shear rate and temperature studied.

The effectiveness of nanofluid coolants depend on the flow mode (laminar or turbulent), that can be estimated based on fluid dynamics equations. Lower viscosity implies lower pumping power that is advantageous from an industrial application point of view. A quantitative expression derived for fully developed laminar flow that compares the relative coefficients of viscosity and k enhancement shows that the use of nanofluid will be beneficial if the increase in the viscosity is less than four times of the increase in k.[144]

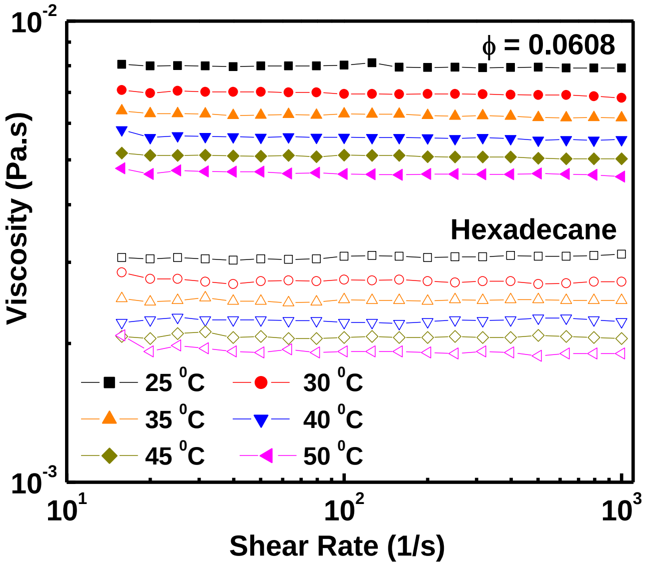

Fig. 6.14: The variation of viscosity with shear rate at different temperatures for hexadecane and hexadecane based Fe_3O_4 nanofluids with $\phi=0.0608$.

Viscosity and thermal conductivity enhancements can be described by linear dependence on the particle volume fraction in our studies.

$$\frac{k}{k_f} = 1 + C_k\phi \tag{6.7}$$

$$\frac{\eta}{\eta_0} = 1 + C_\eta\phi \tag{6.8}$$

where C_k and C_η are constants. At low volume fractions, for the nanofluid to be beneficial, the ratio of coefficients (C_η/C_k) should be < 4.[144] The value of C_k and C_η was found to be 3 and 11 respectively for kerosene based nanofluid with $\phi = 0.027$ at 25 °C in our study. Thus the calculated C_k/C_η ratio of 3.6 is within the expected regime for efficient nanofluid. The above value was lower than the ratio reported for SiC and Al_2O_3 nanofluids.[63] However, C_k/ C_η was found to be 7.3 and 7.8 for kerosene based nanofluids with $\phi = 0.05$ and 0.095 respectively in our study, implying that either viscosity needs to be reduced or conversely the k at the same particle loading has to be improved further for practical applications.

6.5 Conclusions

The k of aqueous nanofluids increases with temperature while it shows a decrease in nonaqueous nanofluids. The ratio of thermal conductivity of both nanofluids with respect to base fluids (k/k_f) remains constant with an increase in temperature, irrespective of the nature of the base fluid. These results suggest that the k of the nanofluids simply track the k of the base fluid and the enhancement in nanofluids relative to base fluids is essentially temperature independent. This observation is in sharp contrast to microconvection theory predictions of an increase in k with a rise in temperature. These results unambiguously confirm the less dominant role of microconvection on k enhancement.

Although the absolute η decreases with an increase in temperature in both the base fluids and the nanofluids, the viscosity ratio remains almost constant with an increase in temperature, which is a clear indication of the absence of aggregation of particles with temperature. The results confirm that nanofluid simply track temperature depend viscosity behavior of base fluid and observed variation in η with increasing temperature comes from the base fluid rather than from behavior associated with the nanoparticles. DLS studies show no aggregation of particles with temperature in stable water and oil based nanofluids.

The present results show that the aggregation is essentially governed by surface chemistry of the nanoparticles and the stabilizing moieties used. Nanoparticle aggregation is insignificant with the increase in temperature in properly functionalized nanofluids. Such nanofluids are ideal for practical applications because of their long-term stability.

Chapter – VII

Effect of Particle Size on Thermal Conductivity and Viscosity of Magnetite Nanofluids

Contents

Chapter VII

Effect of Particle Size on Thermal Conductivity and Viscosity of Magnetite Nanofluids

7.1 Introduction

The exact role of nanoparticle size on k enhancement has been a hotly pursued topic. Literature data on the effect of particle size on the k of nanofluids are limited and controversial. Many experimental and theoretical studies show an increase in k with decrease in particle size.[49, 51, 53, 72-76, 319, 325, 326] However, there are also few reports on enhanced nanofluid k with increasing particle size.[62, 63, 69, 70, 81-84, 327-329]

Many studies have reported monotonic increases in the k with decreasing particle size, attributed to enhanced Brownian motion.[49, 51, 53, 72-76, 319, 325, 326] A recent study in water based Al_2O_3 nanofluids with three different nominal diameters of 20, 50 and 100 nm shows an enhancement in k/k_f with decrease in nanoparticle size.[72] Another report also showed an increase in k with decrease in nanoparticle size in Al_2O_3 nanofluids.[73] Under the influence of increased temperature, for the same particle loading, Al_2O_3 nanofluid with small particle size yielded greater k values.[74] For water based Al_2O_3 nanofluids with two different particle size of 45 and 150 nm, larger k enhancement is observed for the nanofluid with smaller particle size.[75] Zinc oxide (29 and 77 nm) dispersed in 60:40 ratio of EG and water exhibited higher k ratio for smaller size nanoparticles.[76] Water and EG based Al_2Cu and Ag_2Al nanofluids also showed an enhancement in k/k_f with decrease in particle size.[51] In yet another report, water based Al_2O_3 nanofluids with nanoparticle diameters of 36 and 47 nm showed a higher thermal conductivity enhancement for the former than the latter for different volume fraction and temperatures.[53] The thermal conductivity studies in Al_2O_3 nanofluids as a function of nanoparticle size (ranging from 11 nm to 150 nm nominal diameters) over a wide range of temperature (from 21 to 71 °C) showed a k enhancement with decrease in nanoparticle size.[49]

However, a very recent report on k of water based SiC nanofluids with four different nominal diameters of 16, 29, 66 and 90 nm show higher k in larger particles.[81] Water based gold nanofluids also exhibit a decrease in k with decrease in particle size in the range of 2–40 nm.[62] k enhancement in aqueous Al_2O_3 nanofluids at room temperature was found to decrease as the particle size decreased below about 50 nm.[82] Water based ceria (CeO_2) nanofluids also showed an increase in k/k_f with increase in nanoparticle size.[84] For water and EG based Al_2O_3 nanofluids with seven different particle sizes ranging from 8–282 nm, the k enhancement decreases as the particle size decreased below about 50 nm.[83] An enhancement in k with increasing particles size is reported for SiC nanofluids.[63, 70, 328] Water based silica (SiO_2) nanofluids also showed an enhancement in k with increase in nanoparticle size.[329] The limiting value of the enhancement in nanofluids containing large particles was described well by the volume fraction (ϕ) weighted geometric mean of the bulk thermal conductivities of solid and liquid[313] or predictions of the effective medium theory[119, 330] corrected for particle shape by Hamilton and Crosser[331] and for the interface contribution.[332]

Regarding nanofluid η, the lack of consistent data on particle size effect in the literature is even more striking. Inconsistency of data is due to multiple factors affecting the viscosity of suspensions. Firstly, the formation of a diffuse layer of fluid at the particle/liquid interface increases the effective particle size and thus the effective volume concentration.[333, 334] Secondly, the interaction between the particles is also important because it determines particle agglomeration and degrees of freedom of motion in nanofluids. As particle size decreases, the total area of the solid/liquid interface and the number of particles at the same particle volume concentration increases. Therefore both the first and second effects become more important for smaller particle sizes, causing the larger increase in η.[334] A larger η increase for nanometer sized particles compared to micron sized particles was observed earlier.[335, 336] For water based SiC nanofluids, smaller particles showed higher η increase than larger particles of the same particle loading.[81] In a study to investigate the particle size effect on the η of water based Al_2O_3 nanofluid with two different nominal diameters of 36 and 47 nm, it was observed that for volume fractions > 4%, viscosities for the 47 nm particle size are clearly higher than those for the 36 nm particle size.[337] For water based SiO_2 nanofluids, with different particle sizes from 9–94 nm, the η was higher for nanofluids of smaller particle size.[147]

As discussed earlier, the size dependant thermal property studies have been carried out in nanofluids of few particle sizes and with relatively large size (> 20 nm), where the sedimentation is a major cause of concern. To obtain a better insight into the effect particle size on k enhancement, especially in very small particle size range (< 10 nm), the present study investigate the size dependant k in model nanofluids with long term stability. Moreover, effect of particle size on η enhancement is a prerequisite for fundamental and practical applications of nanofluids in thermal engineering.

7.2 Effect of Particle Size on Thermal Conductivity of Nanofluids

The thermal conductivity is measured at two different particle loadings of ϕ=0.01 and ϕ=0.055 as a function of particle size for kerosene based Fe_3O_4 nanofluids. Fig. 7.1 shows the thermal conductivity ratio (k/k_f) and % of k enhancement as a function of particle size. With a particle loading of ϕ=0.01, no enhancement in k is observed for nanofluid. For nanofluid with ϕ=0.055, the enhancement was about 5 and 25%, respectively, for 2.8 and 9.5 nm. The observation of increase in k with increase in particle size is in contrast with the earlier reports.[49, 51, 53, 72-76, 319, 325, 326] However, similar increase in k/k_f with particle size is recently reported in many nanofluids nanofluids.[62, 63, 69, 70, 81-84, 327-329] Molecular dynamics simulations based on the Stilling–Weber potential model silicon nanoparticles of diameter 2–12 nm predicts linear increase in thermal conductivity with particle size.[327] Such increase is attributed to the increase in phonon mean free path.

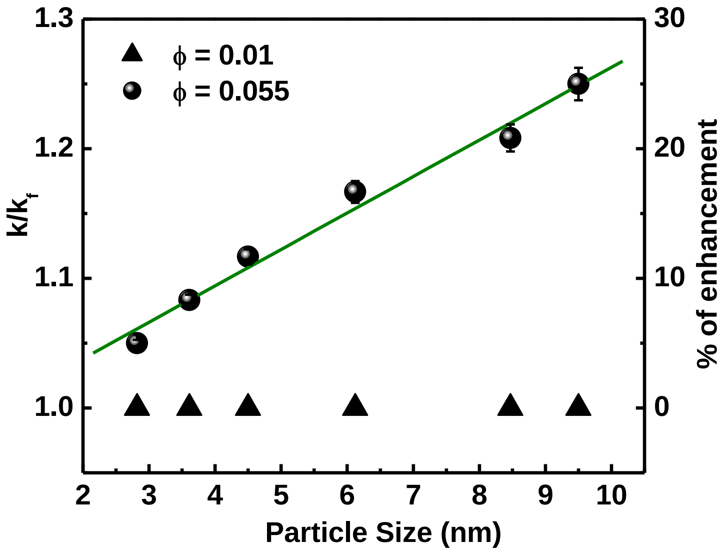

Fig. 7.1: The k/k_f and the % of k enhancement of magnetite nanofluids having two different volume fractions ϕ=0.01 and ϕ=0.055 as a function of nanoparticles size. Best fit is shown by the solid line.

The surface area of the solid/liquid interface increases geometrically as the average particle size in the nanofluids decreases. It is known[338] that interfaces act as an obstacle to heat flow, and the measure of interactions between the surface of the nanoparticles and the fluid are manifested through the interfacial thermal resistance, also known as the Kapitza resistance (R_b). In a recent study on SiC nanofluids, higher k observed for nanofluids with larger particles, was attributed to the effect of nanoparticle surface area.[81] We believe that the observed increase may be originating from the kinetic growth of small particles into fractal like aggregated in the suspensions where the process can be diffusion or reaction limited.[339]

According to microconvection model, the local convection is caused by the Brownian motion of the nanoparticles in base fluid. The Reynolds number (Re) for Brownian motion is inversely proportional to square root of the particle size. Therefore, an increase in thermal conductivity with decrease in particle size is predicted by microconvection model. However, the observed results are contrary to the above predictions. The present findings confirm that microconvection is not the key mechanism responsible for k enhancements in nanofluids and the aggregation has a more prominent role.

The effect of particle size on field induced thermal conductivity enhancements in kerosene based Fe_3O_4 nanofluids is also investigated in the present study. The k measurements are done on nanofluids with different particle size, ranging from 2.8 to 9.5 nm at a fixed concentration of $\phi = 0.04$ (Fig. 7.2). The results show that for nanofluid with particle size = 2.8 nm, there is hardly no change in k with external magnetic field strength. With the increase in nanoparticle size, the field induced k enhancement also increased. The nanofluid with largest particle size (9.5 nm) is found to exhibits largest k enhancement. For a magnetic field strength of 330G, the k enhancement was 16 and 240% for a nanofluid with particle size 2.8 and 9.5 nm respectively at the same particle loading of $\phi = 0.04$.

Here, the iron oxide particles are superparamagnetic in nature and the magnetization variation as a function of magnetic field can be described by Langevin's equation

$$\frac{M}{M_S} = L(\zeta) = \coth(\zeta) - 1/\zeta \tag{7.1}$$

Where M is the sample magnetization, M_S the saturation magnetization, $\zeta = \mu_0 mH/(k_B T)$ is the Langevin function, with $\mu_0 = 4\pi \times 10{-}7$ J A^{-2} m^{-1}, 'm' is the magnetic moment, k_B is the Boltzmann constant, T is the temperature and H is the magnetic field strength.

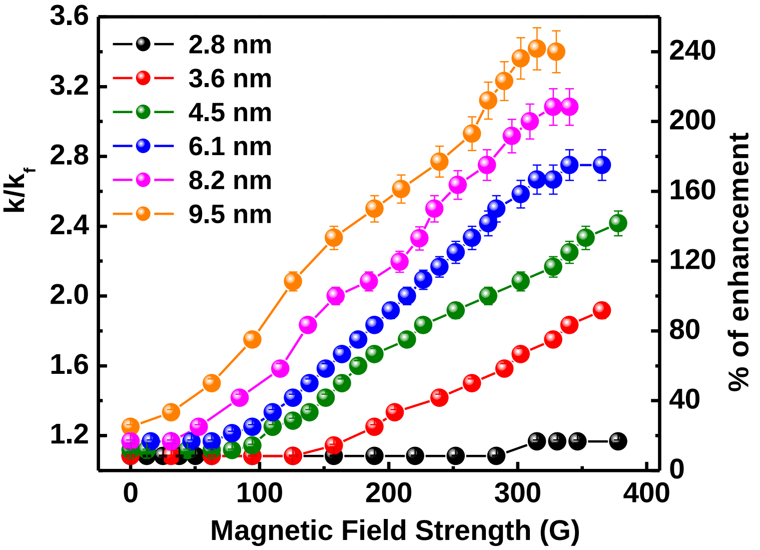

Fig. 7.2: The k/k_f as a function of magnetic field strength for kerosene based Fe_3O_4 nanofluids having different particle sizes at $\phi = 0.04$, where the applied field is parallel to the temperature gradient.

In the low-field limit, the Langevin magnetic susceptibility $\chi_L = M/H$ is linear with the particle number density N, $\chi_L = \frac{\mu_0 N m^2}{3 k_B T} = 8L\phi$ where ϕ is the particle volume fraction, defined as the total volume of particles, including the oleic acid layer, divided by the sample volume and L is the magnetic coupling constant.[340]

The ferrofluid microstructure is very sensitive to particle size and the dipole–dipole interactions that can be tuned by varying the particle size.[341] The magnetic dipole moment (m) of a single-domain sphere of radius ‘r’ and saturation magnetization M_S is $m = 4\pi r^3 M_S / 3$.[342] The dipole–dipole interaction between two magnetic particles at contact, scales as $m^2/\sigma^3 \propto r^6/\sigma^3$, where σ is the hard core diameter of the particle. The magnetic dipole interaction energy of particles with size below 13 nm is less than their thermal energy, and thus such particles cannot form permanent structures.[282] The increase in k/k_f with particle size is attributed to enhanced dipolar interaction and aspect ratio of the chains.

7.3 Effect of Particle Size on Viscosity of Magnetite Nanofluids

Figure 7.3 show the variation of viscosity ratio (η/η_0) as a function of nanoparticles size for kerosene based magnetite nanofluids with ϕ=0.055. Nanofluids with smaller particles result in a higher η increase than larger particles. The η/η_0 is 3.09 and 1.59 respectively for nanofluids with 2.6 and 9.5 nm sized particles. Similar variation of nanofluids η with particle size is reported for silica,[147] silicon carbide[81] and alumina[337] nanofluids. The larger surface area of solid/liquid interfaces and increased effective volume of solids may be the reason for the observed trend. Moreover, the adsorbed oleic acid layer on nanoparticle surface can also contribute for the η enhancement. The amount of surfactant present in 2.6 and 9.5 nm sized oleic acid coated Fe_3O_4 nanoparticles are 32 and 13% respectively, measured from the TGA studies.

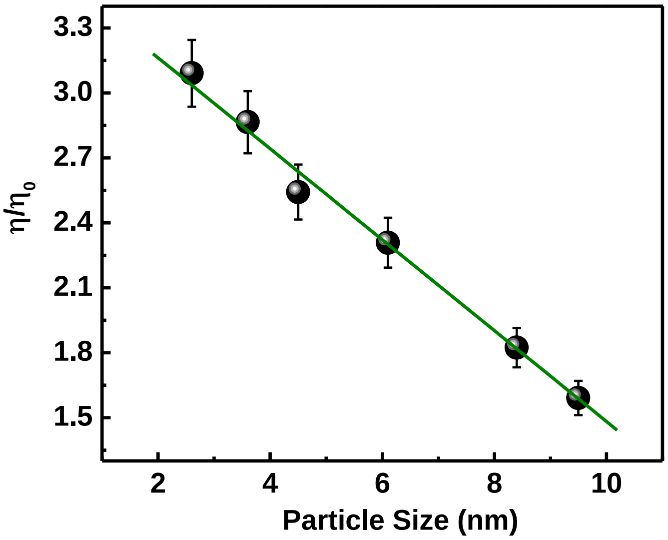

Fig. 7.3: The η/η_0 as a function of nanoparticles size for kerosene based magnetite nanofluids with $\phi=0.055$. Best fit is shown by the solid line.

Effect of nanoparticle size on the magnetoviscous effect of above nanofluids is also studied. Figure 7.4 shows the variation of η/η_0 as a function of magnetic field strength for kerosene based Fe_3O_4 nanofluids with different nanoparticles particle sizes (2.6–9.5 nm) at a particle loading of $\phi=0.055$. No enhancement in η is observed with increase in magnetic field strength for magnetite nanofluids with particles sizes of 2.6, 3.6, 4.5 and 6.1 nm. Nanofluids with bigger sizes (8.4 and 9.5 nm) showed an enhancement in η with increase in magnetic field strength, the increment being higher for 9.5 nm sized nanofluids.

Corresponding to the chain formation model, the magnetoviscous effect in ferrofluids is described as a result of the formation of chain-like structures due to strong interparticle interaction under the influence of a magnetic field.[305] Moreover, it is reported that strong shear can rupture the chains, due to strong viscous forces in the shear flow.[306, 343, 344] The extent of chain formation will be weak for magnetic nanofluids with smaller particle size because of low saturation magnetization and reduced dipolar interaction. Reduced dipolar attraction and shearing forces are responsible for the observed insignificant magnetovisocus effect of nanofluids with smaller size in the present study. The strong magnetic dipole interaction result in the formation of rigid nanoparticle chains along the field lines, causing an obstruction of the carrier fluid in its flow direction and thus an enhancement in η with increase in magnetic field strength for magnetite nanofluids with bigger size (8.4 and 9.5nm) particles.

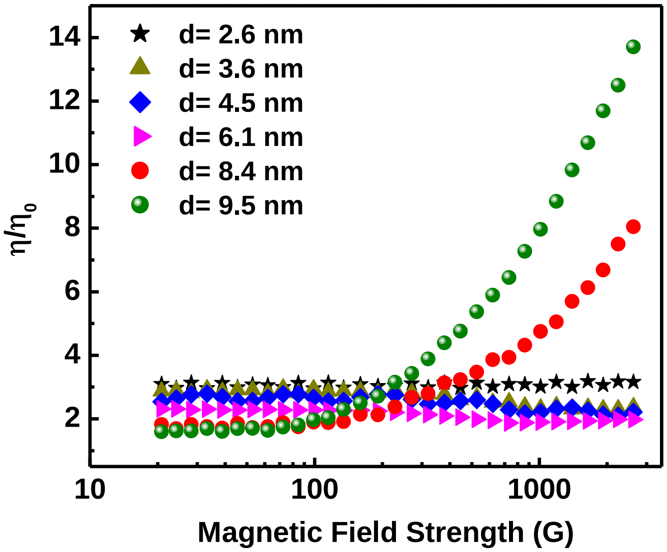

Fig. 7.4: The η/η_0 as a function of magnetic field strength for kerosene based Fe_3O_4 nanofluids having different nanoparticles sizes (2.6–9.5 nm) at a particle loading of ϕ=0.055.

An analysis of the rheological properties of ferrofluids indicates that a strong increase in the effective η under the action of an orienting field is possible, provided that a suspension contains nonspherical, sufficiently elongated objects (particles, aggregates, etc.).[345] In a conventional ferrofluids, such objects can be represented only by chain-like or bulky (drop like) aggregates. The latter acquire elongated shape under the action of an applied magnetic field. Simple estimates show that, magnetite particles with a diameter of 10 nm are so small that the energy of magnetic dipole interactions is considerably smaller than the thermal energy of the system.[343, 346] Therefore, only the largest particles are capable of forming linear bulky aggregates. However, the volume fraction of small particles and, hence, the osmotic pressure produced by this fraction, is large. When a bulky aggregate of large particles (present in a very small concentration) appears, small particles which are driven by the osmotic pressure to aggregate. As a result, the small particles that are neutral with respect to the magnetic dipole interactions occupy a part of the aggregate volume. Thus, the concentration of large particles involved into the magnetic dipole interaction in the aggregate decreases and the structure breaks.[347] However, magnetic nanofluids with high concentration of large diameter magnetic cores have strong magnetic field dependent change of the viscous behavior. Moreover, they exhibit weak shear thinning in presence of magnetic field resulting in a stronger magnetoviscous effect for high shear rates.[348]

7.4 Conclusions

In the present study, size dependant k and η studies are done in model nanofluids with long term stability. For kerosene based magnetite nanofluids with a fixed particle loading of ϕ=0.055, k/k_f increases from 1.05 to 1.25 with increasing particle diameter. Upon increasing the aspect ratio of the linear chains in nanofluids, very large enhancement in k is observed. These findings confirm that microconvection is not the key mechanism responsible for k enhancements.

The η/η_0 decreases from 3.09 to 1.59 with increasing particle diameter for kerosene based magnetite nanofluids at particle loading of ϕ=0.055. The larger surface area of solid/liquid interfaces and increased effective volume of solids together with the surfactant contribution results such variation in η with nanoparticle size. No enhancement in η is observed with increases in magnetic field strength for magnetite nanofluids with smaller size particles (2.6-6.1 nm). However, nanofluids with bigger sizes (8.4 and 9.5 nm) show an enhancement in η with increase in magnetic field strength, the increment being higher for 9.5 nm sized nanofluids.

Based on the present experimental results, it can be concluded that the particle size is a very important parameter in nanofluid property management of nanofluids. Considering heat transfer applications, both the k and η of nanofluids favor the use of larger particles over small ones. However, this approach is limited by the stability of suspensions with larger particles and possible erosion damage to the equipment. Therefore, an optical particle size is preferred for such applications.

Chapter – VIII

Conclusions and Perspectives

Contents

Chapter VIII | **Conclusions and Perspectives**

The present chapter summarizes the results on synthesis, characterization, thermal and rheological studies in magnetite (Fe_3O_4), copper oxide (CuO) and silver (Ag) nanofluids and perspectives.

8.1 Synthesis of Fe_3O_4, CuO and Ag Nanoparticles

- Surfactant stabilized Fe_3O_4 nanoparticles having different particle size are synthesized by varying the solvent dielectric constant of the medium during coprecipitation. The particle size increases with increase in dielectric constant of the solvent. The magnetization data confirms the superparamagnetic behavior with zero coercivity and remanence for Fe_3O_4 nanoparticles in the size range of 2 to 9 nm. The saturation magnetization is found to decrease with the decrease in nanoparticle size.

- Uncoated CuO nanoparticles of different particle sizes are synthesized by varying solvent dielectric constant of the medium during precipitation. The particle size increases with increase in dielectric constant of the solvent. For nanoparticles without coating, the average particle size measured using dynamic light scattering (DLS) is greater than the crystallite size because of aggregation of primary particles in the suspension.

- Oleylamine coated Ag nanoparticles are synthesized by reducing silver salt in presence of surfactant in a mixture of polar and nonpolar solvents. The UV-Visible spectrum shows an intense plasmon resonance absorption peak at 400 nm, due to the excitation of surface plasma resonance of spherical silver nanocrystals.

8.2 Factors Affecting Thermal Conductivity and Rheology of Nanofluids

- The present studies show a prominent role of aggregation on k enhancements of nanofluids. Stable nanofluids exhibit moderate k enhancement within the predictions EMT.[349] However, aggregating nanofluids show enhancement in thermal conductivity beyond EMT predictions.

- The aggregating nanofluids show a time dependent variation in k with elapsed time after sonication. The highest value of k/k_f is observed immediately after sonication, which decreases with elapsed time and finally reaches an equilibrium value after a time interval of about 45 minutes. [350] In the absence of stabilizers, the aggregation and the subsequent settling of agglomerates leads to a decrease in k with elapsed time.

- The cluster size and η/η_0 increases with elapsed time after sonication in aggregating nanofluids. Nanofluids with low particle loading shows least enhancement in η with time and the extent of η enhancement is high for nanofluids with higher particle loading, owing to the great degree of aggregation.

- The optical micrographs confirm cluster formation in unstable nanofluids with elapsed time and an increase in cluster size with time.

- Stable nanofluids with steric and electrostatic stabilization show time independent k with time. They also show an invariant particle size distribution and η with elapsed time.

- Sterically stabilized Ag nanofluids show no shift in plasmon resonance absorption with time indicating the absence of aggregation.

- Microscopy studies in surface modified nanofluids show no sign of aggregation (with cluster size > 200 nm) with time.

- The present results stress the need of surface functionalization of nanoparticles to improve the dispersion stability of nanofluids with least viscosity enhancement for practical applications.

- The k of aqueous nanofluids increase with temperature while it shows a decrease in nonaqueous nanofluids. The k/k_f remains constant with an increase in temperature, irrespective of nature of base fluids. These results suggest that the k of the nanofluids simply track the k of the base fluid and the enhancement in nanofluids relative to base fluids is essentially temperature independent.[351]

- The results unambiguously confirm the less dominant role of microconvection on k enhancement.

- Absolute η decreases with increase in temperature in both the base fluids and nanofluids and the η ratio remains almost constant with increase in temperature, which is a clear indication for the absence of aggregation of nanoparticles with temperature. These results confirm that nanofluid simply follows temperature depend viscosity behavior of base fluid and the observed variation in η with increasing temperature comes from the base fluid rather than the nanoparticles.

- Dynamic light scattering studies show no aggregation of nanoparticles with temperature in stable water and oil based nanofluids.

- The present results show that the aggregation is essentially governed by surface chemistry of nanoparticles and the stabilizing moieties used. Nanoparticle aggregation is insignificant with the increase in temperature in properly functionalized nanofluids. Such nanofluids are ideal for practical applications because of their long-term stability.

- For kerosene based magnetite nanofluids having a ϕ = 0.055, k/k_f increases from 1.05 to 1.25 with increasing particle diameter. Upon increasing the aspect ratio of the linear chains in nanofluids, very large enhancement of k is observed.[85]

- The results confirm that microconvection is not the key mechanism responsible for k enhancements in nanofluids.

- The η/η_0 decreases from 3.09 and 1.59 with increasing particle diameter for kerosene based magnetite nanofluids at particle loading of ϕ=0.055. The larger surface area of solid/liquid interfaces and increased effective volume of solids together with the surfactant contribution results in such variation in η with nanoparticle size.

- No enhancement in viscosity is observed with increase in magnetic field strength for magnetite nanofluids with smaller size particles (2.6–6.1 nm). However, nanofluids with bigger sizes (8.4 and 9.5 nm) showed an enhancement in viscosity with increase in magnetic field strength.

- Based on the present experimental results, it can be concluded that the particle size is a very important parameter for thermal property management in nanofluids.

8.3 Tuning of Thermal Conductivity and Rheology of Nanofluids Using External Stimuli

- A new approach to tune the thermal properties of magnetic nanofluids from low to very high values is demonstrated by varying the magnetic field strength and its orientation. This study reveals a unique possibility of tuning the k_{eff} /η_{eff} ratio in magnetically controllable nanofluids, making them superior to carbon nanotubes based suspensions in terms of reversible tunability of k for heat transport applications.[308]

- In the present study, dramatic k enhancement is observed in magnetite nanofluids under the influence of an applied magnetic field parallel to the temperature gradient. The higher the ϕ of nanofluids, the larger is the observed k increment. The maximum k enhancement observed is 300% for nanofluid with a particle loading of ϕ=0.063. As the magnetic field strength is increased progressively, the continuous conduction paths along the nanoparticle chains result in a series to parallel mode of conduction.[352]

- The decrease in k observed above a critical magnetic field strength is due to 'zippering' of chains, which is confirmed by microscopy studies.[353]

- k measurements under different magnetic field orientations with respect to the thermal gradient show maximum k enhancement when the field direction is exactly parallel to the thermal gradient. No enhancement is observed when field direction is perpendicular to the thermal gradient. A gradual reduction in the k enhancement is observed as the field direction is shifted from parallel to perpendicular direction with respect to thermal gradient.[354]

- When nanoparticles starts to form aggregates of larger size or chains, the convection velocity drops drastically due to the cubic dependence on the particle size and the Brownian motion is severely reduced. Thus the observed field induced k enhancement confirms that the microconvection is not the mechanism responsible for k enhancement.

- The increase in k for magnetic nanofluids under external magnetic field is attributed to the effective conduction of heat through the chainlike structures formed under magnetic field when the dipolar interaction energy becomes greater than the thermal energy.

- The k measurements in stable oil based magnetite nanofluids during rise and decay of magnetic field strength show that the k enhancement is reversible with a small hysteresis under repeated magnetic cycling. The observed reversible tunable thermal property of nanofluid may find many technological applications in NEMS and MEMs based devices.[355]

- Reversible field induced η enhancement with a slight hysteresis is observed in stable oil based magnetite nanofluids during the rise and decay of magnetic field strength.

8.4 Perspectives

- Thermal conductivity measurements under flow through micro channels subjected to a magnetic field

- Thermal conductivity studies in
    - Coreshell nanofluids
    - Binary nanofluids
    - Nanotubes and nanofibers based nanofluids
    - Nanoemulsions
    - Smart structures

- Effect of additives on k of nanofluids

LIST OF REFERENCES

[1] R.P. Feynman, Plenty of Room at the Bottom, http://www.its.caltech.edu/feynman/plenty.html., APS Annual Meeting, 1959.

[2] P. Walter, E. Welcomme, P. Hallegot, N.J. Zaluzec, C. Deeb, J. Castaing, P. Veyssiere, R. Breniaux, J.L. Leveque, G. Tsoucaris, Nano Lett. **6** (2006) 2215.

[3] I. Freestone, N. Meeks, M. Sax, C. Higgitt, Gold Bull. **40** (2007) 270.

[4] M. Reibold, P. Paufler, A.A. Levin, W. Kochmann, N. Patzke, D.C. Meyer, Nature **444** (2006) 286.

[5] M. Faraday, Philos. Trans. R. Soc. London **147** (1857) 145.

[6] R.R. Schaller, IEEE Spectrum **34** (1997) 52.

[7] G. Binnig, H. Rohrer, C. Gerber, E. Weibel, Phys. Rev. Lett. **49** (1982) 57.

[8] G. Binnig, C.F. Quate, C. Gerber, Phys. Rev. Lett. **56** (1986) 930.

[9] H.W. Kroto, J.R. Heath, S.C. O'Brien, R.F. Curl, R.E. Smalley, Nature **318** (1985) 162.

[10] S. Iijima, Nature **354** (1991) 56.

[11] R.H. Baughman, A.A. Zakhidov, W.A.D. Heer, Science **297** (2002) 787.

[12] K.S. Novoselov, A.K. Geim, S.V. Morozov, D. Jiang, Y. Zhang, S.V. Dubonos, I.V. Grigorieva, A.A. Firsov, Science **306** (2004) 666.

[13] A.K. Geim, Science **324** (2009) 1530.

[14] M. Li, H. Schnablegger, S. Mann, Nature **402** (1999) 393.

[15] G. Cao, Nanostructures & nanomaterials: synthesis, properties & applications, Imperial College Press, London, 2000.

[16] H. Ogawa, M. Nishikawa, A. Abe, J. Appl. Phys. **53** (1982) 4448.

[17] C. Herring, J.K. Galt, Phys. Rev. **85** (1952) 1060.

[18] M.S. Dresselhaus, G. Dresselhaus, P. Avouris, Carbon nanotubes: synthesis, structure, properties, and applications, Springer, Berlin, 2001.

[19] R.M. Costescu, D.G. Cahill, F.H. Fabreguette, Z.A. Sechrist, S.M. George, Science **303** (2004) 989.

[20] W.U. Huynh, J.J. Dittmer, A.P. Alivisatos, Science **295** (2002) 2425.

[21] Y. Sun, Y. Xia, Science **298** (2002) 2176.

[22] P.V. Kamat, J. Phys. Chem. B **106** (2002) 7729.

[23] R. Narayanan, M.A.E. Sayed, J. Phys. Chem. B **109** (2005) 12663.

[24] Y. Yin, R.M. Rioux, C.K. Erdonmez, S. Hughes, G.A. Somorjai, A.P. Ivisatos, Science **304** (2004) 711.

[25] A.C. Balazs, T. Emrick, T.P. Russell, Science **314** (2006) 1107.

[26] C.C. Berry, A.S.G. Curtis, J. Phys. D: Appl. Phys. **36** (2003) R198.

[27] S.H. Choi, H.B. Na, Y.I. Park, K. An, S.G. Kwon, Y. Jang, M.H. Park, J. Moon, J.S. Son, I.C. Song, W.K. Moon, T. Hyeon, J. Am. Chem. Soc. **130** (2008) 15573.

[28] C.T. Yavuz, J.T. Mayo, W.W. Yu, A. Prakash, J.C. Falkner, S. Yean, L. Cong, H.J. Shipley, A. Kan, M. Tomson, D. Natelson, V.L. Colvin, Science **314** (2006) 964.

[29] J.J. Chiu, B.J. Kim, E.J. Kramer, D.J. Pine, J. Am. Chem. Soc. **127** (2005) 5036.

[30] M.A. Willard, L.K. Kurihara, E.E. Carpenter, S. Calvin, V.G. Harris, Int. Mater. Rev. **49** (2004) 125.

[31] S.U.S. Choi, ASME J. Heat Transfer **131** (2009) 033106.

[32] S. Lee, S.U.S. Choi, S. Li, J.A. Eastman, ASME J. Heat Transfer **121** (1999) 280.

[33] J.A. Eastman, S.U.S. Choi, S. Li, W. Yu, L.J. Thompson, Appl. Phys. Lett. **78** (2001) 718.

[34] W. Yu, H. Xie, D. Bao, Nanotechnology **21** (2010) 055705.

[35] W. Yu, H. Xie, W. Chen, J. Appl. Phys. **107** (2010) 094317

[36] W. Yu, H. Xie, X. Wang, X. Wang, Phys. Lett. A **375** (2011) 1323.

[37] J.C. Maxwell, A Treatise on Electricity and Magnetism, II ed., Clarendon, Oxford, 1881.

[38] H.E. Patel, S.K. Das, T. Sundararajan, A.S. Nair, B. George, T. Pradeep, Appl. Phys. Lett. **83** (2003) 2931.
[39] T.K. Hong, H.S. Yang, C.J. Choi, J. Appl. Phys. **97** (2005) 064311.
[40] H.U. Kang, S.H. Kim, J.M. Oh, Exp. Heat Transfer **19** (2006) 181.
[41] H. Zhu, C. Zhang, S. Liu, Y. Tang, Y. Yin, Appl. Phys. Lett. **89** (2006) 023123.
[42] S.M.S. Murshed, K.C. Leong, C. Yang, Int. J. Therm. Sci. **44** (2005) 367.
[43] X. Zhang, H. Gu, M. Fujii, Int. J. Thermophys. **27** (2006) 569.
[44] H.T. Zhu, C.Y. Zhang, Y.M. Tang, J.X. Wang, J. Phys. Chem. C **111** (2007) 1646.
[45] D. Wen, Y. Ding, IEEE Trans. Nanotech. **5** (2006) 220.
[46] W. Williams, J. Buongiorno, L.W. Hu, ASME J. Heat Transfer **130** (2008) 042412.
[47] C.Y. Hong, C.C. Wu, Y.C. Chiu, S.Y. Yang, H.E. Horng, H.C. Yang, Appl. Phys. Lett. **88** (2006) 212512.
[48] Q. Li, Y. Xuan, J. Wang, Exp. Therm. Fluid Sci. **30** (2005) 109.
[49] C.H. Chon, K.D. Kihm, S.P. Lee, S.U.S. Choi, Appl. Phys. Lett. **87** (2005) 153107.
[50] S.M.S. Murshed, K.C. Leong, C. Yang, J. Phys. D: Appl. Phys. **39** (2006) 5316.
[51] M. Chopkar, P.K. Das, I. Manna, Scr. Mater. **55** (2006) 549.
[52] M. Chopkar, S. Kumar, D.R. Bhandari, P.K. Das, I. Mannaa, Mater. Sci. Eng. B **139** (2007) 141.
[53] C.H. Li, G.P. Peterson, J. Appl. Phys. **101** (2007) 044312
[54] C.H. Li, G.P. Peterson, J. Appl. Phys. **99** (2006) 084314.
[55] D. Hwang, K.S. Hong, H.S. Yang, Thermochim. Acta **455** (2007) 66.
[56] J.R.V. Penas, J.M.O.d. Zarate, M. Khayet, J. Appl. Phys. **104** (2008) 044314.
[57] A.J. Schmidt, M. Chiesa, D.H. Torchinsky, J.A. Johnson, K.A. Nelson, G. Chen, J. Appl. Phys. **103** (2008) 083529.
[58] K. Sinha, B. Kavlicoglu, Y. Liu, F. Gordaninejad, O.A. Graeve, J. Appl. Phys. **106** (2009) 064307.
[59] P.E. Gharagozloo, J.K. Eaton, K.E. Goodson, Appl. Phys. Lett. **93** (2008) 103110.
[60] J. Buongiorno, J. Appl. Phys. **106** (2009) 094312.
[61] J.W. Gao, R.T. Zheng, H. Ohtani, D.S. Zhu, G. Chen, Nano Lett. **9** (2009) 4128.
[62] N. Shalkevich, W. Escher, T. Burgi, B. Michel, L.S. Ahmed, D. Poulikakos, Langmuir **26** (2010) 663.
[63] D. Singh, E. Timofeeva, W. Yu, J. Routbort, D. France, D. Smith, J.M.L. Cepero, J. Appl. Phys. **105** (2009) 064306.
[64] R. Rusconi, E. Rodari, R. Piazza, Appl. Phys. Lett. **89** (2006) 261916
[65] D.C. Venerus, M.S. Kabadi, S. Lee, V.P. Luna, J. Appl. Phys. **100** (2006) 094310.
[66] S.A. Putnam, D.G. Cahill, P.V. Braun, Z. Ge, R.G. Shimmin, J. Appl. Phys. **99** (2006) 084308.
[67] X. Zhang, H. Gu, M. Fujii, J. Appl. Phys. **100** (2006) 044325.
[68] Y.S. Ju, J. Kim, M.T. Hung, ASME J. Heat Transfer **130** (2008) 092403.
[69] E.V. Timofeeva, A.N. Gavrilov, J.M. McCloskey, Y.V. Tolmachev, S. Sprunt, L.M. Lopatina, J.V. Selinger, Phys. Rev. E **76** (2007) 061203
[70] H. Xie, J. Wang, T. Xi, Y. Liu, Int. J. Thermophys. **23** (2002) 571.
[71] J. Eapen, R. Rusconi, R. Piazza, S. Yip, ASME J. Heat Transfer **132** (2010) 102402.
[72] T.P. Teng, Y.H. Hung, T.C. Teng, H.E. Moa, H.G. Hsu, App. Therm. Eng. **30** (2010) 2213.
[73] H.E. Patel, T. Sundararajan, S.K. Das, J. Nanopart. Res. **12** (2010) 1015.
[74] H.A. Mintsa, G. Roy, C.T. Nguyen, D. Doucet, Int. J. Therm. Sci. **48** (2009) 363.
[75] K.B. Anoop, T. Sundararajan, S.K. Das, Int. J. Heat Mass Transfer **52** (2009) 2189.
[76] R.S. Vajjha, D.K. Das, Int. J. Heat Mass Transfer **52** (2009) 4675.
[77] M. Chopkar, S. Sudarshan, P.K. Das, I. Manna, Mettal. Mater Trans. A **39** (2008) 1535.
[78] S.H. Kim, S.R. Choi, D. Kim, ASME J. Heat Transfer **129** (2007) 298.
[79] J. Hong, S.H. Kim, D. Kim, J. Phys.: Conference Series **59** (2007) 301.
[80] Y. He, Y. Jin, H. Chen, Y. Ding, D. Cang, H. Lu, Int. J. Heat Mass Transfer **50** (2007) 2272.

[81] E.V. Timofeeva, D.S. Smith, W. Yu, D.M. France, D. Singh, J.L. Routbort, Nanotechnology **21** (2010) 215703.
[82] M.P. Beck, Y. Yuan, P. Warrier, A.S. Teja, J. Nanopart. Res. **12** (2010) 1469.
[83] M.P. Beck, Y. Yuan, P. Warrier, A.S. Teja, J. Nanopart. Res. **11** (2009) 1129.
[84] M.P. Beck, Y. Yuan, P. Warrier, A.S. Teja, J. Appl. Phys. **107** (2010) 066101.
[85] P.D. Shima, J. Philip, B. Raj, Appl. Phys. Lett. **94** (2009) 223101
[86] W. Yu, H. Xie, L. Chen, Y. Li, Powder Technol. **197** (2009) 218.
[87] S.M.S. Murshed, K.C. Leong, C. Yang, Int. J. Therm. Sci. **47** (2008) 560.
[88] C.H. Li, G.P. Peterson, Adv. Mech. Eng. **2010** (2010) 1.
[89] C.J. Ho, J.Y. Gao, Int. Commu. Heat Mass Transfer **36** (2009) 467.
[90] D. Kim, Y. Kwon, Y. Cho, C. Li, S. Cheong, Y. Hwang, J. Lee, D. Hong, S. Moon, Curr. Appl. Phys. **9** (2009) e119.
[91] C.S. Jwo, L.Y. Jeng, H. Chang, T.P. Teng, Rev. Adv .Mater. Sci. **18** (2008) 660.
[92] K.F.V. Wong, T. Kurma, Nanotechnology **19** (2008) 345702.
[93] L.S. Sundar, K.V. Sharma, Int. J. Nanoparticles **1** (2008) 66.
[94] L.S. Sundar, K.V. Sharma, Int. J. Dynamics of Fluids **4** (2008) 57.
[95] S.K. Das, N. Putra, W. Roetzel, Int. J. Heat Mass Transfer **46** (2003) 851.
[96] S. Habibzadeh, A.K. Beydokhti, A.A. Khodadadi, Y. Mortazavi, S. Omanovic, M.S. Niassar, Chem. Eng. J. **156** (2010) 471.
[97] M. Yeganeh, N. Shahtahmasebi, A. Kompany, E.K. Goharshadi, A. Youssefi, L. Siller, Int. J. Heat Mass Transfer **53** (2010) 3186.
[98] H. Chen, W. Yang, Y. He, Y. Ding, L. Zhang, C. Tan, A.A. Lapkin, D.V. Bavykin, Powder Technol. **183** (2008) 63.
[99] Q. Yu, Y.J. Kim, H. Ma, Appl. Phys. Lett. **92** (2008) 103111.
[100] H. Xie, L. Chen, Phys. Lett. A **373** (2009) 1861.
[101] N. Jha, S. Ramaprabhua, J. Appl. Phys. **106** (2009) 084317.
[102] P. Garg, J.L. Alvarado, C. Marsh, T.A. Carlson, D.A. Kessler, K. Annamalai, Int. J. Heat Mass Transfer **52** (2009) 5090.
[103] A. Amrollahi, A.A. Hamidi, A.M. Rashidi, Nanotechnology **19** (2008) 315701.
[104] Z.H. Han, B. Yang, S.H. Kim, M.R. Zachariah, Nanotechnology **18** (2007) 105701.
[105] Y. Ding, H. Alias, D. Wen, R.A. Williams, Int. J. Heat Mass Transfer **49** (2006) 240.
[106] K. Parekh, H.S. Lee, J. Appl. Phys. **107** (2010) 09A310.
[107] M. Kole, T.K. Dey, J. Phys. D: Appl. Phys. **43** (2010) 315501.
[108] W. Yu, H. Xie, L. Chen, Y. Li, Colloids Surf. A **355** (2010) 109.
[109] W. Yu, H. Xie, L. Chen, Y. Li, Thermochim. Acta **491** (2009) 92.
[110] X. Zhang, H. Gu, M. Fujii, Exp. Therm. Fluid Sci. **31** (2007) 593.
[111] V.E. Fertman, L.E. Golovicher, N.P. Matusevich, J. Magn. Magn. Mater. **65** (1987) 211.
[112] M.J. Assael, K.D. Antoniadis, I.N. Metaxa, J. Chem. Eng. Data **54** (2009) 2365.
[113] L. Chen, H. Xie, Y. Li, W. Yu, Thermochim. Acta **477** (2008) 21.
[114] J. Glory, M. Bonetti, M. Helezen, M.M.L. Hermite, C. Reynaud, J. Appl. Phys. **103** (2008) 094309.
[115] W. Duangthongsuk, S. Wongwises, Exp. Therm. Fluid Sci. **33** (2009) 706.
[116] B. Yang, Z.H. Han, Appl. Phys. Lett. **89** (2006) 083111
[117] E.V. Timofeeva, J.L. Routbort, D. Singh, J. Appl. Phys. **106** (2009) 014304.
[118] W. Jiang, G. Ding, H. Peng, Int. J. Therm. Sci. **48** (2009) 1108.
[119] A.S. Cherkasova, J.W. Shan, ASME J. Heat Transfer **130** (2008) 082406.
[120] K.J. Lee, S.H. Yoon, y. Jang, Small **3** (2007) 1209.
[121] Y. Yang, E.A. Grulke, Z.G. Zhang, G. Wu, J. Appl. Phys. **99** (2006) 114307.

[122] M.J. Assael, I.N. Metaxa, J. Arvanitidis, D. Christofilos, C. Lioutas, Int. J. Thermophys. **26** (2005) 647.
[123] M.J. Assael, C.F. Chen, I. Metaxa, W.A. Wakeham, Int. J. Thermophys. **25** (2004) 971.
[124] R. Gowda, H. Sun, P. Wang, M. Charmchi, F. Gao, Z. Gu, B. Budhlall, Adv. Mech. Eng. **2010** (2010) 1.
[125] X.J. Wang, D.S. Zhu, S. yang, Chem. Phys. Lett. **470** (2009) 107.
[126] D.H. Yoo, K.S. Hong, H.S. Yang, Thermochim. Acta **455** (2007) 66.
[127] Y.J. Hwang, Y.C. Ahn, H.S. Shin, C.G. Lee, G.T. Kim, H.S. Park, J.K. Lee, Curr. Appl. Phys. **6** (2006) 1068.
[128] K.S. Hong, T.K. Hong, H.S. Yang, Appl. Phys. Lett. **88** (2006) 031901.
[129] T.K. Hong, H.S. Yang, J. Korean Phys. Soc. **47** (2005) S321.
[130] Y. Xuan, Y. Huang, Q. Li, Chem. Phys. Lett. **479** (2009) 264.
[131] H. Xie, J. Wang, T. Xi, Y. Liu, F. Ai, Q. Wu, J. Appl. Phys. **91** (2002) 4568.
[132] M.S. Liu, M.C.C. Lin, I.T. Huang, C.C. Wang, Int. Commu. Heat Mass Transfer **32** (2005) 1202.
[133] H. Xie, H. Lee, W. Youn, M. Choi, J. Appl. Phys. **94** (2003) 4967.
[134] D. Zhu, X. Li, N. Wang, X. Wang, J. Gao, H. Li, Curr. Appl. Phys. **9** (2009) 131.
[135] X.F. Li, D.S. Zhu, X.J. Wang, N. Wang, J.W. Gao, H.Li, Thermochim. Acta **469** (2008) 98.
[136] D. Lee, J.W. Kim, B.G. Kim, J. Phys. Chem. B **110** (2006) 4323.
[137] M.E. Meibodi, M.V. Sefti, A.M. Rashidi, A. Amrollahi, M. Tabasi, H.S. Kalal, Int. Commu. Heat Mass Transfer **37** (2010) 319.
[138] N.R. Karthikeyan, J. Philip, B. Raj, Mater. Chem. Phys. **109** (2008) 50.
[139] M.S. Liu, M.C.C. Lin, C.Y. Tsai, C.C. Wang, Int. J. Heat Mass Transfer **49** (2006) 3028.
[140] P. Keblinski, J.A. Eastman, D.G. Cahill, Mater. Today **8** (2005) 36.
[141] P. Keblinski, R. Prasher, J. Eapen, J. Nanopart. Res. **10** (2008) 1089.
[142] R. Prasher, P.E. Phelan, P. Bhattacharya, Nano Lett. **6** (2006) 1529.
[143] J. Garg, B. Poudel, M. Chiesa, J.B. Gordon, J.J. Ma, J.B. Wang, Z.F. Ren, Y.T. Kang, H. Ohtani, J. Nanda, G.H. McKinley, G. Chen, J. Appl. Phys. **103** (2008) 074301.
[144] R. Prasher, D. Song, J. Wang, P. Phelan, Appl. Phys. Lett. **89** (2006) 133108.
[145] K.B. Anoop, S. Kabelac, T. Sundararajan, S.K. Das, J. Appl. Phys. **106** (2009) 034909.
[146] S.Q. Zhou, R. Ni, D. Funfschilling, J. Appl. Phys. **107** (2010) 054317.
[147] J. Chevalier, O. Tillement, F. Ayela, Phys. Rev. E **80** (2009) 051403.
[148] N. Shalkevich, A. Shalkevich, T. Burgi, J. Phys. Chem. C **114** (2010) 9568.
[149] Y. He, Y. Men, X. Liu, H. Lu, H. Chen, Y. Ding, J. Therm. Sci **18** (2009) 20.
[150] J. Nanda, C. Maranville, S.C. Bollin, D. Sawall, H. Ohtani, J.T. Remillard, J.M. Ginder, J. Phys. Chem. C **112** (2008) 654.
[151] E. Tamjid, B.H. Guenther, Powder Technol. **197** (2010) 49.
[152] A. Mishra, S. Ram, G. Ghosh, J. Phys. Chem. C **113** (2009) 6976.
[153] S.P. Jang, J.H. Lee, K.S. Hwang, S.U.S. Choi, Appl. Phys. Lett. **91** (2007) 243112.
[154] J.Y. Jeng, J.C. Liu, J.H. Jean, J. Am. Ceram. Soc. **90** (2007) 3676.
[155] K.C. Etika, F.D. Jochum, P. Theato, J.C. Grunlan, J. Am. Chem. Soc. **131** (2009) 13598.
[156] Y.S. Lee, N.J. Wagner, Ind. Eng. Chem. Res. **45** (2006) 7015.
[157] J.C. Grunlan, L. Liu, Y.S. Kim, Nano Lett. **6** (2006) 911.
[158] O.T. Mefford, M.L. Vadala, J.D. Goff, M.R.J. Carroll, R.M. Ariza, B.L. Caba, T.G.S. Pierre, R.C. Woodward, R.M. Davis, J.S. Riffle, Langmuir **24** (2008) 5060.
[159] S.W. Ko, J.Y. Lim, B.J. Park, M.S. Yang, H.J. Choi, J. Appl. Phys. **105** (2009) 07E703.
[160] J.H. Lee, K.S. Hwang, S.P. Jang, B.H. Lee, J.H. Kim, S.U.S. Choi, C.J. Choi, Int. J. Heat Mass Transfer **51** (2008) 2651.

[161] C.T. Nguyen, F. Desgranges, N. Galanis, G. Roy, T. Mare, S. Boucher, H.A. Mintsa, Int. J. Therm. Sci. **47** (2008) 103.
[162] M.J.P. Gallego, C. Casanova, R. Paramo, B. Barbes, J.L. Legido, M.M. Pineiro, J. Appl. Phys. **106** (2009) 064301.
[163] H. Chen, S. Witharana, Y. Jina, C. Kim, Y. Ding, Particuology **7** (2009) 151.
[164] L. Chen, H. Xie, Colloids Surf. A **352** (2009) 136.
[165] D.O. Smith, Phys. Rev. **102** (1956) 959.
[166] C.P. Bean, J.D. Livingston, J. Appl. Phys. **30** (1959) S120.
[167] J. Frenkel, J. Doefman, Nature **126** (1930) 274.
[168] D.L.L. Pelecky, Chem. Mater. **8** (1996) 1770.
[169] A.K. Gupta, M. Gupta, Biomaterials **26** (2005) 3995.
[170] B.D. Terris, T. Thomson, J. Phys. D: Appl. Phys. **38** (2005) R199.
[171] D. Makovec, A. Kosak, A. Znidarsic, M. Drofenik, J. Magn. Magn. Mater. **289** (2005) 32.
[172] Z. Li, L. Wei, M.Y. Gao, H. Lei, Adv. Mater. **17** (2005) 1001.
[173] A.E. Rakhshani, Solid State Electron. **29** (1986) 7.
[174] M.L. Zhong, D.C. Zeng, Z.W. Liu, H.Y. Yu, X.C. Zhong, W.Q. Qiu, Acta Mater. **58** (2010) 5926.
[175] P. Dai, H.A. Mook, G. Aeppli, S.M. Hayden, F. Dogan, Nature Mater. **406** (2000) 965.
[176] S. Anandan, X. Wen, S. Yang, Mater. Chem. Phys. **93** (2005) 35.
[177] K.L. Hardee, A.J. Bard, J. Electrochem. Soc. **124** (1977) 215.
[178] J.B. Reitz, E.I. Solomon, J. Am. Chem. Soc. **120** (1998) 11467.
[179] F. Teng, W. Yao, Y. Zheng, Y. Ma, Y. Teng, T. Xu, S. Liang, Y. Zhu, Sensors and Actuators B **134** (2008) 761.
[180] G. Ren, D. Hu, E.W.C. Cheng, M.A.V. Reus, P. Reip, R.P. Allaker, Int J Antimicrob Agents. **33** (2009) 587.
[181] C.J. Murphy, T.K. Sau, A.M. Gole, C.J. Orendorff, J. Gao, L. Gou, S.E. Hunyadi, T. Li, J. Phys. Chem. B **109** (2005) 13857.
[182] D.D. Evanoff, G. Chumanov, Chem. Phys. Chem **6** (2005) 1221.
[183] R.J. Chimentao, I. Kirm, F. Medina, X. Rodriguez, Y. Cesteros, P. Salagre, J.E. Sueiras, Chem. Commun. (2004) 846.
[184] C. Aymonier, U. Schlotterbeck, L. Antonietti, P. Zacharias, R. Thomann, J.C. Tiller, S. Mecking, Chem. Commun. (2002) 3018.
[185] A.D.M. Farland, R.P.V. Duyne, Nano Lett. **3** (2003) 1057.
[186] Y. Li, Y. Wu, B.S. Ong, J. Am. Chem. Soc. **127** (2005) 3266.
[187] W. Wang, S.A. Asher, J. Am. Chem. Soc. **123** (2001) 12528.
[188] J. Park, K. An, Y. Hwang, J.G. Park, H.J. Noh, J.Y. Kim, J.H. Park, N.M. Hwang, T. Hyeon, Nature Mater. **3** (2004) 891.
[189] D. Yu, V.W.W. Yam, J. Phys. Chem. B **109** (2005) 5497.
[190] Y.W. Cao, R. Jin, C.A. Mirkin, J. Am. Chem. Soc. **123** (2001) 7961.
[191] S. Peng, S. Sun, Angew. Chem. Int. Ed. **46** (2007) 4155.
[192] S.-H. Choi, H.B. Na, Y.I. Park, K. An, S.G. Kwon, Y. Jang, M. Park, J. Moon, J.S. Son, I.C. Song, W.K. Moon, T. Hyeon, J. Am. Chem. Soc. **130** (2008) 15573.
[193] H. Zeng, S. Sun, Adv. Funct. Mater. **18** (2008) 391.
[194] S.S. Papell, U.S. Patent **3215572** (1965).
[195] J. Ding, T. Tsuzuki, P.G.M. Cormick, J. Magn. Magn. Mater. **177-181** (1998) 931.
[196] B.L. Cushing, V.L. Kolesnichenko, C.J. O'Connor, Chem. Rev. **104** (2004) 3893.
[197] J. Rockenberger, E.C. Scher, A.P. Alivisatos, J. Am. Chem. Soc. **121** (1999) 11595.
[198] Y. Lee, J. Lee, C.J. Bae, J.G. Park, H.J. Noh, J.H. Park, T. Hyeon, Adv. Funct. Mater. **15** (2005) 503.
[199] C. Burda, X. Chen, R. Narayanan, M.A.E. Sayed, Chem. Rev. **105** (2005) 1025.

[200] G.W. Reimers, S.E. Khalafalla, US Patent **3843540** (1974).
[201] R. Massart, IEEE Trans. Magn. **17** (1981) 1247.
[202] R. Massart, US Patent **4329241** (1982).
[203] R. Massart, E. Dubois, V. Cabuil, E. Hasmonay, J. Magn. Magn. Mater. **149** (1995) 1.
[204] J.R. Thomas, J. Appl. Phys. **37** (1966) 2914.
[205] A.E. Berkowitz, J.L. Walter, US Patent **4381244** (1983).
[206] M. Ueda, H. Dietz, A. Anders, H. Kneppe, A. Meixner, W. Plieth, Electrochim. Acta **48** (2002) 377.
[207] R.B. Frankel, R.P. Blakemore, R.S. Wolfe, Science **203** (1979) 1355.
[208] G. Gnanaprakash, J. Philip, T. Jayakumar, B. Raj, J. Phys. Chem. B **111** (2007) 7978.
[209] C.L. Carnes, K.J. Klabunde, J. Mol. Catal **194** (2003) 227.
[210] J. Zhu, D. Li, H. Chen, X. Yang, L. Lu, X. Wang, Mater. Lett. **58** (2004) 3324.
[211] R.V. Kumar, R. Elgamiel, Y. Diamant, A. Gedanken, J. Norwig, Langmuir **17** (2001) 1406.
[212] H. Wang, J.Z. Xu, J.J. Zhu, H.Y. Chen, J. Cryst. Growth **244** (2002) 88.
[213] Z.S. Hong, Y. Gao, J.F. Deng, Mater. Lett. **52** (2002) 34.
[214] X.G. Zheng, C.N. Xu, K. Nishikubo, K. Nishiyama, W. Higemoto, W.J. Moon, E. Tanaka, E.S. Otabe, Phy. Rev. B **72** (2006) 014464.
[215] C. Carel, M.M. Bahout, J. Gaude, Solid State Ion. **117** (1999) 47.
[216] J. Rockenberger, E.C. Scher, A.P. Alivisatos, J. Am. Chem. Soc. **121** (1999) 11595.
[217] R.V. Kumar, Y. Diamant, A. Gedanken, Chem. Mater. **12** (2000) 2301.
[218] Z.S. Hong, Y. Cao, J.F. Deng, Mater. Lett. **52** (2002) 34.
[219] C.C. Li, M.H. Chang, Mater. Lett. **58** (2004) 3903.
[220] J. Zhu, D. Li, H. Chen, X. Yang, L. Lu, X. Wang, Mater.Lett. **58** (2004) 3324.
[221] D. Romanska, M. Mazur, Langmuir **19** (2003) 4532.
[222] A. Taleb, C. Petit, M.P. Pileni, Chem. Mater. **9** (1997) 950.
[223] R.C. Jin, Y.W. Cao, C.A. Mirkin, K.L. Kelly, G.C. Schatz, J.G. Zheng, Science **294** (2001) 1901.
[224] W. Wang, X. Chen, S. Efrima, J. Phys. Chem. B **103** (1999) 7238.
[225] L.P. Jiang, S. Xu, J.M. Zhu, J.R. Zhang, J.J. Zhu, H.Y. Chen, Inorg. Chem. **43** (2004) 5877.
[226] A.A. Zinchenko, K. Yoshikawa, D. Baigl, Adv. Mater. **17** (2005) 2820.
[227] M. Chen, Y.G. Feng, X. Wang, T.C. Li, J.Y. Zhang, D.J. Qian, Langmuir **23** (2007) 5296.
[228] A. Henglein, M. Giersig, J. Phys. Chem. B **103** (1999) 9533.
[229] H.H. Huang, X.P. Ni, G.L. Loy, C.H. Chew, K.L. Tan, F.C. Loh, J.F. Deng, G.Q. Xu, Langmuir **12** (1996) 909.
[230] F. Gao, Q. Lu, S. Komarneni, Chem. Mater. **17** (2005) 856.
[231] J. Zhang, B. Han, M. Liu, D. Liu, Z. Dong, J. Liu, D. Li, J. Wang, B. Dong, H. Zhao, L. Rong, J. Phys. Chem. B **107** (2003) 3679.
[232] Y.-S. Shon, E. Cutler, Langmuir **20** (2004) 6626.
[233] A. Taleb, C. Petit, M.P. Pileni, Chem. Mater. **9** (1997) 950.
[234] N.R. Jana, X. Peng, J. Am. Chem. Soc. **125** (2003,) 14280.
[235] N.R. Jana, X. Peng, J. Am. Chem. Soc. **125** (2003) 14280.
[236] C. Kittel, Introduction to Solid State Physics, Seventh ed., John Wiley & Sons, U.K, 2004.
[237] D.B. Williams, C.B. Carter, Transmission Electron Microscopy : A Textbook for Materials Science, Springer, New York, 1996.
[238] W. Schartl, Light Scattering from Polymer Solutions and Nanoparticle Dispersions, Springer, Germany, 2007.
[239] J.C. Thomas, J. Colloid Interface Sci. **117** (1987) 187.
[240] Y. Zhu, M.M. Neary, N. Breslin, J. Liu, J. Int. J. Mod. Phys. B **13** (1999) 2044.
[241] B.J.d. Gans, N.J. Duin, D.v.d. Ende, J. Mellema, J. Chem. Phys. **113** (2000) 2032.
[242] L. Mazzola, Nat. Biotechnol. **21** (2003) 1137.

[243] K.L. Kelly, E. Coronado, L.L. Zhao, G.C. Schatz, J. Phys. Chem. B **107** (2003) 668.
[244] M. Chen, Y. Cai, Z. Yan, D.W. Goodman, J. Am. Chem. Soc. **128** (2006) 6341.
[245] G. Reiss, A. Hutten, Nature Mater. **4** (2005) 725.
[246] J. Park, J. Joo, S.G. Kwon, Y. Jang, T. Hyeon, Angew. Chem. Int. Ed. **46** (2007) 4630.
[247] V.F. Puntes, K.M. Krishnan, A.P. Alivisatos, Science **291** (2011) 2115.
[248] S. Sun, H. Zeng, J. Am. Chem. Soc. **124** (2002) 8204.
[249] J.W. Mullin, Crystallization, 3rd ed., Oxford University Press, Oxford, 1997.
[250] P. Dutta, S. Pal, M.S. Seehra, N. Shah, G.P. Huffman, J. Appl. Phys. **105** (2009) 07B501.
[251] Z. Li, H. Chen, H. Bao, M. Gao, Chem. Mater. **16** (2004) 1391.
[252] B.D. Cullity, Introduction to Magnetic Minerals, Addison - Wesley, New York, 1972.
[253] R. Yanes, O.C. Fesenko, H. Kachkachi, D.A. Garanin, R. Evans, R.W. Chantrell, Phys. Rev. B **76** (2007) 064416.
[254] H. Shim, P. Duttaa, M.S. Seehra, J. Bonevich, Solid State Commun. **145** (2008) 192.
[255] A.E. Berkowitz, W.L. Schuele, P.J. Flanders, J. Appl. Phys. **39** (1968) 1261.
[256] Z.X. Tang, C.M. Sorensen, K.J. Klabunde, Phys. Rev. Lett. **67** (1991) 3602.
[257] Y. Sahoo, H. Pizem, T. Fried, D. Golodnitsky, L. Burstein, C.N. Sukenik, G. Markovich, Langmuir **17** (2001) 7907.
[258] V.P. Dieste, O.M. Castellini, J.N. Crain, M.A. Eriksson, A. Kirakosian, J.L. Lin, C.T. Black, C.B. Murray, Appl. Phys. Lett. **83** (2003) 5053.
[259] K. Nakamoto, Infrared and Raman Spectra of Inorganic and Coordination Compounds, John Wiley & Son, New York,, 1997.
[260] T.V.V. Kumar, S. Prabhakar, G.B. Raju, J. Colloid Interface Sci. **247** (2002) 275.
[261] L. Zhang, R. He, H.C. Gu, Appl. Surface Sci. **253** (2006) 2611.
[262] R.D. Waldron, Phys. Rev **99** (1955) 1727.
[263] L.H. Dubois, B.R. Zegarski, R.G. Nuzzo, Langmuir **2** (1986) 412.
[264] Y.T. Tao, J. Am. Chem. Soc. **115** (1993) 4350.
[265] N. Wu, L. Fu, M. Su, M. Aslam, K.C. Wong, V.P. Dravid, Nano Lett. **4** (2004) 383.
[266] P. Guardia, B.B. Brugal, A.G. Roca, O. Iglesias, M.P. Morales, C.J. Serna, A. Labarta, X. Batlle, J. Magn. Magn. Mater. **316** (2007) e756.
[267] P. Berger, N.B. Adelman, K.J. Beckman, D.J. Campbell, A.B. Ellis, G.C. Lisensky, J. Chem. Ed **76** (1999) 943.
[268] M. Racuciu, D.E. Creanga, A. Airineil, V. Badescu, J. Optoel. Adv. Mater. **10** (2008) 635.
[269] A. Liebsch, Phys. Rev. B **48** (1993) 11317.
[270] T. Y.Olson, J.Z. Zhang, J. Mater. Sci. Technol. **24** (2008) 433.
[271] D. Wu, H. Zhu, L. Wang, L. Liu, Curr. Nanosci. **5** (2009) 103.
[272] P.C. Hiemenz, Principles of colloid and surface chemistry, M. Dekker, New York, 1986.
[273] Y. Hwang, J.K. Lee, J.K. Lee, Y.M. Jeong, S. Cheong, Y.C. Ahn, S.H. Kim, Powder Technol. **186** (2008) 145.
[274] S.J. Chung, J.P. Leonard, I. Nettleship, J.K. Lee, Y. Soong, D.V. Martello, M.K. Chyu, Powder Technol. **194** (2009) 75.
[275] C. Wu, T.J. Cho, J. Xu, D. Lee, B. Yang, M.R. Zachariah, Phys. Rev. E **81** (2010) 011406.
[276] J. Fan, L. Wang, J. Phys. D: Appl. Phys. **43** (2010) 165501.
[277] M.J. Assael, I.N. Metaxa, K. Kakosimos, D. Constantinou, Int. J. Thermophys. **27** (2006) 999.
[278] K. Kwak, C. Kim, Korea-Aust. Rheol. J. **17** (2005) 35.
[279] K.A. Kusters, S.E. Pratsinis, S.G. Thoma, D.M. Smith, Chem. Eng. Sci. **48** (1993) 4119.
[280] C. Lu, H. Mohwald, A. Fery, J. Phys. Chem. C **111** (2007) 10082.
[281] E. Brown, N.A. Forman, C.S. Orellana, H. Zhang, B.W. Maynor, D.E. Betts, J.M.D. Simone, H.M. Jaeger, Nature Mater. **9** (2011) 220.

[282] R.E. Rosensweig, Ferrohydrodynamics, 1 ed., Dover, New York, 1997.
[283] H.E. Horng, C.Y. Hong, S.Y. Yang, H.C. Yang, Appl. Phys. Lett. **82** (2003) 2434.
[284] S.Y. Yang, J.J. Chieh, H.E. Horng, C.Y. Hong, H.C. Yang, Appl. Phys. Lett. **84** (2004) 5204.
[285] A.F. Bakuzis, K.S. Neto, P.P. Gravina, L.C. Figueiredo, P.C. Morais, L.P. Silva, R.B. Azevedo, O. Silva, Appl. Phys. Lett. **84** (2004) 2355.
[286] J. Philip, T. Jaykumar, P. Kalyanasundaram, B. Raj, Meas. Sci. Technol. **14** (2003) 1289.
[287] T. Liu, X. Chen, Z. Di, J. Zhang, X. Li, J. Chen, Appl. Phys. Lett. **91** (2007) 121116.
[288] J.J. Chieh, S.Y. Yang, H.E. Horng, C.Y. Hong, H.C. Yang, Appl. Phys. Lett. **90** (2007) 133505.
[289] J.P. Huang, K.W. Yu, Appl. Phys. Lett. **86** (2005) 041905.
[290] W. Liao, X. Chen, Y. Chen, S. Pu, Y. Xia, Q. Li, Appl. Phys. Lett. **87** (2005) 151122.
[291] S. Pu, X. Chen, L. Chen, W. Liao, Y. Chen, Y. Xia, Appl. Phys. Lett. **87** (2005) 021901.
[292] H.E. Horng, C.S. Chen, K.L. Fang, S.Y. Yang, J.J. Chieh, C.Y. Hong, H.C. Yang, Appl. Phys. Lett. **85** (2004) 5592.
[293] J. Philip, G.G. Prakash, T. Jaykumar, P. Kalyanasundaram, B. Raj, Phys. Rev. Lett. **89** (2002) 268301.
[294] V.S. Mendelev, A.O. Ivanov, Phys. Rev. E **70** (2004) 051502.
[295] P. Bian, T.J.M. Carthy, Langmuir **26** (2010) 6145.
[296] T. Hao, R.E. Riman, J. Colloid Interface Sci. **297** (2006) 374.
[297] M. Klokkenburg, B.H. Erne, J.D. Meeldijk, A. Wiedenmann, A.V. Petukhov, R.P.A. Dullens, A.P. Philipse, Phys. Rev. Lett. **97** (2006) 185702
[298] J. Eapen, W.C. Williams, J. Buongiorno, L.W. Hu, S. Yip, R. Rusconi, R. Piazza, Phys. Rev. Lett. **99** (2007) 095901.
[299] Z. Hashin, S. Shtrikman, J. Appl. Phys **33** (1962) 3125.
[300] M. Klokkenburg, C. Vonk, E.M. Claesson, J.D. Meeldijk, B.H. Erne, A.P. Philipse, J. Am. Chem. Soc. **126** (2004) 16706.
[301] L.N. Donselaar, P.M. Frederik, P. Bomans, P.A. Buining, B.M. Humbel, A.P. Philipse, J. Magn. Magn. Mater. **201** (1999) 58.
[302] R. Haghgooie, P.S. Doyle, Phys. Rev. E **75** (2007) 061406.
[303] M. Gross, Phys. Rev. E **58** (1998) 6124.
[304] J.E. Martin, J. Odinek, T.C. Halsey, Phys. Rev. Lett. **69** (1992) 1524.
[305] A.Y. Zubarev, S. Odenbach, J. Fleischer, J. Magn. Magn. Mater. **252** (2002) 241.
[306] S. Odenbach, L.M. Pop, A.Y. Zubarev, GAMM Mitt. **30** (2007) 195.
[307] S. Odenbach, J. Phys.: Condens. Matter **15** (2003) S1497.
[308] P.D. Shima, J. Philip, B. Raj, Appl. Phys. Lett. **95** (2009) 133112.
[309] G. Cha, Y.S. Ju, L.A. Ahure, N.M. Wereley, J. Appl. Phys. **107** (2010) 09B505.
[310] S. Odenbach, J. Phys.: Condens. Matter **15** (2003) S1497.
[311] S.K. Das, N. Putra, P. Thiesen, W. Roetzel, ASME J. Heat Transfer **125** (2003) 567.
[312] D. Li, B. Hong, W. Fang, Y. Guo, R. Lin, Ind. Eng. Chem. Res. **49** (2010) 1697.
[313] M.P. Beck, T. Sun, A.S. Teja, Fluid Phase Equilibria **260** (2007) 275.
[314] B. Yang, Z.H. Han, Appl. Phys. Lett. **88** (2006) 261914.
[315] P.W. Bridgman, Proc. Natl. Acad. Sci. U. S. A **9** (1923) 341.
[316] R. Prasher, P. Bhattacharya, P.E. Phelan, Phys. Rev. Lett. **94** (2005) 025901.
[317] C.W. Nan, R. Birringer, D.R. Clarke, H. Gleiter, J. Appl. Phys. **81** (1997) 6692.
[318] M. Vladkov, J.L. Barrat, Nano Lett. **6** (2006) 1224.
[319] W. Evans, J. Fish, P. Keblinski, Appl. Phys. Lett. **88** (2006) 093116
[320] J.M. Laskar, J. Philip, B. Raj, Phys. Rev. E **78** (2008) 031404.
[321] A. Einstein, Investigation on the Theory of Brownian Movement, Dover, New York, 1956.
[322] G.K. Batchelor, J. Fluid Mech. **83** (1977) 97.

[323] I.M. Krieger, T.J. Dougherty, J. Rheol. **3** (1959) 137.
[324] R.G. Larson, The Structure and Rheology of Complex Fluids, Oxford University Press, New York, 1999.
[325] J.Y. Jung, C. Cho, W.H. Lee, Y.T. Kang, Int. J. Heat Mass Transfer **54** (2011) 1728.
[326] X.F. Zhou, L. Gao, J. Appl. Phys. **103** (2008) 083503
[327] C. Fang, C. Weng, S.P. Ju, Nanotechnology **17** (2006) 3909.
[328] H. Xie, J. Wang, T. Xi, Y. Liu, F. Ai, J. Mater. Sci. Lett. **21** (2002) 193.
[329] G. Chen, W. Yu, D. Singh, D. Cookson, J. Routbort, J. Nanopart. Res. **10** (2008) 1109.
[330] A.S. Cherkasova, J.W. Shan, ASME J. Heat Transfer **132** (2010) 082402.
[331] R.L. Hamilton, O.K. Crosser, Ind. Eng. Chem. Fundam. **1** (1962) 187.
[332] C.W. Nan, G. Liu, Y. Lin, M. Li, Appl. Phys. Lett. **85** (2004) 3549.
[333] W.A. Weil, W.C. Ormsby, Atomistic approach to the rheology of sand–water and clay–water mixtures Rheology:Theory and Applications, New York: Academic, 1960.
[334] B.E. Conway, D.A. Dobry, Viscosity of suspensions of electrically charged particles and solutions of polymeric electrolyte Rheology: Theory and Applications, New York: Academic, 1960.
[335] I.R. Rutgers, Rheol. Acta **2** (1962) 305.
[336] I.R. Rutgers, Rheol. Acta **2** (1962) 202.
[337] C.T. Nguyen, F. Desgranges, G. Roy, N. Galanis, T. MarE, S. Boucher, H.A. Mintsa, Int. J. Heat Fluid Flow **28** (2007) 1492.
[338] J.L. Barrat, F. Chiaruttini, Mol. Phys. **101** (2003) 1605.
[339] D.A. Weitz, J.S. Huang, M.Y. Lin, J. Sung, Phys. Rev. Lett. **53** (1984) 1657.
[340] M. Klokkenburg, B.H. Erne, V. Mendelev, A.O. Ivanov, J. Phys.: Condens. Matter **20** (2008) 204113
[341] K. Butter, P.H.H. Bomans, P.M. Frederik, G.J. Vroege, A.P. Philipse, Nature Mater. **2** (2003) 88.
[342] R.E. Rosensweig, Ferrohydrodynamics Cambridge Univ. Press, Cambridge, 1985.
[343] S. Odenbach, H. Stork, J. Magn. Magn. Mater. **183** (1998) 188.
[344] R.Y. Hong, J.H. Li, S.Z. Zhang, H. Zhong, Y. Zheng, J.M. Ding, D.G. Wei, Appl. Surface Sci. **255** (2009) 3485.
[345] A.Y. Zubarev, L.Y. Iskakova, Phys. Rev. E **61** (2000) 5415.
[346] S. Odenbach, H. Gilly, J. Magn. Magn. Mater. **152** (1996) 123.
[347] A.Y. Zubarev, J. Exp. Theor.Phs. **93** (2001) 80.
[348] M. Kroell, M. Pridoehl, G. Zimmermann, L. Pop, S. Odenbach, A. Hartwig, J. Magn. Magn. Mater. **289** (2005) 21.
[349] P.D. Shima, J. Philip, B. Raj, Appl. Phys. Lett. **97** (2010) 153113.
[350] B. Raj, P.D. Shima, J. Philip, NanoTrends **10** (2011) 14.
[351] P.D. Shima, J. Philip, B. Raj, J. Phys. Chem. C **114** (2010) 18825.
[352] J. Philip, P.D. Shima, B. Raj, Appl. Phys. Lett. **91** (2007) 203108.
[353] J. Philip, P.D. Shima, B. Raj, Nanotechnology **19** (2008) 305706.
[354] P.D. Shima, J. Philip, J. Phys. Chem. C (2011) (Communicated).
[355] J. Philip, P.D. Shima, B. Raj, Appl. Phys. Lett. **92** (2008) 043108.

****